

Harnessing Reconfigurable Intelligent Surfaces For Next-Gen Wireless Networks: Enhancing Efficiency, Reliability, and Security

Youssef Maghrebi

**A Thesis
in
The Department
of
Electrical and Computer Engineering**

**Presented in Partial Fulfillment of the Requirements
for the Degree of
Master of Applied Science (Electrical and Computer Engineering) at
Concordia University
Montréal, Québec, Canada**

February 2025

© Youssef Maghrebi, 2025

CONCORDIA UNIVERSITY

School of Graduate Studies

This is to certify that the thesis prepared

By: **Youssef Maghrebi**

Entitled: **Harnessing Reconfigurable Intelligent Surfaces For Next-Gen Wireless
Networks: Enhancing Efficiency, Reliability, and Security**

and submitted in partial fulfillment of the requirements for the degree of

Master of Applied Science (Electrical and Computer Engineering)

complies with the regulations of this University and meets the accepted standards with respect to originality and quality.

Signed by the Final Examining Committee:

Dr. Jun Cai Chair

Dr. Jun Cai Examiner

Dr. Wei-Ping Zhu Examiner

Dr. Chadi Assi Supervisor

Dr. Ali Ghrayeb Co-supervisor

Approved by _____
Abdelwahab Hamou-Lhadj, Chair
Department of Electrical and Computer Engineering

_____ 2025

Mourad Debbabi, Dean
Faculty of Engineering and Computer Science

Abstract

Harnessing Reconfigurable Intelligent Surfaces For Next-Gen Wireless Networks: Enhancing Efficiency, Reliability, and Security

Youssef Maghrebi

As wireless networks evolve to meet the demands for high-speed, reliable, and secure communications, emerging technologies like Reconfigurable Intelligent Surface (RIS) are set to reshape wireless environments. This thesis investigates the transformative role of RIS in next-generation networks, focusing on performance enhancement and security. The research is divided into two major contributions.

The first part examines the integration of an active STAR-RIS with a full-duplex Cooperative Rate Splitting Multiple Access (FD C-RSMA) system in a downlink Multiple Input Multiple Output (MISO) configuration. To tackle the non-convex optimization problem, an alternating optimization framework based on successive convex approximation (SCA) is developed, achieving up to a 20.3% improvement in network sum rate. Additionally, to simplify real-time decision-making, a deep reinforcement learning model using an actor-critic architecture is proposed, reducing computational time by 98% compared to the SCA method.

The second part explores the effects of a movable antenna (MA)-assisted jammer in a downlink MISO system. The analysis shows that MA-based jamming causes a 30% reduction in sum rate and a 25% increase in outage probability compared to fixed antenna setups. Furthermore, the study evaluates the effectiveness of RIS as a countermeasure against such adversarial attacks under different levels of jammer knowledge. Safeguarding RIS channel state information is found to be critical, as its compromise renders the system ineffective.

Overall, this research provides a comprehensive framework for utilizing RIS to enhance communication performance and strengthen security in wireless environments, laying the foundation for robust next-generation networks.

Acknowledgments

I would like to express my deepest gratitude to my advisors, Professor Chadi Assi and Professor Ali Ghrayeb, whose guidance, support, and insightful feedback have been instrumental throughout my research journey. Their expertise have not only shaped this work but have also greatly enriched my academic experience.

Additionally, I wish to express my sincere gratitude to my dear friend, Dr. Mohamed Elhatab, whose timely support and unwavering assistance proved indispensable during challenging moments.

I would like also to thank the committee members for their effort and time in reading my thesis and providing me with valuable comments and suggestions.

I extend my heartfelt appreciation to my colleagues and friends for the stimulating discussions and collaborative spirit that helped me overcome challenges along the way. Finally, I am profoundly grateful to my family for their endless love, patience, encouragement, and moral support without which this accomplishment would not have been possible.

Thank you all for being an indispensable part of this journey and for every contribution, no matter how small, that has made this achievement possible.

Contents

List of Figures	viii
List of Tables	x
List of Algorithms	xi
List of Acronyms	xii
List of Symbols	xiv
1 Introduction	1
1.1 Motivation	1
1.2 Objectives and Scope	2
1.3 Thesis Contributions	3
1.4 Research Outcomes	5
1.5 Thesis Organization	6
2 Background	7
2.1 The Evolution of Multiple Access and the Emergence of Rate-Splitting	7
2.2 Cooperative Rate-Splitting Multiple Access (C-RSMA): Integrating Cooperation for Enhanced Wireless Communication	11
2.3 Reconfigurable Intelligent Surfaces (RIS): A Paradigm Shift in Wireless Communi- cations	12
2.3.1 Passive RIS vs. Active RIS	14

2.3.2	Reflective RIS vs. Simultaneously Reflective and Transmissive (STAR-RIS)	15
2.4	Movable Antennas: A Key Enabler for Dynamic and Adaptive Wireless Systems	16
2.5	Deep Learning in Modern Wireless Communication Systems	17
3	RIS for Enhancing Sum Rate Performance in C-RSMA-Enabled Downlink Wireless Networks	20
3.1	Introduction	20
3.2	State of The Art	21
3.3	Contributions	23
3.4	Performance Analysis of RIS in C-RSMA-Enabled Downlink Wireless Networks	24
3.4.1	System Model	24
3.4.2	Problem Formulation	28
3.4.3	Solution Approach	29
3.4.4	Complexity and Convergence	33
3.4.5	Simulation Results and Discussion	34
3.5	A Deep Reinforcement Learning-Driven Optimization for Active STAR-RIS empowered C-RSMA	38
3.5.1	Problem Formulation	38
3.5.2	MDP Description	40
3.5.3	Reward Design	41
3.5.4	Model Architecture	42
3.5.5	Prioritized Experience Replay	45
3.5.6	Simulation Results and Discussion	45
3.6	Summary and Conclusions	48
4	RIS for Enhancing Resilience Against MA-Enabled Jamming in Downlink Wireless Networks	50
4.1	Introduction	50
4.2	State of The Art	51
4.3	Contributions	53

4.4	Analyzing MA-Enabled Jamming in Downlink Wireless Networks	54
4.4.1	System Model	54
4.4.2	Problem Formulation	58
4.4.3	Solution Approach	59
4.4.4	Simulation Results and Discussion	61
4.5	Performance Analysis of RIS in mitigating MA-enabled Jamming in Downlink Wireless Networks	66
4.5.1	System Model	66
4.5.2	Problem Formulation	67
4.5.3	Simulation Results and Discussion	69
4.6	Summary and Conclusions	78
5	Conclusion and Future Directions	80
5.1	Conclusion	80
5.2	Future Directions	81
	Bibliography	83

List of Figures

Figure 2.1	Comparison between NOMA and other multiple access techniques: a) TDMA; b) FDMA; c) OFDMA; d) CDMA/SDMA; e) possible NOMA solution [6]	9
Figure 2.2	Diagram of a Rate-Splitting Multiple Access (RSMA) System in a MIMO Downlink Network [9]	10
Figure 2.3	An illustration of CRSMA, where users 1 and 2 relay the common stream s_c to user 3	12
Figure 2.4	An illustration of an RIS-assisted wireless communication [16]	13
Figure 2.5	Comparison between STAR-RIS and conventional RIS.	15
Figure 2.6	Movement mechanisms for Movable Antennas [23]	16
Figure 3.1	System model	25
Figure 3.2	Simulation setup	35
Figure 3.3	Convergence of Algorithm 1	36
Figure 3.4	Active STAR RIS-assisted FD C-RSMA performance against baselines	37
Figure 3.5	MDP illustration	40
Figure 3.6	Actor loss for Actor-Critic-1	46
Figure 3.7	Critic loss for Actor-Critic-1	46
Figure 3.8	Critic loss for Actor-Critic-2	47
Figure 3.9	Actor loss for Actor-Critic-2	47
Figure 3.10	DRL model performance against SCA baseline method	47
Figure 3.11	Comparison of prediction time of the DRL model against the SCA baseline	47
Figure 4.1	Jamming system model	54

Figure 4.2	Movable antenna array	55
Figure 4.3	Comparison of sum rate variation with respect to jammer power and location	62
Figure 4.4	Analysis of system outage probability with respect to jamming power	63
Figure 4.5	System model	66
Figure 4.6	Sum rate variation according to the available power at the jammer for all configurations	74
Figure 4.7	Comparison of sum rate variation between MA and FPA based jamming as a function of jammer power	74
Figure 4.8	Variation in the percentage of users in outage according to the available power at the jammer for all configurations, $R_{th} = 1.5(bps/Hz)$	75
Figure 4.9	Comparison of variation in the percentage of users in outage between MA and FPA based jamming as a function of jammer power, $R_{th} = 1.5(bps/Hz)$	75
Figure 4.10	Variation in the percentage of users in outage according to the available power at the jammer for all configurations, $R_{th} = 1(bps/Hz)$	76
Figure 4.11	Comparison of variation in the percentage of users in outage between MA and FPA based jamming as a function of jammer power, $R_{th} = 1(bps/Hz)$	76
Figure 4.12	System outage probability variation according to the available power at the jammer for all configurations, $R_{th} = 1.5(bps/Hz)$	77
Figure 4.13	Comparison of system outage probability variation between MA and FPA based jamming as a function of jammer power, $R_{th} = 1.5(bps/Hz)$	77

List of Tables

Table 3.1 Simulation Parameters 36

Table 3.2 Training Hyperparameters 46

Table 4.1 Simulation Parameters 62

List of Algorithms

1	Joint Beamforming Optimization	33
2	Joint Optimization of \mathbf{V} and \mathbf{P}	59

List of Acronyms

AO	Alternating Optimization
AS	Antenna Selection
AWGN	Additive White Gaussian Noise
BCD	Block Coordinate Descent
BN	Batch Normalization
BS	Base Station
CDMA	Code Division Multiple Access
C-RSMA	Cooperative Rate Splitting Multiple Access
CSI	Channel State Information
DoF	Degree of Freedom
DRL	Deep Reinforcement Learning
EM	Electromagnetic
eMBB	Enhanced Mobile Broadband FAS Fluid Antenna Systems
FD	Full Duplex
FDMA	Frequency Division Multiple Access
FPA	Fixed Position Antenna
FRI	Field Response Information
FRM	Field Response Matrix
FRV	Field Response Vector
HD	Half Duplex
IoT	Internet of Things
LoS	Line of Sight
MA	Movable Antenna
mMTC	Massive Machine-Type Communication
MDP	Markov Decision Process
MISO	Multiple Input Single Output

MRC	Maximal Ratio Combining
MUSA	Multi User Shared Access
NLoS	Non Line of Sight
NOMA	Non Orthogonal Multiple Access
OFDMA	Orthogonal Frequency Division Multiple Access
PDMA	Pattern Division Multiple Access
PER	Prioritized Experience Replay
PLS	Physical Layer Security
PRM	Path Response Matrix
RAN	Radio Access Network
ReLU	Rectified Linear Unit
RF	Radio Frequency
RIS	Reconfigurable Intelligent Surface
RL	Reinforcement Learning
RSMA	Rate Splitting Multiple Access
SCA	Successive Convex Approximation
SCMA	Sparse Code Multiple access
SDMA	Spatial Division Multiple Access
SI	Self Interference
SIC	Successive Interference Cancellation
STAR-RIS	Simultaneously Transmitting and Reflecting Reconfigurable Intelligent Surface
TD	Temporal Difference
TDMA	Time Division Multiple Access
ULA	Uniform Linear Array
URLLC	Ultra-Reliable Low-Latency Communication

List of Symbols

\mathbb{C}	Set of complex numbers
\mathbb{R}	Set of real numbers
j	Imaginary unit ($j^2 = -1$)
σ^2	Noise variance
∇	Gradient operator
\sum	Summation operator
\prod	Product operator
$\mathbb{E}\{x\}, \mathbb{E}[x]$	Expectation of random variable x
$\text{diag}(\mathbf{x})$	Diagonal matrix with vector \mathbf{x} as diagonal
$e^{(\cdot)}, \exp(\cdot)$	Exponential function
$ x $	Absolute value or magnitude of x
$\ \mathbf{x}\ $	Euclidean norm of vector \mathbf{x}
$\ \mathbf{M}\ _F$	Frobenius norm of matrix \mathbf{M}
$\mathbf{x}^H, \mathbf{M}^H$	Hermitian of vector \mathbf{x} and matrix \mathbf{M} , respectively
$\mathbf{x}^T, \mathbf{M}^T$	Transpose of vector \mathbf{x} and matrix \mathbf{M} , respectively
$\Re(x)$	Real part of x
$[\mathbf{x}]_n$	n^{th} coefficient of vector \mathbf{x}
h^*	Conjugate of complex variable h
$\max(v_1, v_2)$	Maximum value between two values v_1 and v_2
λ	Wavelength of a transmitted signal
$P(\cdot)$	Probability operator

Chapter 1

Introduction

1.1 Motivation

The increasing demand for high-speed, reliable, and secure wireless communication has become a driving force behind the evolution of next-generation networks. Emerging applications such as ultra-high-definition streaming, autonomous vehicles, industrial automation, and immersive extended reality experiences are pushing current infrastructures to their limits, prompting researchers to explore innovative technologies that enhance network performance.

Among these, Reconfigurable Intelligent Surfaces (RIS) have emerged as a key enabler for future wireless networks by offering the ability to dynamically control the propagation environment. By intelligently reflecting and steering signals, RIS can boost efficiency, improve coverage, and mitigate interference, making them a promising solution for advanced communication systems.

Simultaneously, Cooperative Rate Splitting Multiple Access (C-RSMA) has gained traction as an effective method for managing interference and optimizing resource allocation in downlink networks. By dividing messages into common and private parts and leveraging user cooperation, C-RSMA enhances spectral efficiency and overall throughput. Integrating RIS—especially advanced configurations like active STAR-RIS—with C-RSMA can further amplify these benefits, creating a synergy that significantly improves system performance in dynamic wireless environments.

While RIS and C-RSMA offer substantial advantages, their integration also introduces new

challenges. Traditional optimization techniques often struggle with the dynamic and complex nature of modern wireless systems, hindering real-time decision-making. Deep Reinforcement Learning (DRL) has emerged as a powerful tool to overcome these limitations, enabling adaptive and intelligent control of network resources in RIS-assisted configurations.

Moreover, movable antennas (MAs) introduce additional degrees of freedom for optimizing signal reception and adapting to changing network conditions. However, the potential misuse of MAs—particularly in adversarial scenarios like adaptive jamming—highlights the need for robust security measures. In this context, RIS not only enhances communication performance but also offers avenues for developing strategies to counteract emerging security threats.

This thesis investigates the role of RIS in enhancing the efficiency, reliability, and security of next-generation wireless networks. By leveraging advanced optimization techniques and DRL-based approaches, the research explores how RIS can maximize spectral efficiency, improve network resilience, and mitigate security vulnerabilities—with a particular focus on its integration with C-RSMA systems. Through this comprehensive study, the thesis aims to address key challenges associated with RIS deployment and propose innovative solutions to enhance the effectiveness of future wireless networks.

1.2 Objectives and Scope

The primary objective of this thesis is to investigate the role of RIS in enhancing the efficiency, reliability, and security of downlink wireless networks. Specifically, this research explores two key aspects: first, how RIS can improve the performance of a cooperative rate-splitting multiple access (C-RSMA) based downlink system by optimizing interference management and spectral efficiency; and second, how RIS can be leveraged to mitigate the impact of MA-based jamming, enhancing network resilience against adversarial interference. To achieve these objectives, the following specific goals are pursued:

- Conduct a comprehensive review of the literature on RSMA, RIS, and MAs, with a focus on their applications in wireless communication systems.
- Investigate the combined benefits of rate splitting and active Simultaneously Transmitting and

Reflecting RIS (STAR-RIS) in enhancing the performance of downlink wireless networks, with a particular focus on system sum rate. This includes assessing the capabilities of active and passive RIS configurations under various network scenarios.

- Develop and evaluate a DRL-based framework to optimize the deployment and operation of active STAR-RIS in C-RSMA systems, achieving near real-time computation with reduced complexity.
- Analyze the potential threats posed by malicious use of MAs by jammers in downlink wireless systems, including their impact on network reliability and performance.
- Investigate the impact of RIS in mitigating jamming attacks, focusing on lowering outage probability and minimizing the number of users affected by outages.
- Validate all proposed solutions through simulations, comparing their performance with existing baselines to demonstrate their effectiveness across various practical wireless network scenarios.

The scope of this thesis is limited to downlink scenarios and does not address the use of active STAR-RIS in uplink wireless networks. Additionally, it does not cover other security challenges related to MA such as eavesdropping, or the real-world implementation of the proposed techniques. However, the effectiveness and performance of the proposed techniques will be evaluated through simulations and experiments. This thesis aims to contribute to the development of novel RIS-based strategies that can enhance both the performance and security of downlink wireless networks, laying the groundwork for future research in this field.

1.3 Thesis Contributions

The main contributions of this thesis can be detailed as:

- We analyze the performance of an active STAR-RIS in assisting FD C-RSMA in a downlink multiple-input single-output (MISO) system, where a BS serves K users, with S users assisting in the transmission for the remaining users.

- We investigate the joint optimization of the BS precoding vectors, active STAR-RIS reflection and transmission matrices, common stream split, and the transmit powers of strong users to maximize the network sum rate while meeting minimum rate constraints, adhering to active STAR-RIS hardware constraints, and ensuring the power budget at the BS, the active STAR-RIS, and each strong user. We address this non-convex optimization problem is solved using an SCA-based alternating optimization (AO) algorithm.
- We conduct rigorous simulations to demonstrate significant performance gains from the cooperation between users and the inclusion of active STAR-RIS. Our results show maximum sum rates with minimal BS power, achieving a remarkable 20.3% improvement at 32 dBm compared to the second-ranked baseline. Additionally, a modest active STAR-RIS power of 24 dBm yields an approximately 6% gain over the same baseline.
- We develop a DRL model to optimize the computational time of the proposed STAR-RIS-assisted FD C-RSMA system. The trained model jointly optimizes the BS precoding vectors, active STAR-RIS reflection and transmission matrices, common stream split, and the transmit powers of strong users.
- We propose a novel training framework based on the actor-critic architecture to handle the continuous state and action spaces of the optimization variables. Our approach utilizes two actor-critic models, each focusing on a subset of variables, to improve scalability by reducing the state space dimension. Simulations are conducted under various conditions, comparing the proposed model with an SCA-based convex optimization baseline to evaluate its strengths and weaknesses.
- We analyze the impact of an MA-assisted jammer in a downlink MISO system, where a BS serves K users through SDMA. We formulate an optimization problem in which the jammer decides both the antenna locations and beamforming vectors to minimize the overall system sum rate. Due to its non-convexity, the problem is divided into two sub-problems, which are alternately solved until convergence.
- We perform numerical examples under different scenarios, comparing the system sum rate

and outage probability achieved with MAs versus FPAs. Results indicate that MAs reduce the system sum rate 30% more than FPAs. Moreover, MAs raise the outage probability by 25% compared to FPAs, resulting in a 20% increase in the number of users affected by outages.

- We rigorously evaluate the performance of RIS as a potential countermeasure against MA-based jamming attacks. Our investigation encompasses extensive simulation studies that assess key performance metrics—including system sum rate and outage probability—under diverse adversarial conditions. We examine two key scenarios: one where the jammer has full access to the RIS configuration and another where it does not, thereby establishing the upper and lower bounds of its impact. Our findings highlight that protecting the RIS channel state information is essential, as its compromise not only negates the benefits of RIS but can also turn it into a liability for the system.

1.4 Research Outcomes

The work accomplished in this thesis has led to the following publications:

- [1] Maghrebi, Y., Elhattab, M., Assi, C., Ghrayeb, A., & Kaddoum, G. "Cooperative rate splitting multiple access for active star-ris assisted downlink communications". In: *IEEE Wireless Communications Letters* 13(10), pp. 2827-2831. DOI: 10.1109/LWC.2024.3448409
- [2] Maghrebi, Y., Elhattab, M., Assi, C., & Ghrayeb, A. "A Deep Reinforcement Learning-Driven Optimization for STAR-RIS-empowered Cooperative RSMA". In: *IEEE Middle East Conference on Communications and Networking 2024*.
- [3] Maghrebi, Y., Elhattab, M., Assi, C., Ghrayeb, A., & Kaddoum, G. "Movable antennas in wireless systems: A tool for connectivity or a new security threat?" Available on Arxiv: <https://arxiv.org/abs/2411.06028> - Accepted to be published in: *IEEE International Conference on Communications 2025*.

1.5 Thesis Organization

The thesis is organized into five main chapters. Chapter 1 introduces the motivation, objectives, and scope of the research. Chapter 2 provides background on key technologies essential for understanding the work. Chapter 3 explores the role of RIS in enhancing C-RSMA within a downlink wireless network, with a focus on the potential of active Simultaneously Transmitting and Reflecting RIS (STAR-RIS) and a comparative analysis with other RIS configurations. Additionally, it presents a DRL solution for solving the optimization problem, aiming to improve time efficiency and achieve near real-time performance. Chapter 4 examines the impact of MAs on jamming in wireless networks, comparing their effectiveness against fixed-position antenna arrays. Furthermore, it investigates the use of RIS to counteract jamming enhanced by MAs, evaluating its effectiveness in mitigating such attacks. Finally, chapter 5 summarizes the key findings and outlines directions for future research.

Chapter 2

Background

In this chapter, we introduce the key technologies that form the foundation of this thesis. We begin by discussing the rate splitting multiple access technique and its cooperative variant (C-RSMA), highlighting their advantages in managing interference and improving spectral efficiency. Next, we explore reconfigurable intelligent surfaces, detailing their different configurations and their potential to enhance wireless communication by intelligently manipulating electromagnetic (EM) waves. We then examine the concept of movable antennas, emphasizing their role in dynamic beamforming and adaptability in wireless networks. Finally, we discuss the role of machine learning in modern wireless communications, focusing on its applications in resource allocation, network optimization, and intelligent decision-making to enhance system performance and security.

2.1 The Evolution of Multiple Access and the Emergence of Rate-Splitting

Wireless communication has undergone continuous evolution to meet the ever-growing demands for higher data rates, increased spectral efficiency, and enhanced user connectivity. At the heart of this evolution lies multiple access techniques, which govern how multiple users share limited wireless resources effectively. In the early generations of mobile networks (1G, 2G, and 3G), classical orthogonal multiple access (OMA) techniques, such as Time Division Multiple Access (TDMA), Frequency Division Multiple Access (FDMA), Code Division Multiple Access (CDMA), and later

Orthogonal Frequency Division Multiple Access (OFDMA) in 4G, were the dominant methods used for resource allocation [4]. These techniques work by assigning distinct time slots, frequency bands, codes or subcarriers to different users, ensuring that transmissions remain orthogonal and interference-free. This inherent orthogonality made system design straightforward and enabled efficient resource allocation while simplifying interference management at the receiver. Given the hardware constraints and computational limitations of early mobile devices, these techniques were well-suited for their respective generations.

However, as wireless networks evolved, the limitations of purely orthogonal access schemes became apparent. The transition to 4G LTE and, more recently, 5G introduced stringent requirements that OMA struggled to satisfy. The explosive growth in mobile data traffic, fueled by high-definition video streaming, cloud computing, and the Internet of Things (IoT), necessitated a paradigm shift in resource allocation strategies [5]. Furthermore, emerging 5G applications such as ultra-reliable low-latency communication (URLLC), enhanced mobile broadband (eMBB), and massive machine-type communication (mMTC) demanded higher spectral efficiency, lower latency, and more flexible resource management [5]. In densely populated networks, OMA's approach of allocating dedicated resources to each user became inefficient, as spectrum resources were often underutilized, particularly in scenarios with fluctuating traffic loads. Moreover, as the number of users per cell increased, the spectral efficiency (SE) of OMA plateaued due to the limited number of orthogonal resource blocks available [4]. These challenges prompted researchers to explore alternative multiple access strategies capable of serving more users within the same spectral resources.

A major breakthrough came with the development of non-orthogonal multiple access (NOMA), which departed from the traditional orthogonality constraint. Unlike OMA, which assigns separate resources to each user, NOMA enables multiple users to share the same time and frequency resources by leveraging differences in their channel conditions. This is achieved using power-domain multiplexing, where signals for different users are superimposed at different power levels, and successive interference cancellation (SIC) is employed at the receiver to decode the signals. A comparison between NOMA and other multiple access techniques is depicted in Fig. 2.1. Other approaches such as sparse code multiple access (SCMA), pattern division multiple access (PDMA), and multi-user shared access (MUSA) exploit different domains—such as code, pattern, or sequence—to

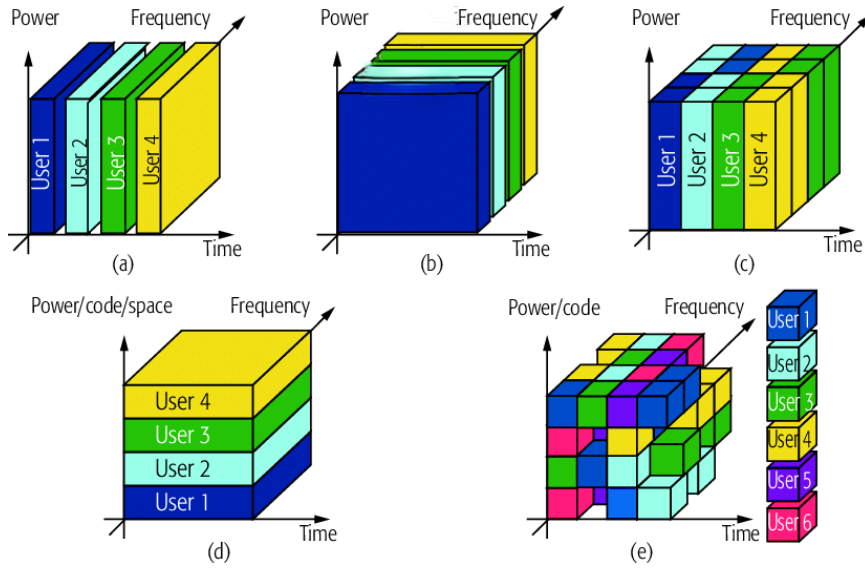


Figure 2.1: Comparison between NOMA and other multiple access techniques: a) TDMA; b) FDMA; c) OFDMA; d) CDMA/SDMA; e) possible NOMA solution [6]

enhance spectral efficiency and connectivity [7]. NOMA improves spectral efficiency by allowing more users to be accommodated within the same bandwidth, making it particularly suitable for massive connectivity scenarios in 5G and beyond. However, despite its advantages, NOMA presents several challenges. The SIC process, which is crucial for separating user signals, increases receiver complexity and may not always be reliable, especially when channel conditions fluctuate or when users have similar power levels [8]. Additionally, fairness issues arise as weaker users often experience higher residual interference, leading to performance degradation. These drawbacks highlighted the need for a more flexible and robust approach to multiple access.

To address these challenges, rate-splitting multiple access (RSMA) emerged as a promising alternative that generalizes both OMA and NOMA while striking a more balanced trade-off between spectral efficiency, interference management, and receiver complexity. The key idea behind RSMA is to split each user's message W_k into a common part $W_{c,k}$ and a private part $W_{p,k}$. The common parts of all users are combined into a single common message W_c , which is then encoded and transmitted along with the private messages. At the receiver side, each user first decodes the common message W_c using a Successive Interference Cancellation (SIC) process and extracts its intended part $\hat{W}_{c,k}$. After removing the common message's contribution, the user then decodes its private message $W_{p,k}$ independently.

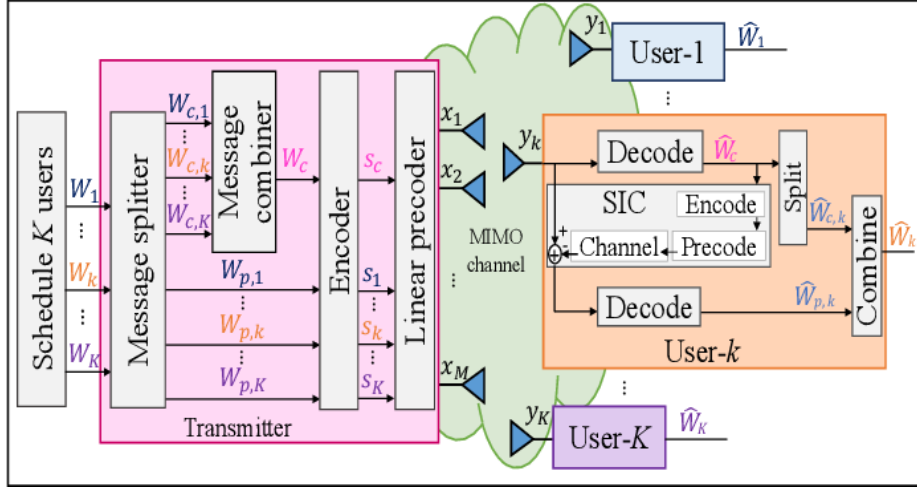


Figure 2.2: Diagram of a Rate-Splitting Multiple Access (RSMA) System in a MIMO Downlink Network [9]

This process is illustrated in Fig. 2.2, where the transmitter consists of a message splitter, a message combiner, an encoder, and a linear precoder. The transmitted signal vector $\mathbf{s} = [s_1, \dots, s_K]^T$ passes through a MIMO channel, producing received signals $\mathbf{y} = [y_1, \dots, y_K]^T$ at the users. Each user performs SIC, splits the received signal into its common and private components, and reconstructs its intended message \hat{W}_k . This enables a more dynamic interference management strategy that allows the system to adjust the level of signal superposition and decoding complexity based on network conditions [10]. Unlike NOMA, which relies on multiplexing in a sole domain, RSMA provides a more flexible framework that encompasses both power-domain and code-domain multiplexing, making it adaptable to different interference scenarios.

One of the key advantages of RSMA is its ability to handle interference in a more structured manner. By leveraging rate splitting, the system can control how much interference is treated as noise versus how much is decoded and removed [10]. This is particularly beneficial in scenarios with moderate to high interference, where treating all interference as noise (as in OMA) or decoding all interference (as in NOMA) is suboptimal. RSMA can dynamically adjust its strategy based on the interference level, optimizing spectral efficiency while ensuring fair resource allocation. Moreover, RSMA exhibits superior robustness in practical deployments, as it does not rely on strict power disparities among users like NOMA does. This makes RSMA more adaptable to a wider range of network conditions, including multi-antenna systems and multi-cell environments [8].

Given these advantages, RSMA is increasingly being recognized as a key enabler for future wireless networks, including 6G [8]. Its ability to provide a unified multiple access framework that seamlessly integrates OMA and NOMA principles makes it highly scalable and efficient. Furthermore, RSMA is well-suited for emerging technologies such as RIS, where intelligent reflection and beamforming can further enhance its performance. As wireless networks continue to evolve, RSMA is expected to play a pivotal role in optimizing spectral efficiency, improving user fairness, and enabling more resilient and adaptive communication systems.

2.2 Cooperative Rate-Splitting Multiple Access (C-RSMA): Integrating Cooperation for Enhanced Wireless Communication

As wireless networks continue to evolve, ensuring fairness and maintaining quality of service (QoS) for all users remains a key challenge, especially in heterogeneous network environments where channel conditions vary significantly. While RSMA, as discussed in the previous section, effectively enhances spectral efficiency and manages interference, its performance can degrade in scenarios with highly disparate channel conditions. In particular, weaker users—such as those at the cell edge or experiencing deep fading—may struggle to decode the common message, limiting their achievable data rates and reducing overall network fairness [11]. To overcome this limitation, C-RSMA builds upon RSMA by introducing user cooperation. In this approach, stronger users assist weaker users in decoding the common stream, improving transmission reliability and enhancing spectral efficiency across the network [11].

The idea of user cooperation in multiple access techniques is not new. In NOMA for instance, Cooperative NOMA (C-NOMA) was developed to improve the performance of weaker users by leveraging stronger users as relays [12]. In C-NOMA, users with better channel conditions perform SIC to decode signals intended for weaker users and then forward these signals, ensuring more reliable transmission. This approach has been shown to improve spectral efficiency and fairness, particularly in heterogeneous networks with a mix of strong and weak users.

Inspired by the benefits of cooperation in NOMA, researchers extended this concept to RSMA, giving rise to C-RSMA. In C-RSMA, users with stronger channel conditions, typically those closer

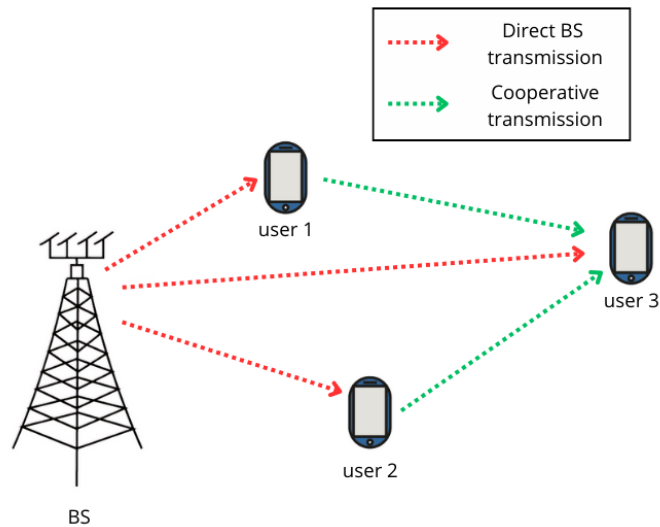


Figure 2.3: An illustration of CRSMA, where users 1 and 2 relay the common stream s_c to user 3

to the BS, can successfully decode the common stream with high reliability. These strong users then act as relays, forwarding the common message to weaker users via direct transmission or cooperative beamforming to assist others who face difficulty due to poor channel conditions as illustrated in Fig. 2.3. As a result, weaker users, who might otherwise experience decoding failures due to deep fading or severe path loss, benefit from improved transmission reliability. The cooperative mechanism in C-RSMA not only enhances spectral efficiency by reducing redundant retransmissions from the BS but also significantly reduces outage probability and improves overall fairness in user performance.

2.3 Reconfigurable Intelligent Surfaces (RIS): A Paradigm Shift in Wireless Communications

With the increasing demand for high-capacity, energy-efficient, and ultra-reliable wireless communication systems, conventional network architectures face significant challenges in meeting the stringent requirements of next-generation networks, such as 6G. Traditionally, improvements in wireless communication have relied on optimizing active components, including base stations, relays, and user equipment, to enhance signal transmission and reception. However, these approaches

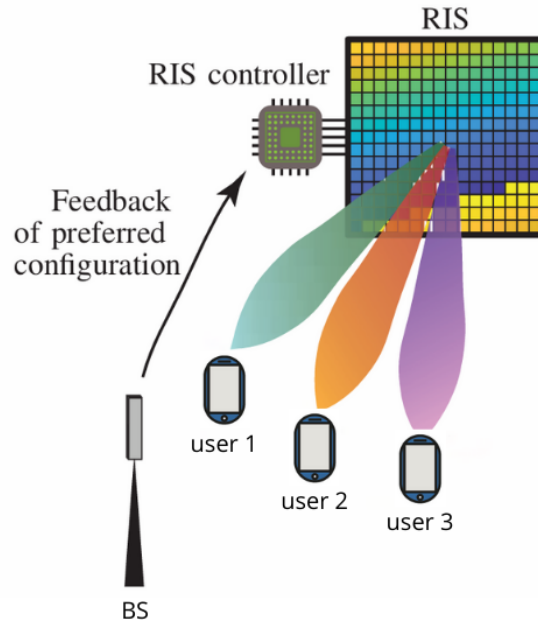


Figure 2.4: An illustration of an RIS-assisted wireless communication [16]

often lead to increased power consumption, hardware complexity, and deployment costs. For instance, the study done by Intel [13] highlights that even with the evolution of technologies such as 5G, the Radio Access Network (RAN)—which predominantly comprises active components like BSs—accounts for over 50% of total network power consumption. This clearly indicates that enhancing performance by adding more sophisticated active components can significantly raise energy demands and associated costs. Similarly, the research presented in [14] demonstrates that wireless transceivers exhibit considerable variability in power consumption due to differences in hardware design and complexity. This variability underlines the fact that optimizing user equipment to improve signal quality inherently leads to higher power usage and more intricate hardware implementations. Additionally, [15] further supports this perspective by showing how even at the device level, processes like signal sampling and analog-to-digital conversion add substantial overhead in terms of power consumption and design complexity. Collectively, these studies corroborate the notion that while active component optimization has historically improved communication performance, it also incurs significant trade-offs in terms of increased energy consumption, hardware complexity, and deployment expenses. A novel technology that has recently gained attention as a promising solution to these challenges is RIS.

RIS consists of a planar metasurface made up of numerous sub-wavelength unit cells, also called meta-atoms, whose EM properties can be dynamically controlled via external tuning mechanisms [17] such as shown in Fig. 2.4. By appropriately adjusting the phase shifts and amplitudes of incident signals, RIS can intelligently manipulate the wireless propagation environment, improving signal strength, mitigating interference, and enhancing coverage without requiring additional power-hungry active components [18], [19]. RIS can be classified based on its power supply mechanism, operational mode, and deployment strategy. The key configurations include:

2.3.1 Passive RIS vs. Active RIS

Passive RIS:

The majority of existing RIS designs operate in a passive manner, meaning they do not actively amplify or generate signals. Instead, they rely solely on the incoming EM waves, adjusting their phase shifts to steer the reflected signals toward desired directions [20]. Passive RIS is energy-efficient since it eliminates the need for power-consuming radio-frequency (RF) chains and amplifiers. However, it suffers from double path loss—the signal first attenuates when traveling from the transmitter to the RIS and again when it reflects toward the receiver, which limits its performance in long-distance communication [20].

Active RIS:

To address the double-fading effect inherent in passive RIS, researchers have explored active RIS, where each meta-element is equipped with amplifiers to compensate for signal attenuation. Unlike passive RIS, active RIS can boost the reflected signals, thereby improving coverage and reliability. However, this comes at the cost of increased power consumption and additional hardware complexity [20]. Active RIS is particularly useful in scenarios where the received signal strength at the RIS is weak, requiring amplification before redirection.

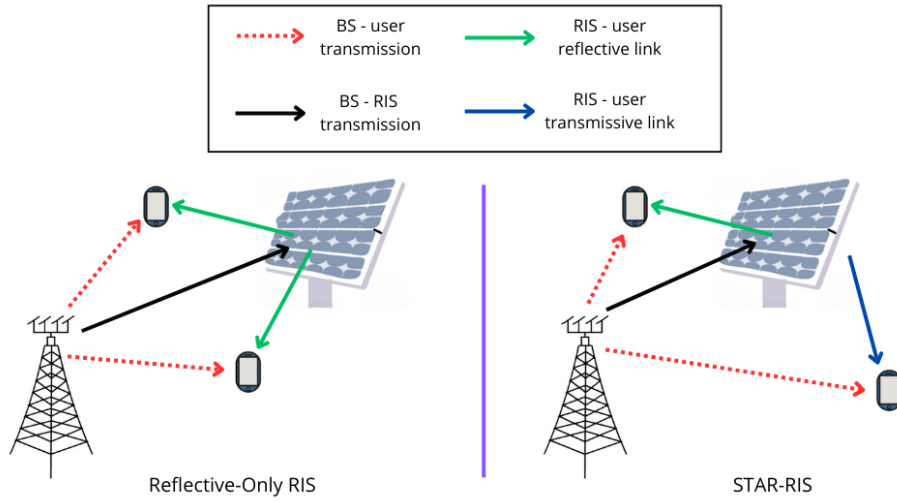


Figure 2.5: Comparison between STAR-RIS and conventional RIS.

2.3.2 Reflective RIS vs. Simultaneously Reflective and Transmissive (STAR-RIS)

Reflective-Only RIS:

In traditional RIS designs, the surface is deployed to reflect incident signals toward a specific direction. These systems are typically mounted on walls, building facades, or other structures to optimize the propagation of downlink and uplink signals. Reflective-only RIS is effective in scenarios where the transmitter and receiver are located on the same side of the RIS, ensuring proper signal redirection. However, this limits its applicability in certain environments, such as indoor-outdoor transitions, where signals need to be redirected in multiple directions.

Simultaneously Transmitting and Reflecting RIS (STAR-RIS):

Unlike conventional reflective-only RIS, STAR-RIS is capable of simultaneously reflecting and transmitting signals in different directions. This feature makes it particularly advantageous in full-space coverage scenarios, where users are distributed on both sides of the RIS [21]. Figure 2.5 demonstrates the comparison between STAR-RIS and conventional RIS. STAR-RIS can dynamically adjust the power ratio allocated between reflection and transmission, allowing for greater flexibility in coverage enhancement and interference mitigation. The integration of active STAR-RIS further amplifies these benefits by overcoming path loss limitations [22].

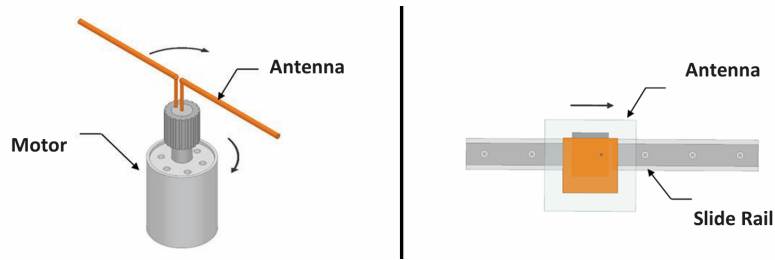


Figure 2.6: Movement mechanisms for Movable Antennas [23]

2.4 Movable Antennas: A Key Enabler for Dynamic and Adaptive Wireless Systems

As wireless communication systems continue to evolve, the demand for increased spectral efficiency, energy efficiency, and adaptability has driven the exploration of novel antenna technologies. Traditionally, wireless networks have relied on fixed-position antennas (FPAs), where BSs and user equipment (UE) operate with predetermined antenna configurations. While these systems have been optimized over multiple generations of cellular networks, they suffer from fundamental limitations, particularly the inability to fully utilize the wireless channel spatial variation, or spatial degree of freedom (DoF), in the given regions where the transmitter and receiver reside due to the discrete form of antennas or antenna arrays deployed at fixed positions [24]. MAs have emerged as a transformative solution to enhance wireless communication by introducing spatial degrees of freedom in addition to traditional waveform and beamforming techniques. Unlike conventional fixed-position antennas, MAs can dynamically adjust their locations within a predefined region, such as moving along a track [24]. The repositioning of MAs is typically achieved through precise movement mechanisms, including stepper motors or mechanical slides shown in Fig 2.6, allowing fine-tuned adjustments in antenna placement. By intelligently adapting their positions, MAs can maximize received signal power, mitigate interference, improve spatial diversity, and enhance overall network robustness [24], [25], [26]. In addition to mechanical movement, MAs can be integrated with beamforming strategies, leveraging a combination of spatial and electronic beamforming techniques to enhance signal directionality.

MAs can be classified based on various key attributes, with the degree of mobility being the most

prominent. One-dimensional (1D) MAs are restricted to movement along a single axis, such as a linear track or a rotational hinge, making them well-suited for linear antenna arrays and fixed installations with limited space. Two-dimensional (2D) MAs, on the other hand, can move freely within a planar region, allowing them to adjust both their horizontal and vertical positions. This additional flexibility provides significant benefits in terms of beam steering and interference avoidance. The most advanced type, three-dimensional (3D) MAs, can move freely within a volumetric space and are typically used in aerial platforms, UAV-assisted communications, and robotic networks.

In conclusion, as 6G and beyond continue to push the limits of wireless communication, MAs provide a flexible framework that adapts to evolving network demands. Furthermore, the integration of MAs with other advanced technologies, such as RIS and massive MIMO, opens the door for joint optimization of spatial and EM parameters, leading to unprecedented gains in wireless system performance.

2.5 Deep Learning in Modern Wireless Communication Systems

The use of deep learning (DL) in wireless communication systems has gained significant momentum in recent years, driven by the growing complexity of modern networks and the increasing availability of large datasets. Initially, wireless communication systems were designed based on classical optimization and signal processing techniques, which were highly effective but limited in their ability to handle the growing intricacies of contemporary networks. With the advent of machine learning (ML), and more specifically deep learning, wireless networks began to adopt AI-driven solutions capable of processing vast amounts of data and learning from patterns in ways that traditional methods could not. Early applications of deep learning in wireless networks focused on tasks like signal detection, channel estimation, and interference management. As the field advanced, the potential for deep learning to revolutionize network design, management, and optimization became evident, and its applications expanded into areas such as network slicing, spectrum management, traffic prediction, and even security.

Deep learning in wireless networks leverages neural networks with multiple layers—often referred to as deep neural networks (DNNs)—to model complex relationships in data. The ability

of deep learning algorithms to automatically extract features and adapt to dynamic environments makes them particularly suitable for solving the challenges inherent in modern communication systems. With networks becoming more heterogeneous, incorporating diverse technologies such as massive MIMO, small cells, and RIS, deep learning offers a powerful tool for dealing with the nonlinearities, uncertainties, and high-dimensional data involved. As a result, the deployment of deep learning techniques in wireless systems is increasingly seen as essential for improving the performance, efficiency, and adaptability of next-generation wireless networks, including 5G and beyond.

There are several types of deep learning approaches used in wireless networks, each tailored to specific tasks and challenges. The three primary categories of deep learning methods are supervised learning, unsupervised learning, and reinforcement learning. These methods differ in how they are trained, the types of data they require, and the kinds of problems they are best suited to solve.

Supervised Learning is the most widely used form of deep learning in wireless communication systems. In supervised learning, the model is trained on labeled data, meaning that both the input data and the corresponding output (or labels) are provided during the training process. This allows the model to learn a mapping from inputs to outputs by minimizing the error between predicted and actual outcomes. In wireless networks, supervised learning is used in applications such as channel state information (CSI) prediction, signal classification, modulation recognition, and beamforming design. The primary advantage of supervised learning is that it can achieve high accuracy when sufficient labeled data is available, which is ideal for applications requiring precise control and optimization, such as beamforming in massive MIMO systems.

Unsupervised Learning, on the other hand, does not rely on labeled data and instead aims to identify patterns or structures in the input data. In unsupervised learning, algorithms try to group similar data points together or reduce the dimensionality of the data for more efficient processing. This type of learning is particularly useful in wireless networks for applications such as clustering, anomaly detection, and feature extraction. For instance, unsupervised learning techniques can be employed to detect unusual traffic patterns or interference sources in the network, or to discover hidden structures within the network that could be leveraged for optimization. One popular unsupervised learning algorithm used in wireless networks is the autoencoder, which is used for

dimensionality reduction in large datasets or for noise reduction in communication channels.

Reinforcement Learning (RL) represents a more dynamic approach to deep learning, where an agent interacts with an environment and learns through trial and error to maximize a reward function. In wireless networks, RL is particularly valuable in scenarios where the network environment is highly dynamic, and traditional optimization techniques struggle to adapt in real time. RL can be applied in various areas of wireless networks, such as power control, resource allocation, and dynamic spectrum management. For example, an RL-based approach might enable a BS to learn the optimal transmission power levels over time to maximize coverage while minimizing interference. One of the key strengths of RL is its ability to make decisions based on real-time feedback, making it ideal for applications where the network's state changes continuously.

The integration of deep learning into wireless communication systems is not without its challenges. One of the primary obstacles is the need for large datasets to train deep learning models effectively, which is often not readily available in real-world wireless systems. Additionally, deep learning models are computationally intensive and require significant processing power, making them challenging to deploy in resource-constrained environments such as mobile devices or IoT systems. To address these challenges, researchers are focusing on developing more efficient models that require less data and computational power, as well as exploring edge computing and federated learning approaches to distribute the computational load across network nodes.

In conclusion, deep learning has become an indispensable tool in the advancement of wireless communication systems, enabling more intelligent, efficient, and adaptive networks. By leveraging supervised learning, unsupervised learning, and reinforcement learning, deep learning techniques offer solutions to a wide range of challenges in modern wireless networks. As the technology continues to evolve, it is expected that deep learning will play an even more central role in optimizing wireless systems, improving spectral efficiency, reducing latency, and enhancing overall network performance. The ongoing integration of AI and machine learning with next-generation networks promises to drive the development of smarter and more resilient wireless communication systems.

Chapter 3

RIS for Enhancing Sum Rate Performance in C-RSMA-Enabled Downlink Wireless Networks

3.1 Introduction

This chapter examines the role of RIS in enhancing the performance of Cooperative Rate Splitting Multiple Access within a downlink wireless network. Particular emphasis is placed on the potential of active STAR-RIS in improving system efficiency, alongside a comparative analysis with other RIS configurations, including those discussed in Section 2.3. The study aims to highlight the advantages and key differences among various RIS architectures in the context of C-RSMA, providing valuable insights into their impact on network performance.

In this context, we investigate a downlink wireless network where a multi-antenna BS utilizes an active STAR-RIS to enhance system performance. To further improve coverage and spectral efficiency, users with favorable channel conditions act as full-duplex relays, assisting weaker users by forwarding the common stream. Our objective is to maximize the network sum rate by jointly optimizing the BS beamformers, active STAR-RIS reflection and transmission coefficients, common stream power allocation, and the relay users' transmit power. This optimization is subject to

multiple constraints, including minimum rate requirements for all users, hardware limitations of the active STAR-RIS, and power budget constraints at the BS, active STAR-RIS, and relaying users. To address this non-convex problem, we propose an alternating optimization framework based on successive convex approximation (SCA). Extensive simulations validate the effectiveness of our approach, demonstrating significant performance gains over conventional baseline methods.

However, while conventional optimization methods, such as SCA, have shown effectiveness in achieving high performance, they often suffer from high computational overhead and are not well-suited for real-time applications. Given the increasing demand for time-efficient solutions in modern wireless systems, it becomes crucial to develop methods that can not only deliver high performance but also meet the stringent real-time requirements.

To overcome these limitations, we propose a solution based on Deep Reinforcement Learning. Leveraging the recent advancements in DRL, which has demonstrated great success in solving complex optimization problems, we aim to apply this approach to optimize the active STAR-RIS-assisted C-RSMA configuration. The DRL model offers the potential for real-time decision-making, significantly reducing computational time compared to conventional optimization techniques. Through simulations and performance analysis, we demonstrate the feasibility and advantages of this DRL-based approach in solving the optimization problem and analyze its trade-offs compared to the previously discussed SCA-based solution.

3.2 State of The Art

In the realm of wireless communication, the quest for enhanced downlink performance is pivotal for advancing next-generation networks. Two key technologies driving this endeavor are reconfigurable intelligent surfaces and rate-splitting multiple access. RISs have emerged as a transformative technology in reshaping wireless propagation environments, offering improvements in signal strength, interference reduction, and coverage expansion. Unlike passive RIS, active simultaneously transmitting and reflecting RIS amplifies reflected signals while actively transmitting, bolstering communication reliability [22]. Meanwhile, RSMA combines spatial division multiple access (SDMA) and non-orthogonal multiple access (NOMA) techniques, dividing transmitted data into

common and private streams to optimize downlink performance [10].

Recent studies have highlighted RSMA's superiority over conventional schemes. For instance, RSMA has shown significant performance advantages over NOMA, SDMA, and orthogonal frequency-division multiple access in maximizing the network spectral efficiency [27] and the network energy efficiency [28]. However, RSMA faces challenges regarding the achievable rate of the common stream, limited by users with the most challenging channel conditions. To address this, cooperative RSMA schemes based on half-duplex (HD) and full-duplex (FD) have been proposed [29, 30, 11, 31]. A recent work [21] demonstrated the efficacy of STAR-RIS in enhancing the minimum user rate of FD C-RSMA in a multi-user scenario.

While previous research has demonstrated performance improvements with passive STAR-RIS in downlink communication systems using RSMA, it remains uncertain whether an active STAR-RIS would yield even greater enhancements. The literature notably lacks comprehensive investigations into the impact of an active STAR-RIS on enhancing the overall performance of FD C-RSMA in downlink communication scenarios. This gap serves as the primary motivation for our study.

On another side, Deep Reinforcement Learning has emerged as a powerful method for solving complex optimization problems across various domains. Building on reinforcement learning, DRL uses deep neural networks to approximate value functions or policies, enabling decision-making in high-dimensional, continuous spaces. Over the past decade, DRL has delivered impressive results in fields such as robotics, game playing, and autonomous driving, where dynamic decision-making and real-time performance are critical. While DRL shows promise, many wireless optimization problems have traditionally been addressed using Successive Convex Approximation. SCA provides high-performance solutions, especially for non-convex problems, but its main drawback is high computational complexity. The iterative process required by SCA can be time-consuming, particularly in large-scale systems with real-time constraints. For instance, in RIS-assisted systems like the one proposed in this chapter, optimizing beamformers, power allocation, and RIS reflection coefficients via multiple iterations introduces significant computational overhead. As system size or user count increases, the time required to converge to an optimal solution becomes prohibitive, making SCA impractical for real-time applications.

To address this, we propose DRL as a solution by formulating the optimization problem as a

reinforcement learning task. DRL can significantly reduce optimization time by learning optimal policies through interaction with the environment, eliminating the need for iterative computation. By training a DRL model to optimize the active STAR-RIS-assisted framework discussed earlier, we aim to provide a time-efficient solution capable of making real-time decisions without exhaustive computation.

3.3 Contributions

Our main contributions in this chapter include:

- We analyze the performance of an active STAR-RIS in assisting FD C-RSMA in a down-link multiple-input single-output (MISO) system, where a BS serves K users, with S users assisting in the transmission for the remaining users.
- We investigate the joint optimization of the BS precoding vectors, active STAR-RIS reflection and transmission matrices, common stream split, and the transmit powers of strong users to maximize the network sum rate while meeting minimum rate constraints, adhering to active STAR-RIS hardware constraints, and ensuring the power budget at the BS, the active STAR-RIS, and each strong user.
- We propose an SCA-based alternating optimization (AO) algorithm to address this non-convex optimization problem.
- We conduct rigorous simulations to demonstrate significant performance gains from the cooperation between users and the inclusion of active STAR-RIS. Our results show maximum sum rates with minimal BS power, achieving a remarkable 20.3% improvement at 32 dBm compared to the second-ranked baseline. Additionally, a modest active STAR-RIS power of 24 dBm yields an approximately 6% gain over the same baseline.
- We develop a DRL model to optimize the performance of the proposed STAR-RIS-assisted FD C-RSMA system. The trained model jointly optimizes the BS precoding vectors, active STAR-RIS reflection and transmission matrices, common stream split, and the transmit powers of strong users. The objective is to maximize the achievable sum rate while meeting the

system constraints.

- We propose a novel training framework based on the actor-critic architecture to handle the continuous state and action spaces of the optimization variables. Our approach utilizes two actor-critic models, each focusing on a subset of variables, to improve scalability by reducing the state space dimension.
- We conduct simulations under various conditions, comparing the proposed model with an SCA-based convex optimization baseline to evaluate its strengths and weaknesses.

3.4 Performance Analysis of RIS in C-RSMA-Enabled Downlink Wireless Networks

3.4.1 System Model

3.4.1.1 Network Model

We examine a downlink communication system with an active STAR-RIS equipped with N elements as illustrated in Fig. 3.1. In this configuration, a BS equipped with N_t transmit antennas delivers services to K single-antenna users ($N_t \geq K$) on both sides of the STAR-RIS.

Without loss of generality, $\mathcal{K}_r \triangleq \{1, 2, \dots, K_r\}$ is the set of users on the reflection side, while $\mathcal{K}_t \triangleq \{(K_r + 1), \dots, K\}$ contains users on the transmission side. The BS is assumed to have knowledge of channel state information (CSI) for all links within the system. Consequently, the BS identifies the S strong users with the strongest channel gains, among the channels between the BS and the K users. Without loss of generality, we assume that the strong users are the first S users on the reflection side ($S < K_r$). In addition, each strong user serves as an FD relay to transmit signals to the remaining weak users.

We denote $\mathbf{h}_k \in \mathbb{C}^{N_t \times 1}$, $\mathbf{f}_k \in \mathbb{C}^{1 \times N}$, and $h_{s,w}$, respectively, as the direct channel from the BS to user k , the channel from user k to the RIS, and the channel from strong user s to weak user w , $\forall k \in \mathcal{K} \triangleq \{1, \dots, K\}$, $\forall s \in \mathcal{S} \triangleq \{1, \dots, S\}$ and $\forall w \in \mathcal{W} \triangleq \{S + 1, \dots, K\}$.

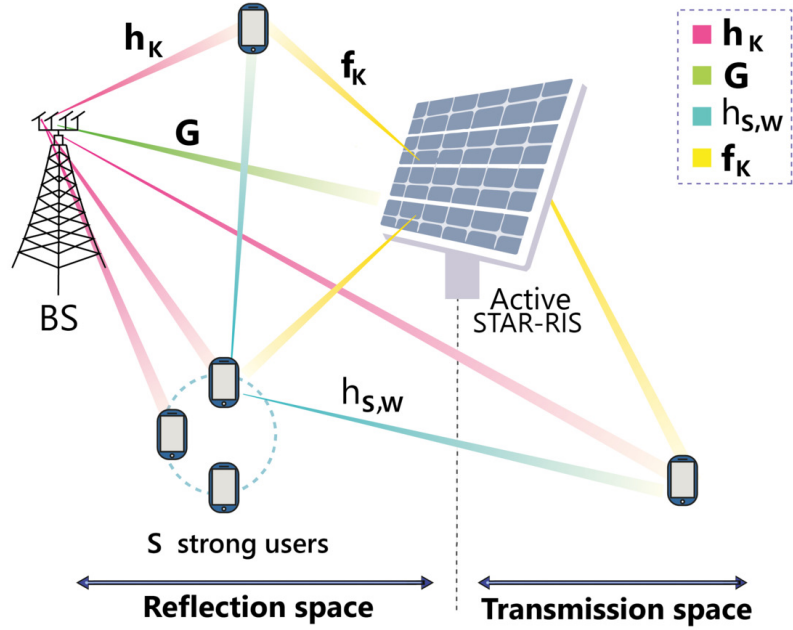


Figure 3.1: System model

Moreover, $\mathbf{G} \in \mathbb{C}^{N \times N_t}$ represents the channel between the BS and the RIS and we denote $n_k \sim \mathcal{CN}(0, \sigma_k^2) \forall k \in \mathcal{K}$, referring to the additive white Gaussian noise (AWGN).

3.4.1.2 Transmission Model

The transmission model comprises two phases:

Direct Transmission Phase

In this phase, the BS partitions each user's message W_k into common ($W_{c,k}$) and private ($W_{p,k}$) components, collectively encoding common parts into a unified common stream (s_c) and private parts into individual private streams (s_1, \dots, s_K). These streams, denoted as $\mathbf{s} = [s_c, s_1, \dots, s_K]^T \in \mathbb{C}^{(K+1) \times 1}$, undergo linear precoding with a precoder $\mathbf{p} = [\mathbf{p}_c, \mathbf{p}_1, \dots, \mathbf{p}_K]^T \in \mathbb{C}^{N_t \times (K+1)}$, with $\mathbf{p}_c, \mathbf{p}_k \in \mathbb{C}^{N_t \times 1} \forall k \in \mathcal{K}$, ensuring $\mathbb{E}\{\mathbf{s}\mathbf{s}^H\} = I_{(K+1)}$. The transmitted signal from the BS is represented as $\mathbf{x} = \mathbf{p}_c s_c + \sum_{k=1}^K \mathbf{p}_k s_k$.

Cooperative Transmission Phase

Strong users broadcast the common stream to weak users, who then combine it with received signals from the BS and strong users to decode the common stream. Subsequently, weak users apply SIC to decode their private streams. Strong users operate in full-duplex (FD) relaying mode, enabling simultaneous execution of direct and cooperative transmission phases within the same time-slot, albeit introducing self-interference (SI) [31].

3.4.1.3 Active STAR-RIS Model

The active STAR-RIS possesses the capability to concurrently amplify, transmit, and reflect signals through the use of amplifiers and phase shifters. Each element of the active STAR-RIS can independently adjust the amplitude and phase-shift of incident signals using distinct components, as demonstrated in [32]. The reflection ($p = r$) and transmission ($p = t$) matrices for active STAR-RIS are defined as $\Theta_p = \text{diag}(\mathbf{v}_p) \in \mathbb{C}^{N \times N}$ where the beamforming vector \mathbf{v}_p is defined as $\mathbf{v}_p = [\sqrt{\beta_{p1}}e^{j\theta_{p1}}, \dots, \sqrt{\beta_{pN}}e^{j\theta_{pN}}]^T$. Note that, for each $n \in [1, N]$, the amplification coefficients verify $\beta_{t_n} + \beta_{r_n} \leq \beta_{max}$, and the phase shifts are within the range $[0, 2\pi)$.

Additionally, our approach can be extended to handle discrete phase shifts by mapping the obtained continuous angles to the nearest discrete values within a quantized set of feasible phase shifts [33]. With sufficient granularity, the algorithm's performance would experience only a slight decrease compared to the continuous case.

3.4.1.4 Signal Model and Rate Analysis

The received signal at strong user s is given as

$$y_s = \tilde{\mathbf{h}}_s^H \mathbf{x} + \mathbf{f}_s \Theta_r \mathbf{v}_{RIS} + h_{SI,s} \sqrt{p_{r,s}} \hat{\mathbf{s}}_{c,s} + n_s, \quad \forall s \in \mathcal{S}, \quad (1)$$

where $\tilde{\mathbf{h}}_s \in \mathbb{C}^{N_t \times 1}$ is expressed as $\tilde{\mathbf{h}}_s^H = \mathbf{h}_s^H + \mathbf{f}_s \Theta_r \mathbf{G}$ and $\mathbf{v}_{RIS} \in \mathbb{C}^{N \times 1}$ denotes the noise added by the active STAR-RIS while reflecting or transmitting the input signal with each entry following $\mathbf{v}_{RIS} \sim \mathcal{CN}(0, \sigma_{RIS}^2)$ as stated in [22]. $p_{r,s}$ and $h_{SI,s}$ are respectively, the transmit relaying power and the self-interference channel for strong user s resulting from transmitting the

common stream to other weak users while receiving the signal from the BS, which follows $h_{SI,s} \sim \mathcal{CN}(0, \sigma_{SI,s}^2)$. Assuming that the common stream is decoded successfully and that the decoding delay is insignificant compared to the duration of one time slot [31], we have $\hat{s}_{c,s} = s_c(t - \tau_s) = s_c \forall s \in \mathcal{S}$, where t denotes the t^{th} time slot and τ_s is the delay caused by the decoding operation at user s . We note $\sigma_{t_k}^2 = \sigma_{RIS}^2 \|\mathbf{f}_k \Theta_r\|^2 + \sigma_k^2, \forall k \in \mathcal{K}_r$ and $\sigma_{t_k}^2 = \sigma_{RIS}^2 \|\mathbf{f}_k \Theta_t\|^2 + \sigma_k^2, \forall k \in \mathcal{K}_t$. Based on that, the achievable data rate at the strong user s to decode the common stream can be expressed as:

$$R_{c,s} = \log_2 \left(1 + \frac{|\tilde{\mathbf{h}}_s^H \mathbf{p}_c|^2}{\sum_{k \in \mathcal{K}} |\tilde{\mathbf{h}}_s^H \mathbf{p}_k|^2 + \sigma_{t_s}^2 + |h_{SI,s}|^2 p_{r,s}} \right), \forall s \in \mathcal{S}. \quad (2)$$

Afterward, the decoded common stream is removed from the total received signal via SIC and the strong user s decodes its private stream with the achievable rate given by:

$$R_{p,s} = \log_2 \left(1 + \frac{|\tilde{\mathbf{h}}_s^H \mathbf{p}_s|^2}{\sum_{\substack{k \in \mathcal{K} \\ k \neq s}} |\tilde{\mathbf{h}}_s^H \mathbf{p}_k|^2 + \sigma_{t_s}^2 + |h_{SI,s}|^2 p_{r,s}} \right), \forall s \in \mathcal{S}. \quad (3)$$

Conversely, the weak users receive two RIS-assisted signals, one from the BS (due to direct transmission) and the other coming from the strong users (due to cooperative transmission) during the same time slot [31]. Thus, the received signal at weak user w can be expressed as

$$y_w = \tilde{\mathbf{h}}_w^H \mathbf{x} + \sum_{s \in \mathcal{S}} \tilde{h}_{s,w}^* \sqrt{p_{r,s}} s_c + \mathbf{f}_w \Theta_p \mathbf{v}_{RIS} + n_w, \forall w \in \mathcal{W}, \quad (4)$$

where $\tilde{\mathbf{h}}_w \in \mathbb{C}^{N_t \times 1}$ is expressed as $\tilde{\mathbf{h}}_w^H = \mathbf{h}_w^H + \mathbf{f}_w \Theta_p \mathbf{G}$, $\tilde{h}_{s,w} \in \mathbb{C}$ is defined as $\tilde{h}_{s,w}^* = h_{s,w}^* + \mathbf{f}_w \Theta_p \mathbf{f}_s^H$. To detect the common stream at the end of cooperative transmission, we assume that weak users can resolve the received signal. Consequently, these signals can be synchronized and combined using maximal ratio combining (MRC) [31]. Thus, the achievable rate for decoding the common stream at weak user w is as follows:

$$R_{c,w} = \log_2 \left(1 + \frac{|\tilde{\mathbf{h}}_w^H \mathbf{p}_c|^2}{\sum_{k \in \mathcal{K}} |\tilde{\mathbf{h}}_w^H \mathbf{p}_k|^2 + \sigma_{t_w}^2} + \sum_{s \in \mathcal{S}} \frac{|\tilde{h}_{s,w}^*|^2 p_{r,s}}{\sigma_{t_w}^2} \right), \forall w \in \mathcal{W}. \quad (5)$$

Upon successful decoding of the common stream, it is subtracted from the received signal, and hence, the attainable rate for weak user w to decode its private stream can be given as

$$R_{p,w} = \log_2 \left(1 + \frac{|\tilde{\mathbf{h}}_w^H \mathbf{p}_w|^2}{\sum_{\substack{k \in \mathcal{K} \\ k \neq w}} |\tilde{\mathbf{h}}_w^H \mathbf{p}_k|^2 + \sigma_{t_w}^2} \right), \forall w \in \mathcal{W}. \quad (6)$$

To ensure successful decoding of the common stream by all users, we determine the achievable data rate R_c as the minimum among the achievable common rates for the K users, expressed as $R_c = \min(R_{c,1}, \dots, R_{c,K})$. R_c serves as a shared resource among all users, with $R_c = \sum_{k=1}^K C_k$, where C_k represents the portion of R_c allocated to transmit $W_{c,k}$. Thus, the achievable rate for user k is $R_k = C_k + R_{p,k}, \forall k \in \{1, 2, \dots, K\}$.

3.4.2 Problem Formulation

In this paper, we aim to jointly design the BS transmit beamforming \mathbf{p} , active STAR-RIS reflection and transmission beamforming matrices, i.e., Θ_r and Θ_t , common stream split $\mathbf{c} = [C_1, \dots, C_K]$ and the transmit relaying power $p_{r,s}$ at each strong user to maximize the network sum rate, while satisfying the minimum rate constraints, active STAR-RIS hardware constraints, the given power budget P_{RIS} at the active STAR-RIS, P_{BS} at the BS and P_s at each strong user s . Consequently, this optimization problem can be formulated as:

$$\mathcal{P} : \max_{\substack{\mathbf{p}, \mathbf{p}_r, \mathbf{c}, \\ \Theta_r, \Theta_t}} \sum_{k \in \mathcal{K}} R_k \quad (7a)$$

$$\text{s.t. } \|\mathbf{p}_c\|^2 + \sum_{j \in \mathcal{K}} \|\mathbf{p}_j\|^2 \leq P_{BS}, \quad (7b)$$

$$\sum_{j \in \mathcal{K}} \|\Theta_r \mathbf{G} \mathbf{p}_j\|^2 + \|\Theta_r \mathbf{G} \mathbf{p}_c\|^2 + \sum_{j \in \mathcal{K}} \|\Theta_t \mathbf{G} \mathbf{p}_j\|^2 + \|\Theta_t \mathbf{G} \mathbf{p}_c\|^2 + \sum_{s \in \mathcal{S}} \|\Theta_r \mathbf{f}_s^H\|^2 p_{r,s} + \sum_{s \in \mathcal{S}} \|\Theta_t \mathbf{f}_s^H\|^2 p_{r,s} + \sigma_{RIS}^2 (\|\Theta_r\|_F^2 + \|\Theta_t\|_F^2) \leq P_{RIS}, \quad (7c)$$

$$0 \leq p_{r,s} \leq P_s, \quad \forall s \in \mathcal{S}, \quad (7d)$$

$$R_k \geq R_{min,k}, \quad \forall k \in \mathcal{K}, \quad (7e)$$

$$\sum_{i \in \mathcal{K}} C_i \leq R_{c,k}, \quad \forall k \in \mathcal{K}, \quad (7f)$$

$$C_i \geq 0, \quad \forall i \in \mathcal{K}, \quad (7g)$$

$$\beta_{t_n} \geq 0, \quad \beta_{r_n} \geq 0, \quad \forall n \in \{1 \dots N\}, \quad (7h)$$

$$\beta_{t_n} + \beta_{r_n} \leq \beta_{max}, \quad \forall n \in \{1 \dots N\}, \quad (7i)$$

$$|e^{j\theta_{r_i}}| = 1, |e^{j\theta_{t_i}}| = 1, \forall i \in \{1 \dots N\}, \quad (7j)$$

where (7b), (7c), and (7d) guarantee compliance with the power budgets at the BS, the active STAR-RIS, and each of the strong users, respectively. (7e) ensures the minimum quality of service required by each user in the system, and (7f) establishes that $R_c = \min(R_{c,1}, \dots, R_{c,K})$ as explained in the previous section. Lastly, (7h)-(7j) are the active STAR-RIS hardware constraints. It is observed that \mathcal{P} is a non-convex optimization problem due to the non-convex objective function (7a) and the non-convex constraints (7e), (7f), and the unit modulus constraint in (7j).

3.4.3 Solution Approach

Due to its intractability, the original problem, i.e., \mathcal{P} , is divided into two sub-problems that are solved alternately until convergence. In this section, we present the formulation and solution of each sub-problem, concluding with a description of the final algorithm.

Optimizing the BS beamforming vector \mathbf{p} , the relaying power vector \mathbf{p}_r and the common splits vector \mathbf{c}

In this sub-problem, we fix Θ_t , Θ_r and optimize \mathbf{p} , \mathbf{p}_r and \mathbf{c} . By introducing the slack variables $\gamma_p = [\gamma_{p,1}, \dots, \gamma_{p,K}]$ and $\gamma_c = [\gamma_{c,1}, \dots, \gamma_{c,K}]$, the problem can be reformulated as follows.

$$\max_{\substack{\mathbf{p}_r, \mathbf{p}, \\ \mathbf{c}, \gamma_p, \gamma_c}} \sum_{k \in \mathcal{K}} (C_k + \log_2(1 + \gamma_{p,k})) \quad (8a)$$

$$\text{s.t. } C_k + \log_2(1 + \gamma_{p,k}) \geq R_{min,k}, \quad \forall k \in \mathcal{K}, \quad (8b)$$

$$\frac{|\tilde{\mathbf{h}}_s^H \mathbf{p}_s|^2}{\sum_{\substack{k \in \mathcal{K} \\ k \neq s}} |\tilde{\mathbf{h}}_s^H \mathbf{p}_k|^2 + \sigma_{t_s}^2 + |h_{SI,s}|^2 p_{r,s}} \geq \gamma_{p,s}, \quad \forall s \in \mathcal{S}, \quad (8c)$$

$$\frac{|\tilde{\mathbf{h}}_w^H \mathbf{p}_w|^2}{\sum_{\substack{k \in \mathcal{K} \\ k \neq w}} |\tilde{\mathbf{h}}_w^H \mathbf{p}_k|^2 + \sigma_{t_w}^2} \geq \gamma_{p,w}, \quad \forall w \in \mathcal{W}, \quad (8d)$$

$$\sum_{j \in \mathcal{K}} C_j \leq \log_2(1 + \gamma_{c,k}), \quad \forall k \in \mathcal{K}, \quad (8e)$$

$$\frac{|\tilde{\mathbf{h}}_s^H \mathbf{p}_c|^2}{\sum_{k \in \mathcal{K}} |\tilde{\mathbf{h}}_s^H \mathbf{p}_k|^2 + \sigma_{t_s}^2 + |h_{SI,s}|^2 p_{r,s}} \geq \gamma_{c,s}, \quad \forall s \in \mathcal{S}, \quad (8f)$$

$$\frac{|\tilde{\mathbf{h}}_w^H \mathbf{p}_c|^2}{\sum_{k \in \mathcal{K}} |\tilde{\mathbf{h}}_w^H \mathbf{p}_k|^2 + \sigma_{t_w}^2} + \frac{\sum_{s \in \mathcal{S}} |\tilde{\mathbf{h}}_{s,w}^*|^2 p_{r,s}}{\sigma_{t_w}^2} \geq \gamma_{c,w}, \quad \forall w \in \mathcal{W}, \quad (8g)$$

$$(7b) - (7d), (7g). \quad (8h)$$

It can be seen that the non-convexity is alleviated from the objective function as well as constraints (8b) and (8e), however, constraints (8c)-(8d) and (8f)-(8g) still need to be convexified. For that, we introduce two other slack variables $\phi_p = [\phi_{p,1}, \dots, \phi_{p,K}]$ and $\phi_c = [\phi_{c,1}, \dots, \phi_{c,K}]$. Therefore, the mentioned constraints can be rewritten as follows.

$$\frac{|\tilde{\mathbf{h}}_k \mathbf{p}_k|^2}{\phi_{p,k}} \geq \gamma_{p,k}, \quad \forall k \in \mathcal{K}, \quad (9)$$

$$\frac{|\tilde{\mathbf{h}}_k \mathbf{p}_c|^2}{\phi_{p,k}} \geq \gamma_{c,k}, \quad \forall k \in \mathcal{K}, \quad (10)$$

$$\phi_{p,s} \geq \sum_{\substack{k \in \mathcal{K} \\ k \neq s}} |\tilde{\mathbf{h}}_s^H \mathbf{p}_k|^2 + \sigma_{t_s}^2 + |h_{SI,s}|^2 p_{r,s}, \quad \forall s \in \mathcal{S}, \quad (11)$$

$$\phi_{p,w} \geq \sum_{\substack{k \in \mathcal{K} \\ k \neq w}} |\tilde{\mathbf{h}}_w^H \mathbf{p}_k|^2 + \sigma_{t_w}^2, \quad \forall w \in \mathcal{W}, \quad (12)$$

$$\phi_{c,s} \geq \sum_{k \in \mathcal{K}} |\tilde{\mathbf{h}}_s^H \mathbf{p}_k|^2 + \sigma_{t_s}^2 + |h_{SI,s}|^2 p_{r,s}, \quad \forall s \in \mathcal{S}, \quad (13)$$

$$\phi_{c,w} \geq \sum_{k \in \mathcal{K}} |\tilde{\mathbf{h}}_w^H \mathbf{p}_k|^2 + \sigma_{t_w}^2, \quad \forall w \in \mathcal{W}. \quad (14)$$

Constraints (9) and (10) are still non-convex and will be iteratively approximated using Taylor's first-order expansion, respectively, around the points from the previous iteration $(\mathbf{p}_k^o, \phi_{p,k}^o)$ and $(\mathbf{p}_c^o, \phi_{c,k}^o) \forall k \in \mathcal{K}$ as follows [28].

$$\frac{2 \Re(\mathbf{p}_k^{oH} \tilde{\mathbf{h}}_k \tilde{\mathbf{h}}_k^H \mathbf{p}_k^H)}{\phi_{p,k}^o} - \frac{|\tilde{\mathbf{h}}_k^H \mathbf{p}_k^{oH}|^2}{\phi_{p,k}^{o,2}} \phi_{p,k} \geq \gamma_{p,k}, \quad \forall k \in \mathcal{K}, \quad (15)$$

$$\frac{2 \Re(\mathbf{p}_c^{oH} \tilde{\mathbf{h}}_k \tilde{\mathbf{h}}_k^H \mathbf{p}_c^H)}{\phi_{p,c}^o} - \frac{|\tilde{\mathbf{h}}_k^H \mathbf{p}_c^{oH}|^2}{\phi_{c,k}^{o,2}} \phi_{c,k} \geq \gamma_{c,k}, \quad \forall k \in \mathcal{K}. \quad (16)$$

Using these approximations, first sub-problem is formulated as:

$$\max_{\substack{\mathbf{p}_r, \mathbf{p}, \mathbf{c}, \gamma_p \\ \phi_c, \phi_p, \gamma_c}} \sum_{k \in \mathcal{K}} (C_k + \log_2(1 + \gamma_{p,k})), \quad (17a)$$

$$\text{s. t. } (8b), (8e), (11) - (16), \quad (17b)$$

$$(7b) - (7d), (7g). \quad (17c)$$

One can see that problem (17) is a convex problem, which can be easily solved using a convex solver such as CVX [34].

Optimizing the Active STAR-RIS reflection and transmission matrices Θ_r and Θ_t

In this sub-problem, the optimization variables are Θ_r and Θ_t whilst all the other variables are fixed. Constraints (7i)–(7j) are substituted by the following constraint.

$$|[\mathbf{v}_t]_n|^2 + |[\mathbf{v}_r]_n|^2 \leq \beta_{max}, \forall n \in \{1 \dots N\}. \quad (18)$$

Constraints (8b) and (8e) from the previous sub-problem remain unchanged, whereas approximations for (8c), (8d), (8f), and (8g) will differ slightly but employing a similar technique as follows.

$$\phi_{p,s} \geq \sum_{\substack{k \in \mathcal{K} \\ k \neq s}} |\tilde{\mathbf{h}}_s^H \mathbf{p}_k|^2 + \sigma_{RIS}^2 \|\mathbf{f}_s \Theta_r\|^2 + |h_{SI,s}|^2 p_{r,s}, \forall s \in \mathcal{S}, \quad (19)$$

$$\phi_{p,w} \geq \sum_{\substack{k \in \mathcal{K} \\ k \neq w}} |\tilde{\mathbf{h}}_w^H \mathbf{p}_k|^2 + \sigma_{RIS}^2 \|\mathbf{f}_w \Theta_r\|^2, \forall w \in \mathcal{K}_r \cap \mathcal{W}, \quad (20)$$

$$\phi_{p,w} \geq \sum_{\substack{k \in \mathcal{K} \\ k \neq w}} |\tilde{\mathbf{h}}_w^H \mathbf{p}_k|^2 + \sigma_{RIS}^2 \|\mathbf{f}_w \Theta_t\|^2, \forall w \in \mathcal{K}_t \cap \mathcal{W}, \quad (21)$$

$$\phi_{c,s} \geq \sum_{k \in \mathcal{K}} |\tilde{\mathbf{h}}_s^H \mathbf{p}_c|^2 + \sigma_{RIS}^2 \|\mathbf{f}_s \Theta_r\|^2 + |h_{SI,s}|^2 p_{r,s}, \forall s \in \mathcal{S}, \quad (22)$$

$$\phi_{c,w} \geq \sum_{k \in \mathcal{K}} |\tilde{\mathbf{h}}_w^H \mathbf{p}_c|^2 + \sigma_{RIS}^2 \|\mathbf{f}_w \Theta_r\|^2, \forall w \in \mathcal{K}_r \cap \mathcal{W}, \quad (23)$$

$$\phi_{c,w} \geq \sum_{k \in \mathcal{K}} |\tilde{\mathbf{h}}_w^H \mathbf{p}_c|^2 + \sigma_{RIS}^2 \|\mathbf{f}_w \Theta_t\|^2, \forall w \in \mathcal{K}_t \cap \mathcal{W}, \quad (24)$$

where the following variables are in terms of \mathbf{v}_r and \mathbf{v}_t ,

$$\Theta_r = \text{diag}(\mathbf{v}_r),$$

$$\Theta_t = \text{diag}(\mathbf{v}_t),$$

$$\tilde{\mathbf{h}}_s^H = \mathbf{h}_s^H + \mathbf{f}_s \text{diag}(\mathbf{v}_r) G, \quad \forall s \in \mathcal{S},$$

$$\tilde{\mathbf{h}}_w^H = \mathbf{h}_w^H + \mathbf{f}_w \text{diag}(\mathbf{v}_r) G, \quad \forall w \in \mathcal{K}_r \cap \mathcal{W},$$

$$\tilde{\mathbf{h}}_w^H = \mathbf{h}_w^H + \mathbf{f}_w \text{diag}(\mathbf{v}_t) G, \quad \forall w \in \mathcal{K}_t \cap \mathcal{W}.$$

We further add two new slack variables $\omega_c = [\omega_{c,1}, \dots, \omega_{c,W}]$ and $\alpha_c = [\alpha_{c,1}, \dots, \alpha_{c,W}]$ to convexify the second fraction in the left term of constraint (8g) as follows.

$$\omega_{c,w} \geq \sigma_{RIS}^2 \|\mathbf{f}_w \text{diag}(\mathbf{v}_r)\|^2, \quad \forall w \in \mathcal{K}_r \cap \mathcal{W}, \quad (25)$$

$$\omega_{c,w} \geq \sigma_{RIS}^2 \|\mathbf{f}_w \text{diag}(\mathbf{v}_t)\|^2, \quad \forall w \in \mathcal{K}_t \cap \mathcal{W}, \quad (26)$$

$$\frac{\sum_{s \in \mathcal{S}} |\tilde{h}_{s,w}^*|^2 p_{r,s}}{\alpha_{c,w}} \geq \omega_{c,w}, \quad \forall w \in \mathcal{W}. \quad (27)$$

Constraints (9), (10) and (27) are approximated in an iterative manner similar to the technique used in (15) and (16), as follows.

$$\frac{2 \Re(\mathbf{p}_k^H \tilde{\mathbf{h}}_k^o \tilde{\mathbf{h}}_k^H \mathbf{p}_k^H)}{\phi_{p,k}^o} - \frac{|\tilde{\mathbf{h}}_k^{oH} \mathbf{p}_k^H|^2}{\phi_{p,k}^{o2}} \phi_{p,k} \geq \gamma_{p,k}, \quad \forall k \in \mathcal{K}, \quad (28)$$

$$\frac{2 \Re(\mathbf{p}_c^H \tilde{\mathbf{h}}_k^o \tilde{\mathbf{h}}_k^H \mathbf{p}_c^H)}{\phi_{c,k}^o} - \frac{|\tilde{\mathbf{h}}_k^{oH} \mathbf{p}_c^H|^2}{\phi_{c,k}^{o2}} \phi_{c,k} \geq \gamma_{c,k}, \quad \forall k \in \mathcal{K}, \quad (29)$$

$$\frac{2 \sum_{s \in \mathcal{S}} \Re(\tilde{h}_{s,w}^o \tilde{h}_{s,w}^*) p_{r,s}}{\alpha_{c,w}^o} - \frac{\sum_{s \in \mathcal{S}} |\tilde{h}_{s,w}^o|^2 p_{r,s}}{\alpha_{c,w}^{o2}} \alpha_{c,w} \geq \omega_{c,w}, \quad \forall w \in \mathcal{W}, \quad (30)$$

where $\phi_{c,k}^o$, $\phi_{p,k}^o$, $\tilde{h}_{s,w}^o$ and $\tilde{\mathbf{h}}_k^o$ denote the values of the variables obtained from the previous iteration of the algorithm. We recall that $\tilde{h}_{s,w}^* = h_{s,w}^* + \mathbf{f}_w \text{diag}(\mathbf{v}_r) \mathbf{f}_s^H$, $\forall w \in \mathcal{K}_r \cap \mathcal{W}$ and $\tilde{h}_{s,w}^* = h_{s,w}^* + \mathbf{f}_w \text{diag}(\mathbf{v}_t) \mathbf{f}_s^H$, $\forall w \in \mathcal{K}_t \cap \mathcal{W}$.

Algorithm 1 Joint Beamforming Optimization

- 1: **Input** $\mathbf{h}_k, \mathbf{f}_k, \sigma_k^2, R_{min,k} \forall k \in \mathcal{K}, \mathbf{G}, \sigma_{RIS}^2, P_m, P_{RIS}, P_{BS}, T_{max}, \delta_{th}, h_{SI,s}, h_{s,w}, \sigma_{SI,w}^2 \forall s \in \mathcal{S}, \forall w \in \mathcal{W}$
 - 2: **Output** BS beamforming \mathbf{p} , active STAR-RIS beamforming Θ_r and Θ_t , cooperative relaying power vector \mathbf{p}_r , common split \mathbf{c} and sum rate R_{sum}
 - 3: **Initialize:** $\mathbf{p}, \mathbf{p}_r, \mathbf{c}, \Theta_r, \Theta_t, t = 1, \delta = \infty, R_{sum} = 0$
 - 4: **while** $t \leq T_{max}$ and $\delta \geq \delta_{th}$ **do**
 - 5: $R_{pre} = R_{sum}$;
 - 6: Update \mathbf{c}, \mathbf{p} , and \mathbf{p}_r by solving (17);
 - 7: Update Θ_r and Θ_t by solving (31);
 - 8: $R_{sum} = \sum_{k=1}^K R_k$;
 - 9: $\delta = |R_{pre} - R_{sum}|$;
 - 10: $t = t + 1$;
 - 11: **end while**
-

Considering all the preceding, the second sub-problem is expressed as:

$$\max_{\substack{\mathbf{v}_r, \mathbf{v}_t, \gamma_p \\ \phi_c, \phi_p, \gamma_c}} \sum_{k \in \mathcal{K}} \log_2(1 + \gamma_{p,k}) \quad (31a)$$

$$\text{s. t. } (18) - (26), (28) - (30), \quad (31b)$$

$$(7c), (8b), (8e). \quad (31c)$$

Now, the second sub-problem is transformed into a convex optimization problem, which can be easily solved using CVX [34]. The finalized algorithm for our proposed SCA-based solution is presented in Algorithm 1. The algorithm requires initialization with a feasible initial point, consisting of the variables $\mathbf{p}, \mathbf{p}_r, \mathbf{c}, \Theta_r$ and Θ_t , that satisfies constraints (7b) – (7j).

3.4.4 Complexity and Convergence

One can see that each sub-problem is a second-order cone program that has the complexity of $(S_1^2 S_2)$, where S_1 and S_2 are the total numbers of variables and constraints, respectively. For sub-problem (17), we have $S_1^{(1)} = S + (5 + N_t)K$ and $S_2^{(1)} = 5K + 3S + 2W + 2$. For sub-problem (31), we have $S_1^{(2)} = S + (5 + N_t)K + 2N$ and $S_2^{(2)} = 14K + 5S - 3W + N + 4$. Therefore, the overall complexity of the AO algorithm is $O(T_{max} S_1^{(1)2} S_2^{(1)} + T_{max} S_1^{(2)2} S_2^{(2)})$, where T_{max} is the maximum number of iterations. The SCA method, along with constraints (7b), (7c), and (7d) ensure

the monotonic increase of the sum rate while establishing an upper bound, thereby guaranteeing the convergence of (17) [31]. Similarly, the SCA method, coupled with constraint (7c), ensures the convergence of (31). The convergence of both sub-problems ensures the overall convergence of the proposed AO algorithm [21].

3.4.5 Simulation Results and Discussion

This section provides a detailed exploration of the performance of the proposed C-RSMA active STAR-RIS scheme. To assess its effectiveness, we present numerous numerical examples and simulation results, and compare it against the following baseline schemes:

- **RSMA active STAR-RIS:** Within this framework, the BS communicates with users by employing RSMA, with additional support from the active STAR-RIS.
- **SDMA active STAR-RIS:** In this framework, the base station communicates with users using SDMA, further enhanced by the active STAR-RIS for additional support.
- **C-RSMA passive STAR-RIS:** In this scheme, the BS communicates with the users using C-RSMA with support provided by a passive STAR-RIS.
- **C-RSMA NO RIS:** In this baseline, the BS communicates with users using C-RSMA.
- **RSMA NO RIS:** In this baseline, the downlink communication is ensured using RSMA.

Simulation Setup

The simulation setup for the considered system model is depicted in Fig. 3.2. The BS is situated at coordinates (0 m, 10 m, 10 m), while the active STAR-RIS is positioned at (100 m, 10 m, 10 m). Weak and strong users are uniformly distributed within two circular zones, each spanning a radius of 10 meters. The two zones are positioned around the RIS and the center (15 m, 10 m, 0 m), respectively.

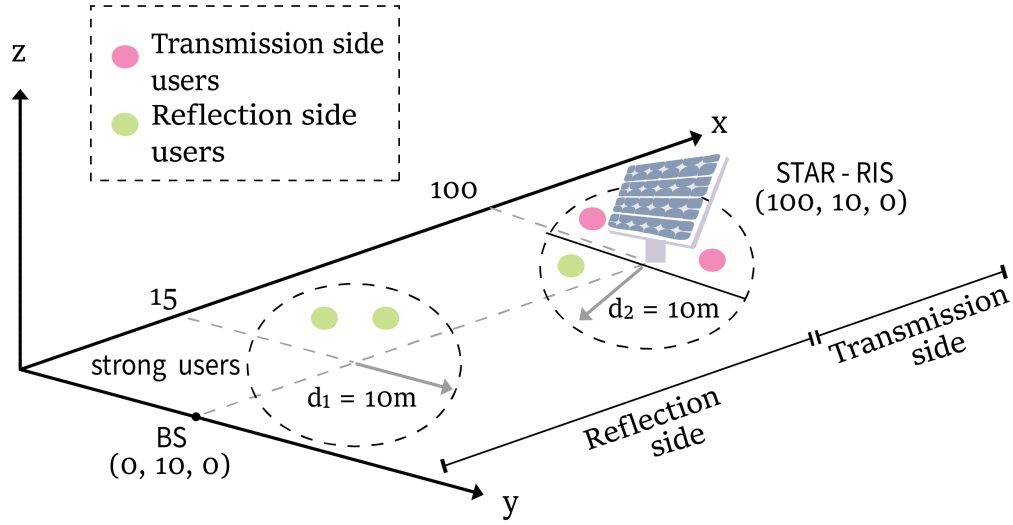


Figure 3.2: Simulation setup

BS-user and strong user-weak user links are modeled as Rayleigh fading, while the RIS-assisted links are modeled as Rician fading which are given by:

- $\mathbf{h}_k = \sqrt{PL(d_{BU})}\mathbf{h}_k^{NLOS}, \forall k \in \mathcal{K},$
- $h_{s,w} = \sqrt{PL(d_{SW})}h_{s,w}^{NLOS}, \forall s \in \mathcal{S}, \forall w \in \mathcal{W},$
- $\mathbf{f}_k = \sqrt{\frac{PL(d_{RU})}{k_{RU}+1}} (\sqrt{k_{RU}}\mathbf{f}_k^{LOS} + \mathbf{f}_k^{NLOS}), \forall k \in \mathcal{K},$
- $\mathbf{G} = \sqrt{\frac{PL(d_{BR})}{k_{BR}+1}} (\sqrt{k_{BR}}\mathbf{G}^{LOS} + \mathbf{G}^{NLOS}),$

where $PL(d_{BU}), PL(d_{RU}), PL(d_{SW})$ and $PL(d_{BR})$ are the distance dependent path loss modeled as $PL(d) = \rho_o d^{-\alpha}$. Here, ρ_o represents the path loss at the reference distance of 1 m, d signifies the distance, and α denotes the path loss exponent for the communication link. k_{RU} and k_{BR} stand for the Rician factors, \mathbf{f}_k^{LOS} and \mathbf{G}^{LOS} are the deterministic line-of-sight (LoS) components, while $\mathbf{h}_k^{NLOS}, \mathbf{h}_{s,w}^{NLOS}, \mathbf{f}_k^{NLOS}$ and \mathbf{G}^{NLOS} represent the random non-LoS (NLoS) components modeled using a Rayleigh distribution with zero mean and unitary variance. Key simulation parameters are outlined in Table 3.1; these parameters remain consistent across all simulations unless explicitly mentioned otherwise.

Parameter	Value	Parameter	Value
α_{SW}, α_{BW}	3.5	ρ_o	-30 dB
α_{RW}, α_{BR}	2.2	$R_{min,k}$	1 bps/Hz
α_{RS}, α_{BS}	3	P_{BS}	40 dBm
k_{RU}, k_{BR}	3 dB	P_{RIS}	30 dBm
σ_s, σ_w	-110 dBm	P_s	15 dBm
σ_{RIS}	-120 dBm	β_{max}	10
K	4	σ_{SI}	-120 dB
N	16	S	2

Table 3.1: Simulation Parameters

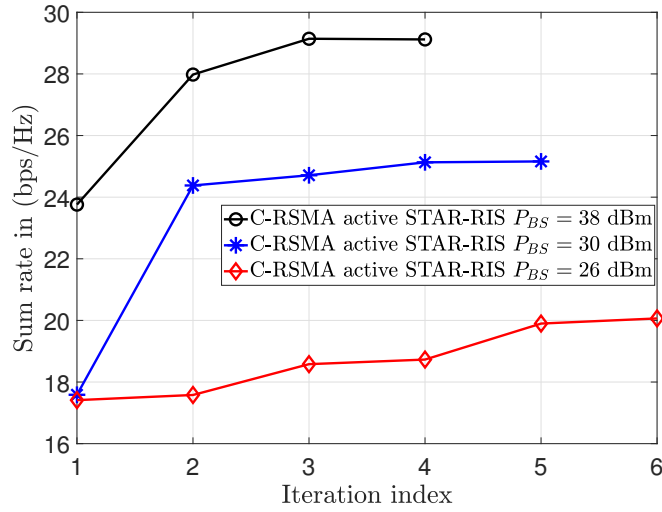
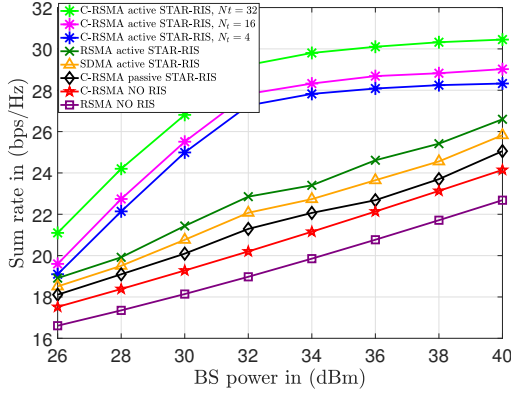


Figure 3.3: Convergence of Algorithm 1

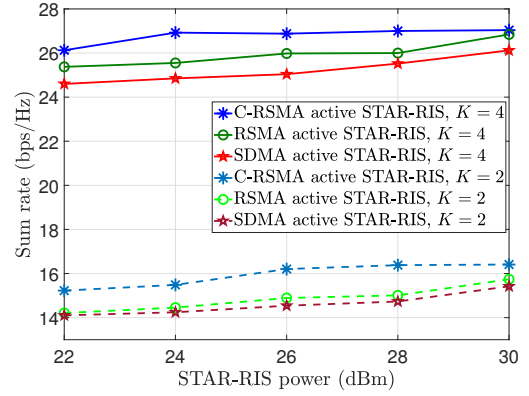
Performance Analysis

In Fig. 3.3, we illustrate the convergence behavior of the proposed active STAR RIS-assisted FD C-RSMA algorithm with the iteration number across different power budgets at the BS. We can see that the algorithm converges within few iterations in all cases.

Fig. 3.4a illustrates the relationship between the system sum rate and the transmit power of the BS. It can be seen that our proposed scheme consistently outperforms baseline alternatives. This superior performance is attributed to the dual flexibility arising from the increased degrees of freedom (DoFs) facilitated by the active STAR-RIS and collaboration with strong users. Within the power range of 26 to 36 dBm, the system's sum rate experiences exponential growth, showcasing the efficiency of our proposed approach in achieving higher rates with limited power compared to



(a) Sum Rate vs. BS power



(b) Sum Rate vs. RIS power

Figure 3.4: Active STAR RIS-assisted FD C-RSMA performance against baselines

other schemes. The significance of an active STAR-RIS is highlighted when compared with schemes utilizing passive STAR-RIS. As depicted in Fig. 3.4a, C-RSMA with passive STAR-RIS consistently yields lower performance rankings compared to RSMA with active STAR-RIS. This observation underscores that cooperation alone is insufficient to surpass the performance gains achieved with an active STAR-RIS, even at low power levels. The synergistic effect of both cooperation and the influence of the active STAR-RIS enables our system to achieve nearly the maximum sum rate with minimal BS power, which is highlighted by an astonishing gain of 20.3% at 32 dBm compared with the second-ranked baseline. In the power range of 36 to 40 dBm, the system approaches saturation. This behavior is attributed to the power constraint defined in equation (7c), wherein the system restricts the increase in allocated power to the BS beamformers and relaying users to prevent exceeding the available power at the active RIS. Additionally, it is observed that when the number of transmit antennas at the BS is increased, the achieved sum rate is enhanced due to the added degrees of freedom in the system.

In Fig. 3.4b, we analyze the impact of the power available at the active STAR-RIS on the system's performance. Our initial observation is that the performance rankings of the baselines remain consistent with those in Fig. 3.4a, with our proposed scheme continuing to be the best performer. Furthermore, our proposed model demonstrates exceptional performance even with resource constraints. Remarkably, a modest active STAR-RIS power of 24 dBm was sufficient to approach the

peak achieved sum rate, registering a gain of approximately 6% compared to RSMA active STAR-RIS. The observed plateau occurs because, beyond a certain point, the additional power from the STAR-RIS no longer contributes to performance improvements. Instead, the noise introduced by the active STAR-RIS starts to degrade the system's performance. Thus, the sum rate achieved by the system can no longer be improved. Examining the other two baselines, RSMA outperforms SDMA. As the STAR-RIS power increases sufficiently, the performance of RSMA approaches that of our proposed scheme. Therefore, we can conclude that within our proposed framework, only low levels of STAR-RIS power are necessary to achieve a remarkable gain over the other baselines. These findings emphasize the critical roles played by both user cooperation and the active STAR-RIS in enhancing the system sum rate and prove the advantage of the proposed system model compared to other related works. Additionally, we observe that across varying numbers of users, all the compared schemes exhibit similar behavior.

In conclusion, the findings underscore the remarkable performance of the proposed scheme, which consistently outperforms baseline alternatives across various scenarios. This superiority is attributed to the scheme's dual flexibility, enabled by the active STAR-RIS and collaboration with strong users.

3.5 A Deep Reinforcement Learning-Driven Optimization for Active STAR-RIS empowered C-RSMA

3.5.1 Problem Formulation

In this section, we remind the reader with the problem to be optimized, while writing it in a more suitable form for the remaining of this chapter. We aim to jointly design the BS transmit beamforming \mathbf{p} , active STAR-RIS reflection and transmission beamforming matrices, i.e., Θ_r and Θ_t , common stream split $\mathbf{c} = [C_1, \dots, C_K]$ and the transmit relaying powers at the strong users

$\mathbf{p}_r = [p_{r,1}, \dots, p_{r,S}]$ to maximize the network sum rate, while satisfying the minimum rate constraints, active STAR-RIS hardware constraints, the given power budget P_{RIS} at the active STAR-RIS, P_{BS} at the BS and P_s at each strong user s , which can be formulated as:

$$\max_{\substack{\mathbf{p}, \mathbf{p}_r, \mathbf{c}, \\ \Theta_r, \Theta_t}} \sum_{k=1}^K R_k \quad (32a)$$

$$\text{s.t. } v_i \leq 0 \quad \forall i \in \{1, \dots, 9\}, \quad (32b)$$

where the expressions for the constraints v_i are defined as:

$$v_1 = \|\mathbf{p}_c\|^2 + \sum_{j=1}^K \|\mathbf{p}_j\|^2 - P_{BS}, \quad (33)$$

$$\begin{aligned} v_2 = & \sum_{j=1}^K \|\Theta_r \mathbf{G} \mathbf{p}_j\|^2 + \|\Theta_r \mathbf{G} \mathbf{p}_c\|^2 + \sum_{j=1}^K \|\Theta_t \mathbf{G} \mathbf{p}_j\|^2 + \|\Theta_t \mathbf{G} \mathbf{p}_c\|^2 \\ & + \sum_{s=1}^S \|\Theta_r \mathbf{f}_s^H\|^2 p_{r,s} + \sum_{s=1}^S \|\Theta_t \mathbf{f}_s^H\|^2 p_{r,s} + \sigma_{RIS}^2 (\|\Theta_r\|_F^2 + \|\Theta_t\|_F^2) - P_{RIS}, \end{aligned} \quad (34)$$

$$v_3 = \max(0, p_{r,s} - P_s), \quad \forall s \in \mathcal{S}, \quad (35)$$

$$v_4 = R_{min,k} - R_k, \quad \forall k \in \mathcal{K}, \quad (36)$$

$$v_5 = \sum_{i=1}^K C_i - R_c, \quad (37)$$

$$v_6 = -C_i, \quad \forall i \in \mathcal{K}, \quad (38)$$

$$v_7 = \max(0, -\beta_{t_n}) + \max(0, -\beta_{r_n}), \quad \forall n \in \{1, \dots, N\}, \quad (39)$$

$$v_8 = (\beta_{t_n} + \beta_{r_n}) - \beta_{max}, \quad \forall n \in \{1, \dots, N\}, \quad (40)$$

$$\begin{aligned} v_9 = & \max(0, \theta_{r_i} - \pi) + \max(0, -\pi - \theta_{r_i}) + \max(0, \theta_{t_i} - \pi) \\ & + \max(0, -\pi - \theta_{t_i}), \quad \forall i \in \{1, \dots, N\}. \end{aligned} \quad (41)$$

Constraints (33), (34), and (35) ensure adherence to the designated power allocations at the BS, the active STAR-RIS, and each individual strong user, respectively. Condition (36) mandates the fulfillment of minimum quality of service requirements for all users within the system, while (37) establishes R_c as the minimum among $R_{c,1}, \dots, R_{c,K}$, as elaborated in the preceding section. Moreover,

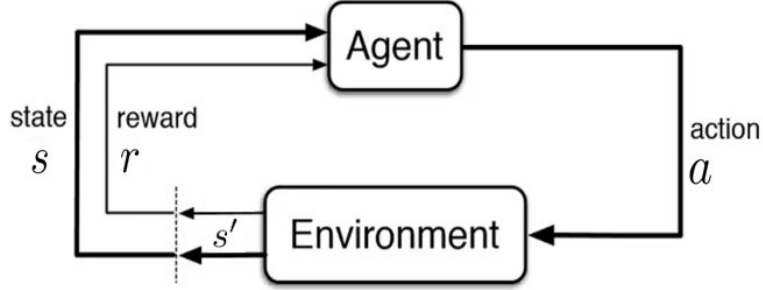


Figure 3.5: MDP illustration

constraints (39)-(41) encapsulate the hardware limitations of the active STAR-RIS.

Traditional optimization techniques typically address this by convexifying the problem through approximations and solving it iteratively until convergence, such as the method employed in section 3.4.3. However, these algorithms are computationally expensive and can require several iterations to converge which can be prohibitive for real-time applications in wireless communication systems, particularly those with a large number of users. To overcome this challenge, we propose a time-efficient DRL-based approach to predict the optimal configuration for the system.

3.5.2 MDP Description

In reinforcement learning, Markov Decision Processes (MDPs) model sequential decision-making in stochastic environments. An MDP, represented as $(\mathbb{S}, \mathbb{A}, \mathbb{P}, \mathbb{R})$, includes states \mathbb{S} , actions \mathbb{A} , transition probabilities \mathbb{P} , and reward functions \mathbb{R} . Here, $s \in \mathbb{S}$ is the current state, $a \in \mathbb{A}$ is the action, $s' \in \mathbb{S}$ is the next state, and $r \in \mathbb{R}$ is the reward. The transition function $P(s'|s, a)$ specifies the probability of moving to state s' from state s after action a . The reward function $R(s, a, s')$ defines the reward for transitioning from state s to state s' after action a . The described MDP process is illustrated in Fig .3.5.

For our communication system optimization, states encapsulate system parameters like resource allocations, and actions involve decisions such as adjusting BS beamformers or configuring the STAR-RIS. The MDP components are defined as follows:

- State: $s = (\mathbf{p}, \mathbf{p}_r, \mathbf{c}, \Theta_r, \Theta_t, \mathbf{v})$

- Action: $a = (\Delta \mathbf{p}, \Delta \mathbf{p}_r, \Delta \mathbf{c}, \Delta \Theta_r, \Delta \Theta_t)$.

Here, $\mathbf{v} = [v_1, \dots, v_9]$ is the constraint violation vector. The large state dimension can hinder the critic's learning, especially regarding beamforming vector coefficients. To address this, we feed the critic with a reduced state: $\tilde{\mathbf{s}} = (\|\mathbf{p}\|, \mathbf{p}_r, \mathbf{c}, \Theta_r, \Theta_t, \mathbf{v})$, where $\|\mathbf{p}\| = [\|\mathbf{p}_c\|, \|\mathbf{p}_1\|, \dots, \|\mathbf{p}_K\|]$. Tracking the norms of the beamforming vectors instead of the full vectors helps the RL agent capture essential information while keeping the state dimension manageable.

At the start of each MDP, a new environment is generated for the agent, featuring new randomly determined channel conditions $(\tilde{\mathbf{h}}, \tilde{\mathbf{h}}_{co}, \mathbf{h}_{SI}, \mathbf{f}, \mathbf{G})$ that simulate the conditions of our downlink communication system, where $\tilde{\mathbf{h}} = [\tilde{\mathbf{h}}_1, \dots, \tilde{\mathbf{h}}_K]$, $\mathbf{f} = [\mathbf{f}_1, \dots, \mathbf{f}_K]$, $\mathbf{h}_{SI} = [h_{SI,1}, \dots, h_{SI,S}]$ and $\mathbf{h}_{co} = [h_{s,w}, \forall s \in \mathcal{S}, \forall w \in \mathcal{W}]$. All the mentioned channels are defined as discussed in section 3.6.1. At each time step, the agent observes the channels dictated by the environment, the current system configuration $(\mathbf{p}, \mathbf{p}_r, \mathbf{c}, \Theta_r, \Theta_t)_i$ contained in state s_i and the constraint violation coefficients \mathbf{v} , then takes an action a_i consisting of adjustments to the current observed values $a_i = (\Delta \mathbf{p}, \Delta \mathbf{p}_r, \Delta \mathbf{c}, \Delta \Theta_r, \Delta \Theta_t)_i$, leading to the next state $s_{i+1} = (\mathbf{p}, \mathbf{p}_r, \mathbf{c}, \Theta_r, \Theta_t)_{i+1} = (\mathbf{p}_i + \Delta \mathbf{p}_i, \mathbf{p}_{r_i} + \Delta \mathbf{p}_{r_i}, \mathbf{c}_i + \Delta \mathbf{c}_i, \Theta_{r_i} + \Delta \Theta_{r_i}, \Theta_{t_i} + \Delta \Theta_{t_i})$.

It is important to highlight that the channels remain constant throughout internal transitions within the same trajectory of the agent, as they are not modifiable parameters under the agent's control. The agent keeps transitioning between the states while adjusting the optimization variables until converging to the terminal state containing the optimal configuration for the system that maximizes the sum rate and satisfies the constraints.

3.5.3 Reward Design

Among the constraints outlined in Section II.E, v_3, v_6, v_7 and v_9 are inherently reflected and satisfied within the state space definition. To address the remaining five constraints stipulated in our optimization problem while maximizing the sum rate, the reward is defined as follows:

$$r = \sum_{k=1}^K R_k + \sum_{j=1}^5 r_j \quad (42)$$

The first component in (42) represents the sum rate achieved by the current system configuration, encouraging the model to maximize this value, While the second term guarantees adherence to the system’s constraints. In this context, r_j denotes the reward attributed to constraint j , which is defined as:

$$r_j = \begin{cases} +10 & \text{if constraint } j \text{ is satisfied} \\ -v_j & \text{if constraint } j \text{ is violated} \end{cases} \quad (43)$$

The design of the reward function plays a crucial role in shaping the learning dynamics of the reinforcement learning agent. In our formulation, we emphasize a balanced approach that incentivizes desirable behavior while appropriately penalizing constraint violations. To achieve this balance, we assign moderate rewards and penalties, ensuring the agent receives meaningful feedback without extreme influences that could mislead or overwhelm it. Specifically, we set rewards to +10 for satisfying constraints and penalties to $-v_j$ for violations, providing a clear signal that encourages adherence to specified constraints while maximizing the sum rate. Opting for a distance-based penalty v_j over a constant penalty helps the model better understand optimization directions and how far it is from satisfying each constraint, while facilitating smoother training by mitigating abrupt changes in rewards.

3.5.4 Model Architecture

Given the complexity of optimizing multiple variables across several distinct constraints concurrently, a single DRL model might lead to a cumbersome state representation and hinder effective learning. To address this challenge and streamline training, we have adopted a strategy using two separate actor-critic models, each focused on optimizing a sub-problem targeting different subsets of variables.

Actor-Critic Model

The actor-critic architecture stands out among deep reinforcement learning approaches by combining both benefits of policy-based methods (direct policy optimization) and value-based methods (efficient value estimations) within a single framework [35]. This model is particularly suited for

complex environments with continuous action spaces, which is the case of this work.

In the actor-critic framework, the actor is responsible for learning a policy that maps states directly to actions. This policy outputs continuous-valued actions, allowing for precise control in continuous action spaces. Simultaneously, the critic evaluates the actions chosen by the actor by estimating the expected cumulative reward that would be obtained from following the actor’s policy. The critic learns to assess the quality of actions taken in different states, providing feedback to the actor about which actions are more likely to lead to higher rewards. This feedback is crucial for guiding the actor’s learning process towards actions that maximize long-term rewards.

During training, the actor and critic networks interact iteratively: the actor selects actions based on its current policy, these actions are executed in the environment, resulting in new states and rewards, and the critic evaluates these actions to provide feedback to the actor. Both the actor and critic networks are updated based on their respective loss functions which are given by:

$$L_{actor} = -\mathbb{E}_{s \sim D} [Q_{\theta}(s, \pi_{\phi}(s))], \quad (44)$$

$$L_{critic} = \mathbb{E}_{(s,a,r,s') \sim D} [\delta^2], \quad (45)$$

$$\delta = r + \gamma Q_{\theta'}(s', \pi_{\phi'}(s')) - Q_{\theta}(s, a), \quad (46)$$

where,

- L_{critic} : Loss function for the critic network.
- L_{actor} : Loss function for the actor network.
- D : Replay buffer from which samples are drawn.
- δ : Temporal difference (TD) error.
- γ : Discount factor for future rewards.
- $Q_{\theta}(s, a)$: Critic network parameterized by θ , estimating the value of action a in state s .
- $\pi_{\phi}(s)$: Actor network parameterized by ϕ , providing the action to be taken in state s .
- θ' : Parameters of the target critic network.

- ϕ' : Parameters of the target actor network.

Target networks θ' and ϕ' are periodically updated copies of the critic and actor networks used to stabilize training by providing consistent targets for learning. The parameters of the target networks are updated using a soft update technique, which ensures smoother transitions:

$$\theta' \leftarrow \tau\theta + (1 - \tau)\theta' \quad (47)$$

$$\phi' \leftarrow \tau\phi + (1 - \tau)\phi' \quad (48)$$

where $\tau \ll 1$ is a small parameter that controls the update rate.

Actor-Critic Models for Sub-Problem Optimization

As we previously mentioned, we adopted a strategy of training two separate actor-critic models, each dedicated to optimizing distinct sub-problems consisting of their respective sets of variables and corresponding constraints. Actor-Critic-1 focuses on optimizing variables $(\mathbf{p}, \mathbf{p}_r, \mathbf{c})$ while adhering to constraints (v_1, v_2, v_4, v_5) . On the other hand, Actor-Critic-2 is designed to optimize variables $(\boldsymbol{\theta}_r, \boldsymbol{\theta}_t, \boldsymbol{\beta}_r, \boldsymbol{\beta}_t)$ while satisfying constraints (v_4, v_5, v_7) .

The joint training of these models presents a significant challenge, as they must collectively optimize the system's sum rate while focusing on their respective variables and constraints. To address this complexity, we implemented a 3-phase strategy inspired by curriculum learning—a method that facilitates gradual learning of increasingly complex tasks [36]. In phase 1, Actor-Critic-1 focuses on optimizing the first sub-problem without considering the active STAR-RIS assistance. This involves temporarily excluding terms related to RIS variables from both constraints and rate expressions for this phase only. Training occurs across multiple environments within each episode to ensure robust generalization across varying channel characteristics. In phase 2, Actor-Critic-2 is trained to address the second sub-problem, guided by predictions from Actor-Critic-1. Here, the fixed values predicted by Actor-Critic-1 for variables $(\mathbf{p}, \mathbf{p}_r, \mathbf{c})$ are incorporated into the environment, while adjustments are made to $(\boldsymbol{\theta}_r, \boldsymbol{\theta}_t, \boldsymbol{\beta}_r, \boldsymbol{\beta}_t)$ to meet constraints (v_4, v_5, v_7) . A comprehensive dataset of predictions from Actor-Critic-1 ensures exposure to various scenarios encountered during training.

The third phase involves iterative joint training of the models. Each episode begins with the first model initializing variables $(\theta_r, \theta_t, \beta_r, \beta_t)$ based on predictions from the second model in previous iterations, aiming to optimize the first sub-problem while fixing the RIS variables. The predictions for $(\mathbf{p}, \mathbf{p}_r, \mathbf{c})$ are then fed to the second model, which addresses the second sub-problem. This iterative process continues until either the episode meets constraints or reaches the maximum steps. In our implementation, we normalized all variables in both the state and action vectors to facilitate training. Additionally, training begins with a different environment including new channels at each episode's start. It is noteworthy that limiting the maximum number of steps per episode not only accelerates training but also prevents the model from becoming entrenched in incorrect paths and helps exposing it to a diverse range of scenarios without wasting computational resources.

3.5.5 Prioritized Experience Replay

To enhance the efficiency of training, each of the two models employs a Prioritized Experience Replay (PER) buffer, as introduced by Schaul et al. [37]. This technique prioritizes experiences based on their temporal-difference (TD) errors, allowing the model to focus on more informative experiences, thus improving convergence and overall performance. Transitions with higher TD errors are sampled more frequently using a probability distribution proportional to their errors, $P(i) = \frac{p_i^\alpha}{\sum_k p_k^\alpha}$, where p_i is the priority of transition i , with the exponent α determining how much prioritization is used. Importance-sampling weights, $w_i = \left(\frac{1}{N} \cdot \frac{1}{P(i)}\right)^\beta$, correct the bias introduced by prioritized sampling using the exponent β , aiding in stabilizing the reinforcement learning model.

3.5.6 Simulation Results and Discussion

This section evaluates the performance of the proposed DRL model through numerical simulations and compares it with the SCA-based alternating optimization algorithm from the previous chapter.

Parameter	Value	Parameter	Value
BATCH SIZE	1024	γ	0.99
BUFFER SIZE	10^5	τ	10^{-3}
α	0.6	learning rate _{actor}	10^{-4}
β	0.4	learning rate _{critic}	$2 \cdot 10^{-4}$
ϵ	10^{-5}	MAX STEPS PER EPISODE	10

Table 3.2: Training Hyperparameters

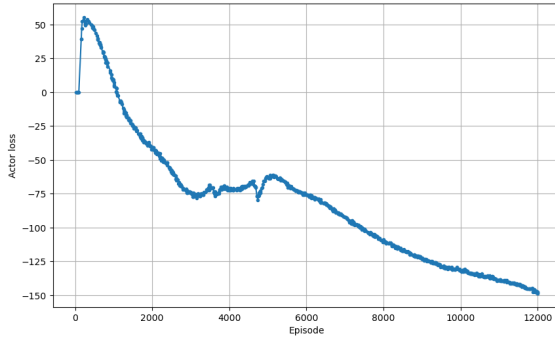


Figure 3.6: Actor loss for Actor-Critic-1

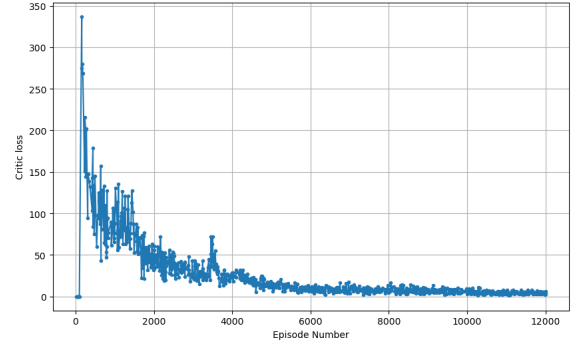


Figure 3.7: Critic loss for Actor-Critic-1

Training Hyperparameters

In this section, we detail the hyperparameters and architecture of our actor-critic model. The Actor network comprises three fully connected layers: a 512-neuron input layer with batch normalization (BN1) and ReLU activation, a 256-neuron layer with batch normalization (BN2) and ReLU activation, and a final layer with tanh activation for action space mapping. The Critic network also features three fully connected layers: a 512-neuron input layer with batch normalization (BN1) and ReLU activation, followed by concatenation with the action input from the actor network and a 256-neuron layer with ReLU activation, and a final layer producing the Q-value. Other key hyperparameters are outlined in Table. 3.2.

Training Results

In this section, we examine the training results of our models over 12,000 episodes. For the first model, Fig. 3.6 illustrates a steady decline in actor loss, signifying stable learning dynamics and improved action selection by the actor, which is positively reinforced by the critic’s feedback. This stability is further supported by the critic loss curve shown in Fig. 3.7, which also decreases

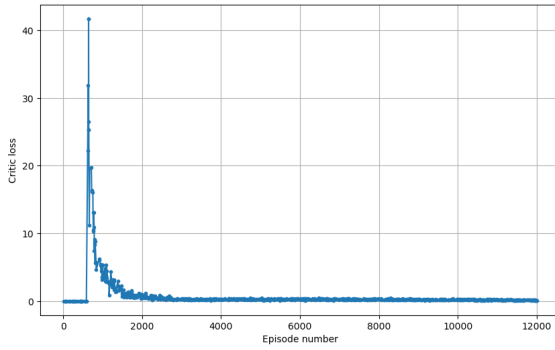


Figure 3.8: Critic loss for Actor-Critic-2

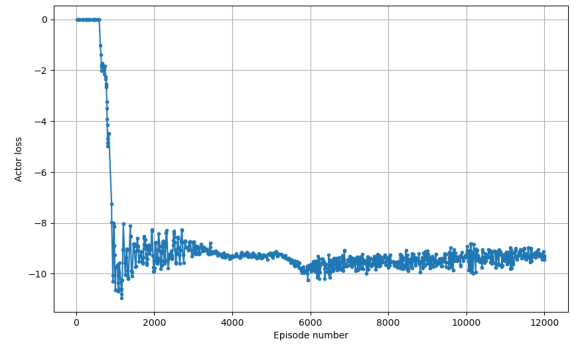


Figure 3.9: Actor loss for Actor-Critic-2

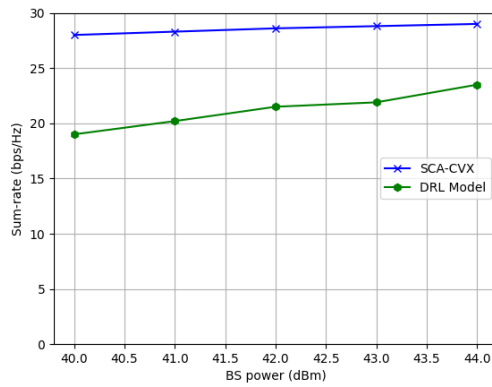


Figure 3.10: DRL model performance against SCA baseline method

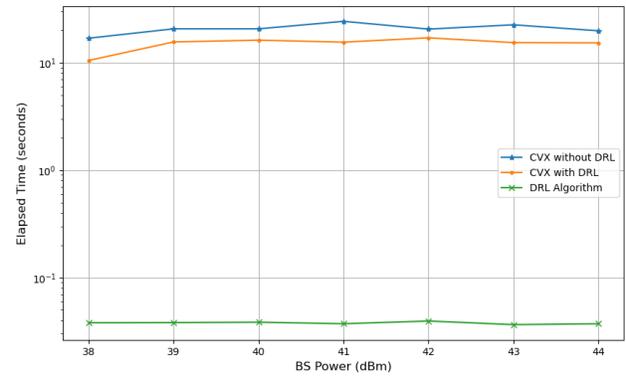


Figure 3.11: Comparison of prediction time of the DRL model against the SCA baseline

progressively, indicating the critic’s growing confidence in evaluating the quality of the actor’s decisions. Figure 3.9 presents the training outcomes for the second model’s actor network. Although the actor loss exhibits some fluctuations, it gradually stabilizes towards the later stages of training. The critic’s performance shown in Fig. 3.8 is desirable, with convergence achieved in the early episodes.

Testing Results

In this section, we evaluate the performance of the proposed DRL model against the results obtained from SCA-based optimization baseline. As depicted in Figure 3.10, the current DRL model exhibits less robustness compared to conventional optimization techniques, indicating a need for further refinement. This discrepancy is particularly evident in scenarios with a low power budget, where the stringent budgetary constraints challenge the DRL model’s ability to find feasible solutions within the search space. In contrast, the SCA-based algorithm successfully identifies solutions

even under these constraints. Notwithstanding its current limitations, the DRL agent demonstrates promising behavior by enhancing the achieved sum rate as the resources at the BS increase. Specifically, at a BS power level of $P_{BS} = 44$ dBm, the DRL agent achieves its peak performance, delivering a sum rate of 24.3 bps/Hz, which approximates 84% of the optimal 29 bps/Hz attained by the convex optimization approach.

Additionally, the DRL-based solution demonstrates significant gains in computational efficiency, effectively compensating for the loss in sum rate. As shown in Figure 3.11, while the SCA-based algorithm takes an average of 20 seconds to compute a solution, the DRL-based model accomplishes the same task in just 0.038 seconds—a remarkable 99.81% reduction in execution time. The trade-off between optimality and speed becomes even more valuable in large-scale or rapidly changing network environments. Although the SCA-based solution maintains superior optimality, we further improved its time efficiency by initializing it with predictions from the DRL model instead of using a random feasible point. This approach, highlighted in orange, led to a 25% reduction in execution time. These findings underscore the DRL-based solution’s significant advantage in time efficiency, a critical factor for modern wireless communication systems.

3.6 Summary and Conclusions

This chapter explored using an active STAR-RIS to enhance a C-RSMA downlink system, optimizing various parameters to maximize the communication sum rate while satisfying constraints. A comprehensive analysis underscored the remarkable performance of the proposed scheme, which consistently outperforms baseline alternatives across various scenarios. This superiority is attributed to the scheme’s dual flexibility, enabled by the active STAR-RIS and collaboration with strong users.

Due to the high time complexity required by traditional convex approximation methods, they remain impractical for real-time applications despite their optimization capabilities. To address this challenge, we proposed a more time-efficient DRL framework using an actor-critic model. Simulations show that while the DRL model is less robust than conventional techniques under strict power constraints, it performs well with increased BS resources, achieving a significant portion of the

optimal sum rate. The DRL solution also demonstrated substantial computational efficiency, significantly reducing execution time compared to the SCA algorithm. Initializing the SCA algorithm with DRL predictions reduced its execution time, suggesting potential for hybrid approaches.

Future work will focus on improving the model's performance to achieve results closer to the optimal by exploring various DRL architectures. Additionally, investigating hybrid approaches that integrate DRL with classical optimization techniques could provide further improvements in both efficiency and robustness.

Chapter 4

RIS for Enhancing Resilience Against MA-Enabled Jamming in Downlink Wireless Networks

4.1 Introduction

The emergence of MA technology has marked a significant advancement in the field of wireless communication research, paving the way for enhanced connectivity, improved signal quality, and adaptability across diverse environments. By allowing antennas to adjust positions dynamically within a finite area at transceivers, this technology enables more favorable channel conditions, optimizing performance across applications like mobile telecommunications and remote sensing.

Yet, as with every groundbreaking technology, the potential for exploitation by adversaries looms large. While MAs can enhance connectivity, they may also be repurposed for malicious activities such as jamming. In this chapter, we rigorously analyze the implications of an MA-empowered jamming system—featuring M movable antennas—within a downlink multi-user framework where a BS equipped with N antennas transmits data to K single-antenna users.

Furthermore, we investigate the promise of RIS as a potent countermeasure against MA-based

jamming in downlink wireless networks. RIS technology has gained attention for its ability to manipulate the wireless propagation environment, offering a promising approach to enhancing security and resilience against adversarial interference. By intelligently controlling phase shifts and reflections, RIS can mitigate jamming effects, particularly when the jammer benefits from mobility and adaptability.

Our comprehensive study evaluates the efficacy of RIS in safeguarding network integrity by quantifying its impact on mitigating performance degradation induced by MA-enabled jammers. We examine key performance metrics, including system sum rate and outage probability, under various configurations. Ultimately, this investigation aims to demonstrate the viability of RIS-assisted security mechanisms and provide valuable insights into their potential to counteract the disruptive influence of MA-based jamming in next-generation wireless networks.

4.2 State of The Art

The advent of MA technology represents an innovative shift in wireless communication systems, offering dynamic positioning capabilities to manage and improve signal propagation and reception adaptively. Unlike traditional FPAs, MAs can adjust their location within a designated region, exploiting spatial degrees of freedom (DoF) allowing them to optimize connectivity based on environmental and system-specific parameters. These systems harness spatial diversity more effectively than FPAs, particularly in scenarios with low mobility or limited diversity options, such as Industrial IoT, smart home applications and satellite communications [24].

While the implementation of MAs may vary, they are generally defined as antennas connected to the radio frequency (RF) chain through a flexible cable, allowing mobility facilitated by a positioning mechanism or driver [25]. An early approach to MA design involved a reconfigurable linear array in which dipole antennas, mounted on stepper motors, could move along semicircular paths [38]. Another initial design allowed for the rotation of a uniform linear array (ULA) while maintaining fixed antenna spacing, aiming to achieve line-of-sight (LoS) transmission capacity [39]. The existing designs in the literature can be broadly classified into two categories: mechanical MAs and fluid antennas, also known as fluid antenna systems (FAS). Mechanical MAs utilize actuators, such

as stepper motors, to enable antenna movement in three-dimensional space [25]. In contrast, fluid antennas are constructed using liquid metals or ionized solutions [40]. These antennas are designed to move between discrete, predefined positions, referred to as ports, along a one-dimensional line.

The literature on MAs primarily emphasizes their potential for enhancing link reliability, reducing interference, and supporting flexible deployment in challenging propagation environments. In [26], the authors compare the maximum channel gain of a single receive MA to that of its FPA counterpart, demonstrating that the MA system achieves significant performance improvements over conventional FPA systems, both with and without antenna selection (AS). The study in [25] showed that the total transmit power of multiple access systems can be significantly decreased when using MAs compared to conventional FPA systems employing AS. MAs can also significantly enhance physical layer security (PLS). In [41], the authors demonstrate that an MA array considerably improves the secrecy rate compared to a conventional FPA array when transmitting confidential information in the presence of multiple eavesdroppers. Furthermore, [42] explores scenarios where perfect CSI about the eavesdroppers is unavailable, focusing on the transmission of confidential data from an MA-enabled array to multiple single-antenna receivers. The results reveal that MA-enabled PLS systems outperform FPAs in maximizing secrecy rates.

While previous research highlights the significant advantages of MAs, this technology is also susceptible to misuse, as has been the case with many innovations throughout history. Hackers and malicious actors may attempt to exploit MAs for their harmful purposes. Therefore, it is crucial to examine the potential implications of MAs when used maliciously, a topic that is yet to be explored in the literature. One significant threat is jamming, where a malicious user aims to intensify interference against legitimate users to disrupt or stop their communication. In this chapter, we investigate how MAs can enhance jamming efforts by a malicious user targeting legitimate users.

In light of these vulnerabilities, we next shift our focus to a potential countermeasure using a reconfigurable intelligent surface. RIS technology offers a dynamic means of reengineering the wireless propagation environment by precisely controlling phase shifts and reflections. In our study, we evaluate the efficacy of RIS-assisted defenses in downlink wireless networks confronted with MA-based jamming attacks. Specifically, we simulate a scenario where an RIS is deployed to counteract the disruptive influence of a malicious user leveraging MAs, assessing key performance indicators

such as system sum rate and outage probability. This rigorous analysis aims to demonstrate that RIS can substantially mitigate the deleterious effects of MA-enabled jamming, thereby reinforcing the resilience and security of next-generation wireless networks.

4.3 Contributions

Our main contributions are as follows:

- We analyze the impact of an MA-assisted jammer in a downlink MISO system, where a BS serves K users through SDMA.
- We formulate an optimization problem in which the jammer decides both the antenna locations and beamforming vectors to minimize the overall system sum rate. Due to its non-convexity, the problem is divided into two sub-problems, which are alternately solved until convergence.
- We perform numerical examples under different scenarios, comparing the system sum rate and outage probability achieved with MAs versus FPAs. Results indicate that MAs reduce the system sum rate 30% more than FPAs. Moreover, MAs raise the outage probability by 25% compared to FPAs, resulting in a 20% increase in the number of users affected by outages.
- We rigorously evaluate the performance of RIS as a potential countermeasure against MA-based jamming attacks. Our investigation encompasses extensive simulation studies that assess key performance metrics—including system sum rate and outage probability—under diverse adversarial conditions.
- We examine two key scenarios: one where the jammer has full access to the RIS configuration and another where it does not, thereby establishing the upper and lower bounds of its impact. Our findings highlight that protecting the RIS channel state information is essential, as its compromise not only negates the benefits of RIS but can also turn it into a liability for the system.

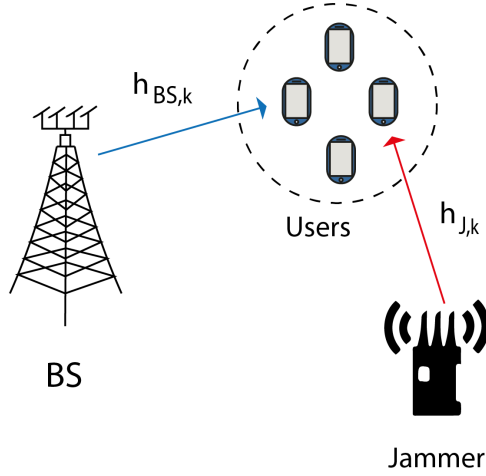


Figure 4.1: Jamming system model

4.4 Analyzing MA-Enabled Jamming in Downlink Wireless Networks

4.4.1 System Model

Network Model

As shown in Fig. 4.1, a BS equipped with a ULA of size N serves $K \leq N$ single-antenna users in downlink transmission at frequency $f = \frac{c}{\lambda_{BS}}$. Meanwhile, a jammer attempts to disrupt this communication using a device with M MAs, as illustrated in Fig. 4.2. Though structurally similar to a ULA, the jammer's antennas are mobile and can adjust positions according to the jammer's objectives. Each antenna has defined movement boundaries in the (X, Z) plane, ranging from $[x_{\min}, x_{\max}] \times [z_{\min}, z_{\max}]$. Along the y -axis, the antennas are unrestricted provided that the spacing between any two consecutive antennas remains at least $D = \lambda_J/2$ to avoid coupling effects [43], where λ_J denotes the jammer's transmitted signal wavelength. The direct channel from the BS to user k is represented by $\mathbf{h}_{BS,k} \in \mathbb{C}^{N \times 1}$, and the channel from the jammer to user k is denoted by $\mathbf{h}_{J,k} \in \mathbb{C}^{M \times 1} \forall k \in \mathcal{K} \triangleq \{1, \dots, K\}$. We denote $n_k \sim \mathcal{CN}(0, \sigma_k^2) \forall k \in \mathcal{K}$, as the AWGN.

Unaware of the jammer's presence, the BS optimizes its beamforming vectors based solely on the BS-user channels. Consequently, the BS's transmitted baseband signal can be expressed as $x = \sum_{k \in \mathcal{K}} \mathbf{w}_k s_k$, where $\mathbf{w}_k \in \mathbb{C}^{N \times 1}$ and s_k are the BS beamforming vector and the information

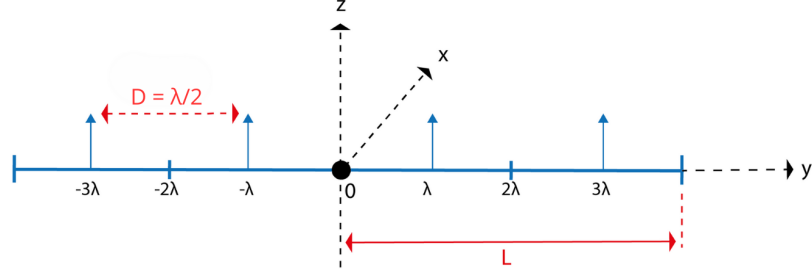


Figure 4.2: Movable antenna array

symbol for user k with zero mean and unit variance. The jammer aims to disrupt the communication between the BS and the users by transmitting a signal z through its antenna array, expressed as $z = \sum_{k \in \mathcal{K}} \mathbf{v}_k q_k$, where $\mathbf{v}_k \in \mathbb{C}^{M \times 1}$ is the jammer's beamforming vector, and q_k is the jamming signal symbol directed toward user k . We suppose that the jammer transmits over the same frequency used by the BS, i.e. $\lambda_{BS} = \lambda_J = \lambda$. Additionally, the jammer possesses CSI for all channels between itself and the users¹; however, the jammer lacks the CSI for the BS-user links. Given the above, the actual received signal at user k is expressed as²:

$$y_k = \mathbf{h}_{BS,k}^H \mathbf{w}_k s_k + \mathbf{h}_{J,k}^H \mathbf{v}_k q_k + n_k, \forall k \in \mathcal{K}. \quad (49)$$

The rate expression for each user depends on the multiple access technique employed by the BS. In our case, the BS employs SDMA, thus the achievable rate for each user k is given by:

$$R_k = \log_2 \left(1 + \frac{|\mathbf{h}_{BS,k}^H \mathbf{w}_k|^2}{\sum_{\substack{j \in \mathcal{K} \\ j \neq k}} |\mathbf{h}_{BS,k}^H \mathbf{w}_j|^2 + \sum_{j \in \mathcal{K}} |\mathbf{h}_{J,k}^H \mathbf{v}_j|^2 + \sigma_k^2} \right), \forall k \in \mathcal{K}, \quad (50)$$

where the term $\sum_{\substack{j \in \mathcal{K} \\ j \neq k}} |\mathbf{h}_{BS,k}^H \mathbf{w}_j|^2$ represents the interference from other users, $\sum_{j \in \mathcal{K}} |\mathbf{h}_{J,k}^H \mathbf{v}_j|^2$ is the interference from the jammer, and σ_k^2 is the noise power for user k .

¹We assume the jammer performs prior channel estimation, storing estimated channels for various user locations in a dictionary. During jamming, it selects channels based on users' current locations. The effect of imperfect field-response information (FRI) due to minor user location misalignment is minimal, allowing the algorithm to maintain robust performance [25].

²In this study, we assume that $M \geq K$, allowing the jammer to design a distinct beamforming vector for each user. If $K > M$, the jammer can still effectively target a group of M users, making the problem equivalent to the scenario discussed in this paper.

Channel Model

In this work, we consider narrow-band channels with slow fading. The BS-user links are modeled as Rayleigh fading, expressed as:

$$\mathbf{h}_{BS,k} = \sqrt{PL(d_{BS,k})} \mathbf{h}_{BS,k}^{NLOS}, \quad \forall k \in \mathcal{K}, \quad (51)$$

where $PL(d_{BS,k})$ is the distance dependent path loss modeled as $PL(d_{BS,k}) = \rho_o d^{-\alpha_{BS}}$. Here, ρ_o represents the path loss at the reference distance of 1 m, $d_{BS,k}$ signifies the BS-user distance, and α_{BS} denotes the path loss exponent for the communication link. $\mathbf{h}_{BS,k}^{NLOS}$ represents the random non-LoS component modeled using a distribution with zero mean and unitary variance.

The channel vector between the jammer and each user is determined by the propagation environment and the position of the MA at the jammer which is characterized by the field-response channel model [26]. In this model, because the movement regions for the jammer's antennas are significantly smaller than the signal propagation distance, we assume that the far-field condition holds. With this assumption, a plane-wave model can accurately represent the field response from the jammer's MA region to each user. Specifically, the angle of departure (AoD), angle of arrival (AoA), and the amplitude of the complex coefficient for each channel path between the BS and each user remain constant regardless of the MA's position within its movement region, while only the phase of each channel path changes with the MA's position.

Let L_k^t and L_k^r , for $1 \leq k \leq K$, denote the total number of transmit and receive channel paths from the jammer to user k , respectively. The elevation and azimuth AoDs for the j -th transmit path from the jammer to user k are denoted by $\theta_{k,j}^t$ and $\phi_{k,j}^t$ for $1 \leq j \leq L_k^t$. Similarly, the elevation and azimuth AoAs for the i -th receive path to user k are denoted by $\theta_{k,i}^r$ and $\phi_{k,i}^r$ for $1 \leq i \leq L_k^r$.

For simplicity, we define the virtual AoDs and AoAs as:

$$\begin{aligned} \vartheta_{k,j}^t &= \cos \theta_{k,j}^t \cos \phi_{k,j}^t, \quad \varphi_{k,j}^t = \cos \theta_{k,j}^t \sin \phi_{k,j}^t \\ \omega_{k,j}^t &= \sin \theta_{k,j}^t, \quad 1 \leq k \leq K, \quad 1 \leq j \leq L_k^t, \end{aligned} \quad (52)$$

$$\begin{aligned}
\vartheta_{k,i}^r &= \cos \theta_{k,i}^r \cos \phi_{k,i}^r, \quad \varphi_{k,i}^r = \cos \theta_{k,i}^r \sin \phi_{k,i}^r \\
\omega_{k,i}^r &= \sin \theta_{k,i}^r, \quad 1 \leq k \leq K, \quad 1 \leq j \leq L_k^r.
\end{aligned} \tag{53}$$

In light of the above, the transmit and receive field-response vectors (FRVs) for the channel from the jammer to user k are obtained as follows.

$$\mathbf{f}_k(\mathbf{p}_m) = \left[e^{j\frac{2\pi}{\lambda}\rho_{k,1}^t(\mathbf{p}_m)}, e^{j\frac{2\pi}{\lambda}\rho_{k,2}^t(\mathbf{p}_m)}, \dots, e^{j\frac{2\pi}{\lambda}\rho_{k,L_k^t}^t(\mathbf{p}_m)} \right]^T, \tag{54}$$

$$\mathbf{g}_k(\mathbf{u}_k) = \left[e^{j\frac{2\pi}{\lambda}\rho_{k,1}^r(\mathbf{u}_k)}, e^{j\frac{2\pi}{\lambda}\rho_{k,2}^r(\mathbf{u}_k)}, \dots, e^{j\frac{2\pi}{\lambda}\rho_{k,L_k^r}^r(\mathbf{u}_k)} \right]^T, \tag{55}$$

where, $\mathbf{u}_k \in \mathbb{R}^{3 \times 1}$ is the antenna position vector at user k and $\mathbf{p}_m \in \mathbb{R}^{3 \times 1}$ is the m -th antenna position vector at jammer. $\rho_{k,j}^r(\mathbf{u}_k) = X_k \vartheta_{k,j}^r + Y_k \varphi_{k,j}^r + Z_k \omega_{k,j}^r$ for $1 \leq j \leq L_k^r$ represents the difference in signal propagation distance for the j -th receive channel path between the user antenna position \mathbf{u}_k and the origin of the local coordinate system at user k . This indicates that the phase difference of the coefficient of the j -th receive channel path for user k between user position \mathbf{u}_k and O_k is given by $\frac{2\pi}{\lambda} \rho_{k,j}^r(\mathbf{u}_k)$. Similarly, the transmit FRV, $\mathbf{f}_k(\mathbf{p}_m)$, characterizes the phase differences in all L_k^t transmit paths to user k , where $\rho_{k,i}^t(\mathbf{p}_m) = x_m \vartheta_{k,i}^t + y_m \varphi_{k,i}^t + z_m \omega_{k,i}^t$ for $1 \leq i \leq L_k^t$ represents the difference of the signal propagation distance for the i -th transmit channel path between the m -th jammer-antenna position \mathbf{p}_m and the origin of the local coordinate system at jammer O_0 . The path-response matrix (PRM), $\Sigma_k \in \mathbb{C}^{L_k^t \times L_k^r}$, represents the response between all the transmit and receive channel paths from O_0 to O_k , $\forall k \in \mathcal{K}$. Specifically, the entry in the i -th row and j -th column of Σ_k is the response coefficient between the i -th transmit path and the j -th receive path for user k . Subsequently, the channel vector from the jammer to user k can be expressed as:

$$\mathbf{h}_{J,k}(\mathbf{P}) = \mathbf{F}_k^H(\mathbf{P}) \Sigma_k \mathbf{g}_k, \quad \forall k \in \mathcal{K}, \tag{56}$$

where $\mathbf{F}_k = \left[\mathbf{f}_k(\mathbf{p}_1), \mathbf{f}_k(\mathbf{p}_2), \dots, \mathbf{f}_k(\mathbf{p}_M) \right] \in \mathbb{C}^{L_k^t \times M}$ is the field-response matrix (FRM) at the jammer targeting user k , and $\mathbf{P} = [\mathbf{p}_1, \mathbf{p}_2, \dots, \mathbf{p}_M] \in \mathbb{R}^{3 \times M}$ is the antenna position matrix at the jammer. Since the positions of the antenna at each user are fixed, the field receive vectors $\mathbf{g}_k, \forall k \in \mathcal{K}$ are constant.

4.4.2 Problem Formulation

In this study, the aim of the jammer is to jointly optimize the MA location matrix \mathbf{P} , while designing the jamming beamforming matrix $\mathbf{V} = [\mathbf{v}_1, \mathbf{v}_2, \dots, \mathbf{v}_K] \in \mathbb{C}^{M \times K}$ to minimize the network sum rate, while adhering to available power budget P_J and the antenna array hardware constraints, which can be formulated as:

$$\mathcal{P} : \min_{\mathbf{V}, \mathbf{P}} \sum_{k \in \mathcal{K}} R_k \quad (57a)$$

$$\text{s.t.} \quad \sum_{k \in \mathcal{K}} \|\mathbf{v}_k\|^2 \leq P_J, \quad (57b)$$

$$-\lambda \leq x_m \leq \lambda \quad \forall m \in \{1, \dots, M\}, \quad (57c)$$

$$-\lambda \leq z_m \leq \lambda \quad \forall m \in \{1, \dots, M\}, \quad (57d)$$

$$-L \leq y_m \leq L \quad \forall m \in \{1, \dots, M\}, \quad (57e)$$

$$y_m - y_{m-1} \geq \lambda/2 \quad \forall m \in \{2, \dots, M\}. \quad (57f)$$

Constraint (57b) represents the jammer's power budget limit. Constraints (57c) and (57d) define the permitted movement region for the MAs within the (X, Z) plane. The typical size of the antenna moving region is in the order of several wavelengths [26], however the most common value in research is a distance of $\pm\lambda$ around the x and z axes. As previously mentioned, the MAs in this architecture are free to move along the entire length $2L$ of the array on the y -axis, as specified in (57e), provided they maintain a minimum spacing of $\lambda/2$ between each other, as ensured by (57f). Since the jammer lacks information about the BS-user links or the BS beamforming vectors, its objective is to align its beamforming with each jammer-user channel to maximize interference. Therefore, the problem is formulated as follows.

$$\mathcal{P}' : \min_{\mathbf{V}, \mathbf{P}} - \sum_{k \in \mathcal{K}} |\mathbf{h}_{J,k}^H(\mathbf{P}) \cdot \mathbf{v}_k|^2 \quad (58a)$$

$$\text{s.t.} \quad (57b) - (57f). \quad (58b)$$

The problem \mathcal{P}' is a non-convex optimization problem for two main reasons. First, the dependence on antenna location matrix \mathbf{P} in the jammer-user channel $\mathbf{h}_{J,k}^H$ is non linear, making the objective function non-convex. Additionally, constraints (57c)-(57e) are obviously non-convex.

4.4.3 Solution Approach

Given the non-convexity of problem \mathcal{P}' and the coupling between variables \mathbf{P} and \mathbf{V} in the objective function, we divide the problem into two sub-problems that will be solved iteratively until convergence. In each sub-problem, we focus on optimizing a set of variables while fixing the rest, which is usually referred to as block coordinate descent (BCD) or alternating optimization. The detailed algorithm is described in Algorithm 2.

Algorithm 2 Joint Optimization of \mathbf{V} and \mathbf{P}

```

1: Input:  $\mathbf{p}_m^{(0)} = [x_m^{(0)}, y_m^{(0)}, z_m^{(0)}]^T \forall m \in \mathcal{M}, \mathbf{v}_k^{(0)} \forall k \in \mathcal{K}, \lambda, \epsilon, T_{1,\max}, T_{2,\max}, \mathbf{g}_k \forall k \in \mathcal{K},$   

    $\vartheta_{k,i}^t, \varphi_{k,i}^t, \omega_{k,i}^t$  for  $1 \leq i \leq L_k^t, \forall k \in \mathcal{K}$ 
2: Output:  $\mathbf{p}_m^{opt} \forall m \in \mathcal{M}, \mathbf{v}_k^{opt} \forall k \in \mathcal{K}$ 
3: Set  $i = 0$ 
4: while  $\|\mathbf{V}^{(i+1)} - \mathbf{V}^{(i)}\|_F > \epsilon$  and  $\|\mathbf{P}^{(i+1)} - \mathbf{P}^{(i)}\|_F > \epsilon$  and  $i < T_{1,\max}$  do
5:   Set  $t = 0, \mathbf{V}^{(t)} = \mathbf{V}^{(i)}$ 
6:   while  $\|\mathbf{V}^{(t+1)} - \mathbf{V}^{(t)}\|_F > \epsilon$  and  $t < T_{2,\max}$  do
7:     Compute  $\nabla_{\mathbf{V}} \Psi^{(t)}$  using the current value of  $\mathbf{P}$ 
8:     Solve  $\mathcal{P}_1$  to obtain  $\mathbf{V}^{(t+1)}$ 
9:     Update  $\mathbf{V}^{(t)} = \mathbf{V}^{(t+1)}$ 
10:     $t = t + 1$ 
11:   end while
12:   Update  $\mathbf{V}^{(i+1)} = \mathbf{V}^{(t)}$ 
13:   Set  $t = 0, \mathbf{P}^{(t)} = \mathbf{P}^{(i)}$ 
14:   while  $\|\mathbf{P}^{(t+1)} - \mathbf{P}^{(t)}\|_F > \epsilon$  and  $t < T_{2,\max}$  do
15:     Compute  $\nabla_{\mathbf{P}} \Phi^{(t)}$  using the current value of  $\mathbf{V}$ 
16:     Solve  $\mathcal{P}_2$  to obtain  $\mathbf{P}^{(t+1)}$ 
17:     Update  $\mathbf{P} = \mathbf{P}^{(t+1)}$ 
18:     $t = t + 1$ 
19:   end while
20:   Update  $\mathbf{P}^{(i+1)} = \mathbf{P}^{(t)}$ 
21:    $i = i + 1$ 
22: end while

```

Optimizing the beamforming matrix \mathbf{V}

In this subproblem, the antenna position matrix \mathbf{P} is fixed. Thus, the optimization problem can be reduced to the following problem:

$$\mathcal{P}_1 : \min_{\mathbf{V}} \Psi(\mathbf{V}) \triangleq - \sum_{k \in \mathcal{K}} |\mathbf{h}_{J,k}^H(\mathbf{P}) \cdot \mathbf{v}_k|^2 \quad (59a)$$

$$\text{s.t. (57b).} \quad (59b)$$

The function Ψ is concave, thus to have a convex objective, we apply a first-order Taylor expansion around a point $\Psi^{(t)}$ as:

$$\Psi = \Psi^{(t)} + \nabla_{\mathbf{V}} \Psi^{(t)} \cdot (\mathbf{V} - \mathbf{V}^{(t)}), \quad (60)$$

where, $\nabla_{\mathbf{V}} \Psi^{(t)}$ is the Jacobian of Ψ with respect to \mathbf{V} , evaluated at $\mathbf{V}^{(t)} = [\mathbf{v}_1^{(t)}, \mathbf{v}_2^{(t)}, \dots, \mathbf{v}_K^{(t)}]$.

The new formulation for the problem is:

$$\mathcal{P}_1 : \min_{\mathbf{V}} \nabla_{\mathbf{V}} \Psi^{(t)} \cdot (\mathbf{V} - \mathbf{V}^{(t)}) \quad (61a)$$

$$\text{s.t. (57b).} \quad (61b)$$

This convex problem is solved iteratively with CVX [34], beginning from a feasible starting point $\mathbf{V}^{(0)}$ and continuing until convergence, which is determined by reaching a specified tolerance ϵ or the maximum number of iterations $T_{2,max}$.

Optimizing the antenna-position matrix \mathbf{P}

In this subproblem, the beamforming matrix \mathbf{V} is now fixed, and the new optimization problem can be expressed as:

$$\mathcal{P}_2 : \min_{\mathbf{P}} \Phi(\mathbf{P}) \triangleq - \sum_{k \in \mathcal{K}} |\mathbf{h}_{J,k}^H(\mathbf{P}) \cdot \mathbf{v}_k|^2 \quad (62a)$$

$$\text{s.t. (57c) – (57f).} \quad (62b)$$

To alleviate the non-convexity from the objective function, we use a similar technique to the first sub-problem as follows.

$$\Phi = \Phi^{(t)} + \nabla_{\mathbf{P}} \Phi^{(t)} \cdot (\mathbf{P} - \mathbf{P}^{(t)}), \quad (63)$$

where, $\nabla_{\mathbf{P}} \Phi^{(t)}$ is the Jacobian of Φ with respect to \mathbf{P} , evaluated at $\mathbf{P}^{(t)} = [\mathbf{p}_1^{(t)}, \mathbf{p}_2^{(t)}, \dots, \mathbf{p}_M^{(t)}]$. Constraint (57f) is convex, however, (57c)-(57e) need to be transformed into the following convex constraints:

$$x_m \leq \lambda, \quad -x_m \leq \lambda \quad (64)$$

$$z_m \leq \lambda, \quad -z_m \leq \lambda \quad (65)$$

$$y_m \leq L, \quad -y_m \leq L. \quad (66)$$

Using the above approximations, problem \mathcal{P}_2 is written as:

$$\mathcal{P}_2 : \min_{\mathbf{P}} \nabla_{\mathbf{P}} \Phi^{(t)} \cdot (\mathbf{P} - \mathbf{P}^{(t)}) \quad (67a)$$

$$\text{s.t. (57f), (64) – (66).} \quad (67b)$$

Similar to the first sub-problem, \mathcal{P}_2 is a convex problem that can be iteratively solved with CVX [34], starting from a feasible point $\mathbf{P}^{(0)}$ and continuing until convergence.

4.4.4 Simulation Results and Discussion

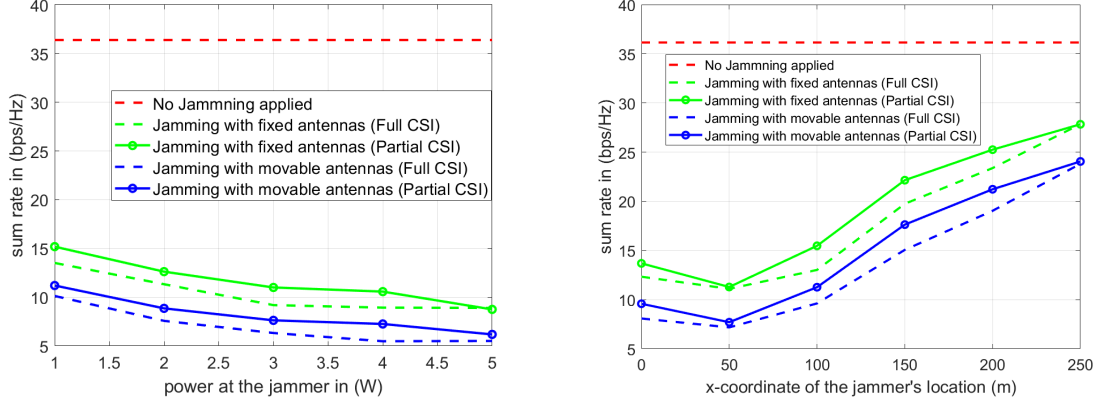
In this section, we analyze the performance of the proposed MA-enhanced jamming algorithm through simulations, focusing on its effectiveness in maximizing interference against legitimate users. We present key performance metrics to evaluate the impact of MAs in various jamming scenarios, comparing these results to conventional FPAs.

Simulation Setup

The simulation setup is as follows: the BS is positioned at (0, 0), while users are uniformly distributed within a circular area of radius 40 m centered at (50, 50). The jammer is located at (100, 0). All coordinates are given in meters.

Parameter	Value	Parameter	Value
α_{BS}, α_J	2.8	ρ_o	-30 dB
P_{BS}	40 dBm	g_o	-40 dB
P_J	30 dBm	σ^2	-80 dBm
K,N,M	4	$R_{th,k}$	1 bps/Hz
L_t, L_r	6	λ	0.01 m

Table 4.1: Simulation Parameters



(a) Sum rate change according to the available power at the jammer (b) Sum rate change according to the jammer's location

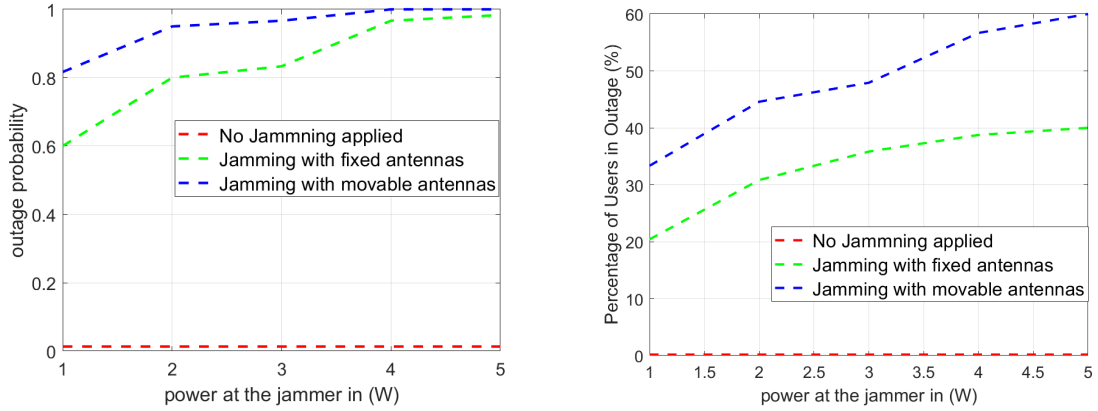
Figure 4.3: Comparison of sum rate variation with respect to jammer power and location

We adopt the PRM matrix model used in [25], where the PRM for each user k , $\Sigma_k = \text{diag}\{\sigma_1, \sigma_2, \dots, \sigma_L\}$, is a diagonal matrix where each diagonal element σ_i follows a circularly symmetric complex Gaussian (CSCG) distribution, $\mathcal{CN}(0, \frac{c_k^2}{L})$. Here, $c_k^2 = g_0 d_k^{-\alpha_J}$ represents the expected channel power gain for user k , with g_0 denoting the average channel power gain at a reference distance of 1 meter, and α_J being the path-loss exponent.

The elevation and azimuth AoDs and AoAs for the channel paths of each user location are modeled as random variables with a joint probability density function (PDF) given by $f_{\theta_k, \phi_k}(\theta_k, \phi_k) = \frac{\cos \theta_k}{2\pi}$, where $\theta_k \in [-\frac{\pi}{2}, \frac{\pi}{2}]$ and $\phi_k \in [-\frac{\pi}{2}, \frac{\pi}{2}]$. Key simulation parameters are summarized in Table 4.1 and remain consistent across all simulations unless specified otherwise.

Impact on the system sum-rate

As previously mentioned, the jammer is assumed to possess only the CSI of its connections with each user. To evaluate the performance of jamming with MAs against conventional FPAs, while



(a) Outage probability versus the jamming power budget (b) Percentage of users in outage versus the jamming power

Figure 4.4: Analysis of system outage probability with respect to jamming power

also considering the implications of lacking BS-user CSI and BS beamforming on the jammer's optimization, we define and compare the following baseline scenarios:

- **Jamming with Fixed Antennas (Full CSI):** The jammer employs an FPA to disrupt communication while having access to both its jammer-user channels and complete BS information, which includes BS-user CSI and beamforming details.
- **Jamming with Fixed Antennas (Partial CSI):** In this scenario, the jammer utilizes an FPA but only has CSI about jammer-user channels.
- **Jamming with Movable Antennas (Full CSI):** Here, the jammer employs MA-enabled jamming, having full access to all system information.
- **Jamming with Movable Antennas (Partial CSI):** In this case, the jammer only possesses jammer-user CSI while using an MA array.

The analysis of the impact of jamming on the sum rate performance, based on varying jammer locations and power is conducted in Fig 4.3. The simulations were conducted using the Monte-Carlo method, with results averaged over 100 different channel realizations. In the absence of jamming, the system achieves a stable sum rate of about 36 bps/Hz, serving as a baseline. When a jammer is introduced, its effectiveness varies significantly depending on its configuration.

In Fig. 4.3a, we present the system sum rate achieved based on the power budget available at the jammer. As anticipated, the intensity of jamming, whether using MAs or FPAs, increases with the jammer’s power. Notably, jamming with MAs proved to be, on average, 30% more effective than using FPAs, resulting in an average reduction of 4 (bps/Hz) across all simulation points. Additionally, MA-based jamming results in a 15% greater reduction in sum rate than its FPA counterpart compared to the baseline value when no jamming is applied. This significant difference could be a crucial factor in disrupting sensitive communication scenarios. Another noteworthy observation is that the difference in results between having partial CSI and full CSI is minimal, demonstrating the effectiveness of this jamming optimization despite its simplicity. In fact, the only requirement for the jammer is to estimate the CSI of its channels.

The impact of the jammer’s location on the system sum rate is illustrated in Fig. 4.3b through the variation of the jammer’s x-coordinate. The differences in values between jamming with MAs and FPAs continue to reflect the same gain percentages discussed in Fig. 4.3a, thereby confirming the validity of the results. Jamming is most effective when the jammer is closest to the users, particularly near the center of the user distribution ($x_{jammer} = 50\text{ m}$). When positioned at equal distance from the center of the users, there is no significant difference in the achieved sum rate whether the jammer is located on the side of the BS ($x_{jammer} = 0\text{ m}$) or the opposite side ($x_{jammer} = 100\text{ m}$), indicating that the effectiveness of jamming primarily relies on the channel conditions between the jammer and the users. However, jamming from the BS side is slightly more effective, as the jammer can generate stronger interference with to BS-user links. This modest performance increase encourages the jammer to position itself on the opposite side of the BS to maximize its distance. Greater distance weakens the jammer’s signal at the BS, making it harder to detect through signal strength-based techniques. Ultimately, as the jammer moves further from the center of the users, the intensity of jamming decreases.

Impact on the system outage probability

A critical factor in physical layer security is the outage probability $P_{\text{system outage}}$, defined as the probability of at least one user having a rate below the rate threshold. $P_{out,k}$ denotes the probability

of outage of user k given as:

$$P_{\text{out},k} = P(R_k < R_{\text{th}}), \quad \forall k \in \mathcal{K}. \quad (68)$$

Since users are assumed to have independent channels, the probability that all users avoid outage (i.e., each user k meets $R_k \geq R_{\text{th}}$) is given by:

$$P_{\text{no outage}} = \prod_{k=1}^K (1 - P_{\text{out},k}). \quad (69)$$

Thus, the system outage probability is expressed as:

$$P_{\text{system outage}} = 1 - P_{\text{no outage}} = 1 - \prod_{k=1}^K (1 - P_{\text{out},k}). \quad (70)$$

In Fig. 4.4, we evaluate the system outage probability when the jammer power varies between 1 and 5 W, through Monte Carlo simulation of 100 different channel realizations, where the rate threshold for each user is $R_{th} = 1$ bps/Hz. In the absence of jamming, the system maintains an outage probability of zero, as expected without interference. Fig. 4.4a illustrates that jamming with fixed antennas yields an outage probability starting at 0.6 at 1 W and rising to approximately 0.95 by 5 W. However, jamming with MAs proves more disruptive, with the outage probability beginning around 0.75 at 1 W and approaching 1 by just 3.5 W. This demonstrates that MAs increase the outage probability more significantly—by about 0.2 across the power range—making MA arrays roughly 25% more effective than FPAs at disrupting service for legitimate users.

To deepen the analysis, we track the percentage of users experiencing outages among all users, as shown in Fig. 4.4b. With jamming from FPAs, around 20% of users are in outage at 1 W, rising moderately to 40% at 5 W. In contrast, jamming with MAs starts at 30% outage at 1 W and climbs sharply to about 60% at 5 W, showing a linear-like increase in user disruptions. While the outage rate with FPAs begins to plateau near 40%, MAs continue to increase steadily, with a performance gain that becomes more pronounced as power increases. This suggests that MAs cause more widespread outages, affecting roughly 15% more users than FPAs at low power levels and up to 20% more at 5W. Overall, the higher outage rates with MAs underscore the importance of implementing effective

countermeasures in network design.

To sum up, our investigation into an MA-enhanced jamming system revealed significant vulnerabilities that arise when such advanced technologies are exploited for malicious purposes. The results demonstrate that jamming using MAs is substantially more effective than FPAs. These findings underscore the necessity of developing advanced security protocols that can adapt to the evolving landscape of wireless technology and counteract the threats posed by the unauthorized use of MAs in communication networks.

4.5 Performance Analysis of RIS in mitigating MA-enabled Jamming in Downlink Wireless Networks

4.5.1 System Model

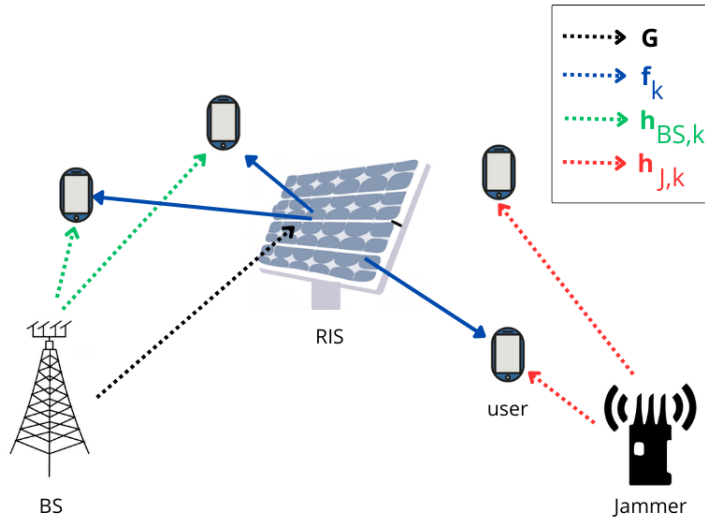


Figure 4.5: System model

In this chapter, we consider the previously discussed system model, but now with an RIS, positioned at $(50\text{ m}, 50\text{ m})$, assisting BS-user downlink communication as depicted in Fig. 4.5. Specifically, we consider a passive reflective RIS as described in Section 2.3.1, employing 32 reflective elements. Under this setup, the received signal at user k is given by:

$$y_k = \tilde{\mathbf{h}}_{BS,k}^H \mathbf{w}_k s_k + \mathbf{h}_{J,k}^H \mathbf{v}_k q_k + n_k, \forall k \in \mathcal{K}, \quad (71)$$

where $\tilde{\mathbf{h}}_{BS,k} \in \mathbb{C}^{N \times 1}$ represents the combined BS-user channel, including both direct BS transmission and RIS reflection. It is expressed as:

$$\tilde{\mathbf{h}}_{BS,k} = \mathbf{h}_{BS,k} + \mathbf{G}\Theta\mathbf{f}_k, \forall k \in \mathcal{K}, \quad (72)$$

where $\mathbf{G} \in \mathbb{C}^{N \times N_{RIS}}$ denotes the BS-RIS channel, and $\mathbf{f}_k \in \mathbb{C}^{N_{RIS} \times 1}$ represents the RIS-user channel. The achievable rate for user k is then given by:

$$R_k = \log_2 \left(1 + \frac{|\tilde{\mathbf{h}}_{BS,k}^H \mathbf{w}_k|^2}{\sum_{\substack{j \in \mathcal{K} \\ j \neq k}} |\tilde{\mathbf{h}}_{BS,k}^H \mathbf{w}_j|^2 + \sum_{j \in \mathcal{K}} |\mathbf{h}_{J,k}^H \mathbf{v}_j|^2 + \sigma_k^2} \right), \forall k \in \mathcal{K}, \quad (73)$$

which closely resembles the rate expression in Section 4.4.1, except for the enhanced BS-user channel. The BS-user and jammer-user channels follow the definitions in Section 4.4.1, while the RIS-related channels are defined analogously to Section 3.6.1. For clarity, we briefly remind the reader with the key channel models as follows:

- $\mathbf{h}_{J,k}(\mathbf{P}) = \mathbf{F}_k^H(\mathbf{P})\Sigma_k\mathbf{g}_k, \forall k \in \mathcal{K},$
- $\mathbf{h}_{BS,k} = \sqrt{PL(d_{BS,k})} \mathbf{h}_{BS,k}^{NLOS}, \forall k \in \mathcal{K},$
- $\mathbf{f}_k = \sqrt{\frac{PL(d_{RU})}{k_{RU}+1}} (\sqrt{k_{RU}} \mathbf{f}_k^{LOS} + \mathbf{f}_k^{NLOS}), \forall k \in \mathcal{K},$
- $\mathbf{G} = \sqrt{\frac{PL(d_{BR})}{k_{BR}+1}} (\sqrt{k_{BR}} \mathbf{G}^{LOS} + \mathbf{G}^{NLOS}).$

4.5.2 Problem Formulation

Jammer's Objective

The jammer's objective remains the same as in the previous chapter: leveraging its MA-array to minimize the system sum rate, thereby disrupting the communication links of legitimate users. The problem follows the same formulation as in Section 4.4.2. However, we distinguish between two cases in our analysis:

- **Scenario 1:** The jammer is aware of the RIS and has full knowledge of the combined channel $\tilde{h}_{BS,k}$. This represents the most favorable scenario for the jammer and the most challenging one for the BS.
- **Scenario 2:** The jammer is unaware of the RIS and only has knowledge of the direct jammer-user CSI. This corresponds to the least favorable case for the jammer.

By analyzing the two described scenarios, we establish both the upper and lower bounds on the jammer’s impact, and provide insights into the effectiveness of RIS in countering jamming under varying levels of adversarial knowledge.

Base Station’s Objective

In this section, we detail how the BS leverages RIS to counteract jamming attacks. As jamming intensifies, multiple users begin reporting communication failures, enabling the BS to infer the presence of a jammer. Once a jamming attack is suspected, the BS initiates a two-stage response. First, it employs power sensing sweeps to localize the jammer based on its emission signature—techniques such as the MUSIC algorithm or Capon’s beamforming method can be used for this purpose, although a detailed discussion of these established localization methods is beyond the scope of this work. Following localization, the BS estimates the jammer-user CSI across the network by solving an optimization problem analogous to that employed by the jammer. This process yields the optimized MA positions and corresponding beamforming vectors, thereby approximating the CSI for all jammer-user links. The primary unknown parameter remains the jammer’s power budget; to address this, the BS adopts a worst-case approach, assuming the maximum reasonable power level (e.g., 5 W in our scenario).

For the purpose of our analysis, we assume that the BS has complete CSI knowledge of all jammer-user links. Given this information, the BS aims to optimize its beamforming strategy to mitigate the impact of jamming as effectively as possible. The optimization problem can be formulated as follows.

$$\mathcal{P}_3 : \max_{\mathbf{p}} \sum_{k \in \mathcal{K}} R_k \quad (74a)$$

$$\text{s.t.} \quad \sum_{j \in \mathcal{K}} \|\mathbf{p}_j\|^2 \leq P_{BS}, \quad (74b)$$

$$R_k \geq R_{min,k}, \quad \forall k \in \mathcal{K}, \quad (74c)$$

$$|e^{j\theta_i}| = 1, \quad \forall i \in \{1 \dots N\}, \quad (74d)$$

where (74b) guarantees compliance with the power budget at the BS, and (74c) ensures the minimum quality of service required by each user in the system. (74d) is the unit modulus constraint related to the RIS. It is observed that \mathcal{P}_3 is a non-convex optimization problem due to the non-convex objective function (74a) and the non-convex constraints (74c) and (74d). The solution to this problem employs an approach analogous to the SCA-based algorithm outlined in Section 3.4.3. For brevity, we have not repeated the detailed steps here.

4.5.3 Simulation Results and Discussion

Jamming impact on system sum rate

Figure 4.6 offers several key insights into the impact of RIS on system performance under different jamming conditions. As expected, the presence of RIS enhances the system’s sum rate, as evidenced by the performance gap between the curves with and without RIS in the absence of jamming. However, an intriguing finding emerges when the jammer possesses full CSI knowledge, including RIS-related CSI—under such conditions, the RIS provides little to no advantage, regardless of whether the jammer employs FPAs or MAs. The near-identical performance of the “NO RIS” and “known RIS” cases in both jamming scenarios, further shown in Fig. 4.7a, highlights a critical vulnerability: without proper security measures, RIS becomes an ineffective resource, offering no tangible benefits. This underscores the necessity of securing CSI information through robust encryption techniques and countermeasures against information leakage, ensuring that RIS can function as an asset rather than a wasted complexity.

Another noteworthy comparison arises in the "blind jamming" scenario, where the jammer lacks RIS-user CSI and only has knowledge of its own channels to the users. As previously mentioned, the jammer can estimate these channels before initiating its attack without requiring additional effort to intercept RIS-related CSI. In this case, the RIS proves beneficial, mitigating the impact of jamming and yielding a higher sum rate than the "NO RIS" case for both jamming techniques. Surprisingly, however, the FPA-based blind jamming achieves a stronger jamming effect than the MA-based approach, an observation that challenges initial expectations and warrants further analysis which will be done in section "Impact on system outage probability". This observation is shown separately in Fig. 4.7b for the reader's convenience.

Finally, when the jammer has full CSI knowledge, the MA-based jamming strategy once again proves superior, reducing the system sum rate by approximately 30% more than FPAs, as previously observed in Section 4.4.5. The performance gain from full CSI access can be quantified as an average improvement of 66% for MAs and 44% for FPAs. In other words, complete CSI knowledge enhances the efficiency of MAs by 66% and FPAs by 44%, with the additional information providing a 33% greater advantage to MAs compared to FPAs. This further reinforces the need for stringent security measures to limit the jammer's access to CSI, ensuring it remains as blind as possible.

The key takeaway from this analysis is that RIS deployment must be both strategic and secure. If improperly secured, RIS can become a liability rather than an asset, offering no protection and potentially worsening network performance when the jammer has full CSI access. However, when effectively shielded from the jammer, RIS can mitigate the impact of jamming, particularly reducing the effectiveness of MA-based attacks, thereby preserving system sum rate and justifying its inclusion in the network. It's important also to note that the extent to which the RIS can help is significantly reduced as the jammer's power budget increases as it is expressed by the decreasing nature of the curves for all the configurations.

Jamming impact on percentage of jammed users

From figures. 4.8 and 4.9, we observe a consistent trend across all configurations, mirroring the insights drawn from the sum rate analysis. As the jammer's power budget increases—enhancing its disruptive capabilities—the number of users experiencing outages rises accordingly. Notably,

when the jammer has full CSI knowledge, the presence of RIS offers no tangible benefit, reinforcing the earlier conclusion that an unsecured RIS becomes an ineffective addition to the network. Furthermore, in the blind jamming scenario, FPA-based jamming proves more detrimental than its MA-based counterpart, leading to a higher number of jammed users. This aligns with the previously observed sum rate degradation and further emphasizes the need for securing RIS-related CSI to prevent unnecessary system vulnerabilities.

Jamming impact on system outage probability

Figure 4.12 confirms that outage probability trends largely mirror those observed in the sum rate analysis, while also revealing a noteworthy distinction. In the blind jamming scenario, MA-based jamming outperforms FPA-based jamming in terms of outage probability—a reversal of the behavior seen in figures 4.6 and 4.8 for the impact on system sum rate and number of jammed users, respectively. To analyze this, recall that system outage probability is defined as the likelihood that at least one user fails to meet its QoS requirements. Under MA-based jamming, the jammer appears to consistently target and disrupt several users, suggesting a systematic, user-by-user approach. In contrast, FPA-based jamming exhibits a “hit or miss” pattern: it sometimes fails to jam users and, when it does succeed, it tends to affect multiple users simultaneously, but with less consistency overall.

This disparity can be understood by examining the underlying optimization strategies. Without full system information, the MA-based approach seems to allocate its resources sequentially—ensuring one user is effectively jammed before shifting focus to the next. This method, likely affected by the greater degrees of freedom available in MA-based configurations, allows for a more consistent degradation of user QoS. However, it could also be due to the abundance of available optimization directions in a non-convex problem space leading to suboptimal choices or cause the process to become trapped in local maxima preventing the MA-jamming from achieving a bigger percentage of users in outage.

Conversely, FPA-based jamming relies on a single optimization strategy—beamforming—that aims solely to reduce the global sum rate and deny QoS to as many users as possible. Under limited information, this approach is inherently rigid. However, once complete CSI is available, the

jammer can accurately identify the optimal jamming direction, allowing the more flexible MA-based strategy to achieve a significantly greater impact than its FPA-based counterpart.

In summary, while MA-based jamming offers consistent performance in the absence of full CSI by effectively targeting users sequentially, its greater number of optimization paths can sometimes lead to suboptimal outcomes. FPA-based jamming, with its single strategic approach, may occasionally deliver a stronger impact but suffers from inconsistency when operating blind. These observations underscore the importance of comprehensive CSI for optimizing jamming strategies and reinforce the need for robust security measures to limit the jammer’s access to system information.

Impact Analysis of RIS Optimization

In the previous subsections, we evaluated the impact of jamming on a system employing RIS as an initial defense line. Building on those insights, we now assess the effect of an optimized RIS—hereafter referred to as the “Reacting VS Jamming” in the figures—on mitigating jamming once the BS detects the jammer. For clarity, our figures focus solely on the MA-based jamming scenario, comparing the cases where the jammer either has complete RIS-CSI or lacks such information.

Our analysis, based on three performance metrics, consistently shows that optimizing the RIS produces a tangible reduction in jamming impact, regardless of the jammer’s level of information. However, the magnitude of this improvement depends on both the jammer’s power and the QoS requirements imposed on the users.

For instance, when the QoS requirement is relatively low ($R_{th} = 1$ bps/Hz), Fig. 4.10 reveals that the “reacting vs. jamming” curves remain close to zero over most of the jammer’s power range. At its peak power ($P_{jammer} = 5$ W), the maximum outage percentage reaches only 8%, reflecting a reduction of roughly 70% in the jammer’s impact (from about 26% to 8% of affected users). Moreover, under these conditions the curves for both “RIS known” and “RIS unknown” scenarios nearly coincide, indicating that a low QoS requirement simplifies the RIS optimization task.

Conversely, with a higher QoS threshold ($R_{th} = 1.5$ bps/Hz), two key observations emerge from Fig. 4.8: First, the overall effectiveness of the RIS is diminished. For example, at a jammer

power of $3W$, the outage percentage reaches 24% compared to only 2% for the lower QoS requirement—demonstrating a performance sensitivity exceeding 91%. Additionally, at $5W$ the RIS does practically nothing as the number of affected users is the same with and without an optimized RIS which is demonstrated by the collision of the two curves "MA Jamming with known RIS" and "Reacting VS Jamming with known RIS". Second, a notable discrepancy arises between the "Reacting vs Jamming" curves when the jammer possesses complete RIS-CSI versus when it does not, with approximately 12% more users affected in the former case. This observation confirms that the jammer's access to RIS information becomes increasingly detrimental as QoS constraints tighten, underscoring the challenges of defending against MA-based jamming in high-demand scenarios.

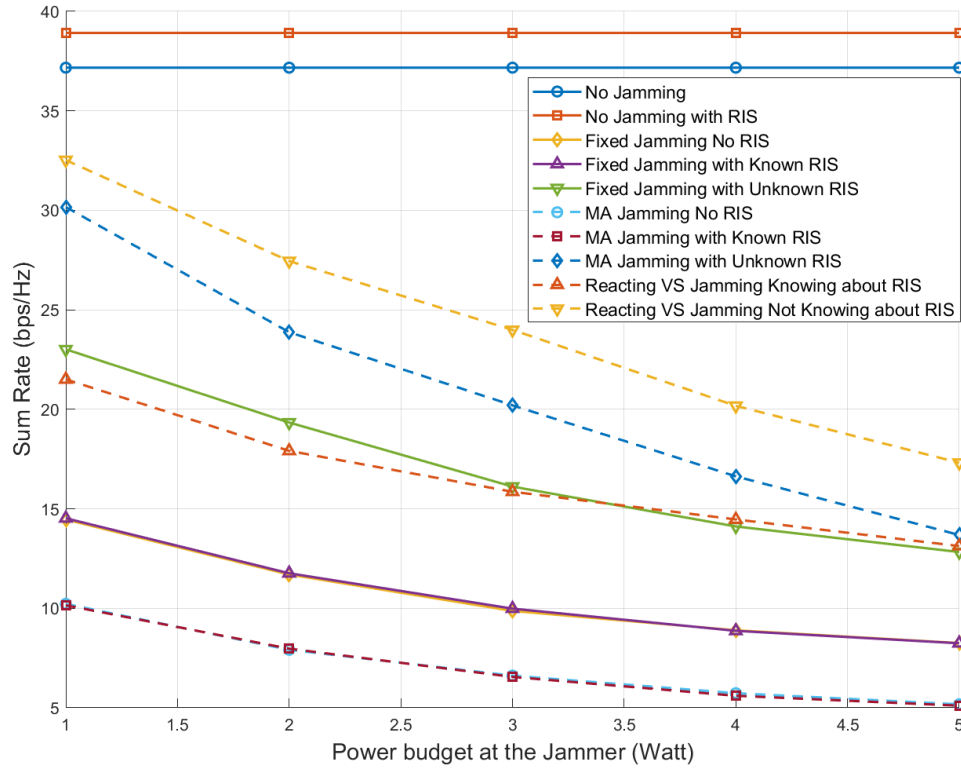
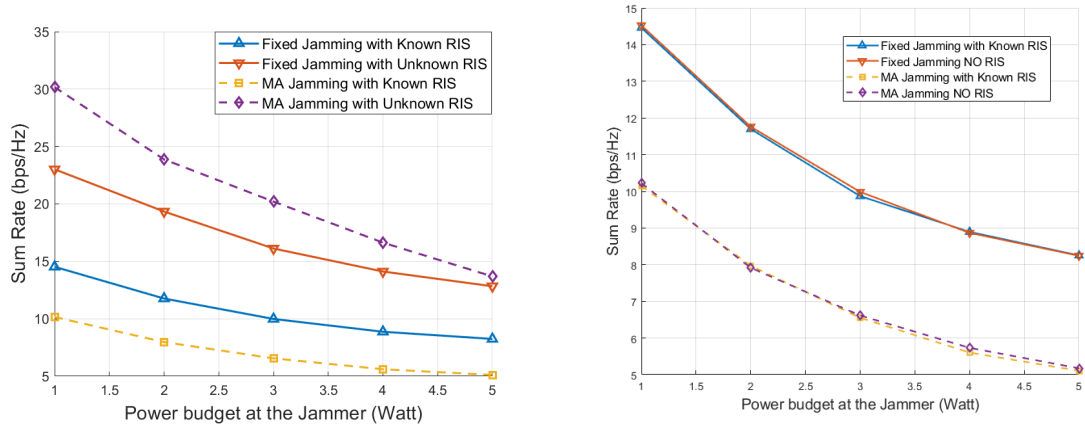


Figure 4.6: Sum rate variation according to the available power at the jammer for all configurations



(a) Blind jamming vs Full-knowledge jamming

(b) Full-knowledge jamming vs Jamming against a system without RIS

Figure 4.7: Comparison of sum rate variation between MA and FPA based jamming as a function of jammer power

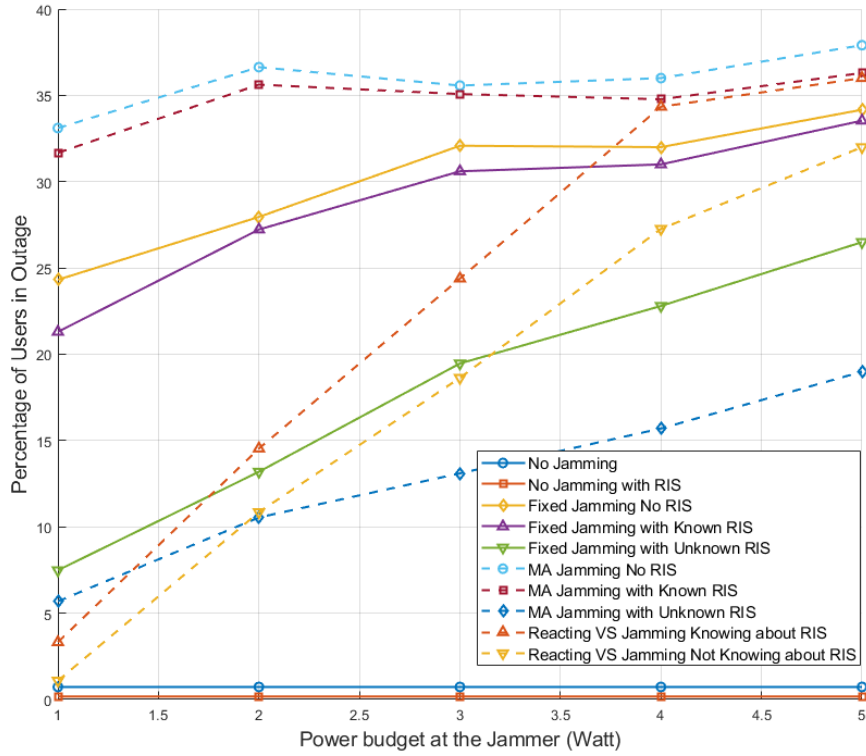
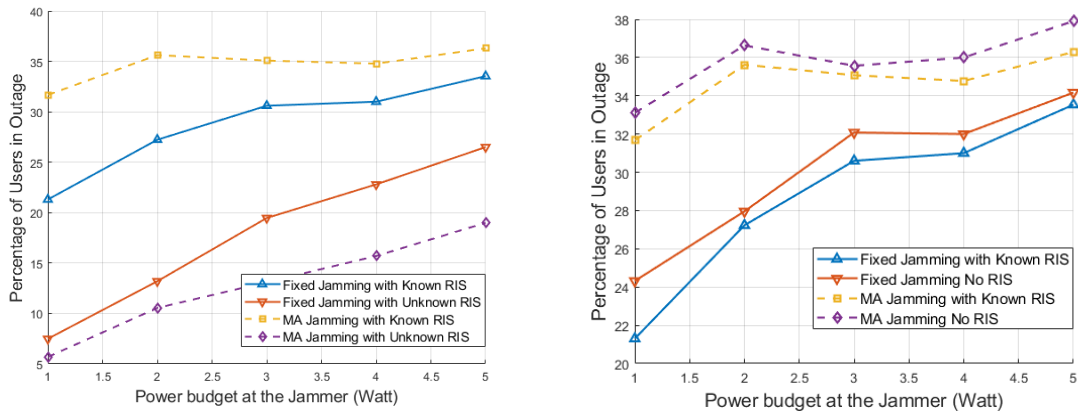


Figure 4.8: Variation in the percentage of users in outage according to the available power at the jammer for all configurations, $R_{th} = 1.5(bps/Hz)$



(a) Blind jamming vs Full-knowledge jamming

(b) Full-knowledge jamming vs Jamming against a system without RIS

Figure 4.9: Comparison of variation in the percentage of users in outage between MA and FPA based jamming as a function of jammer power, $R_{th} = 1.5(bps/Hz)$

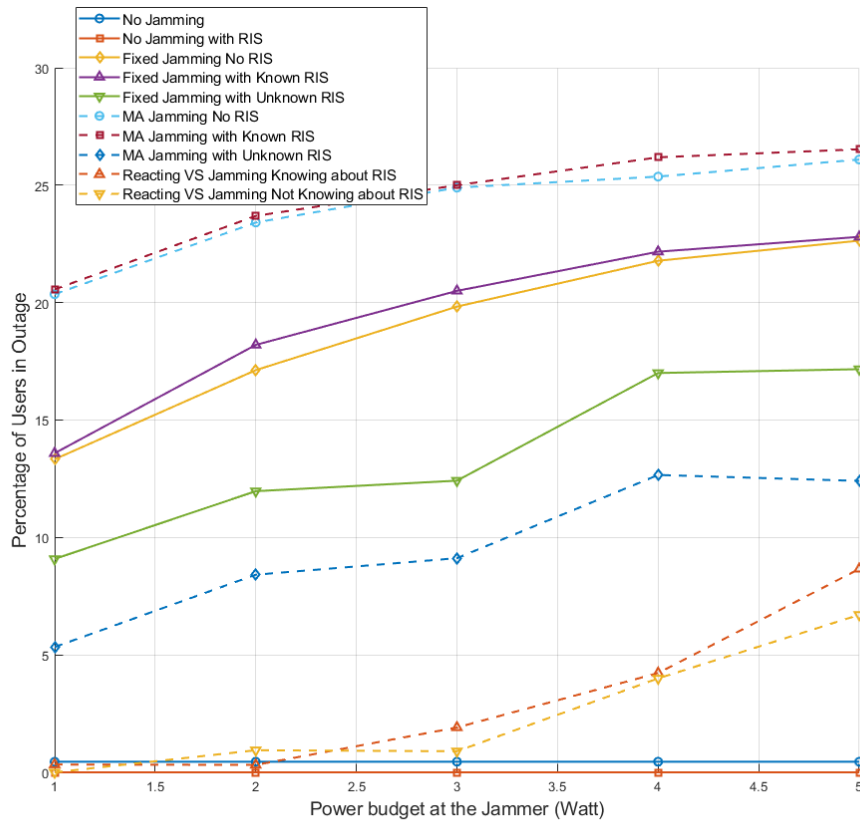
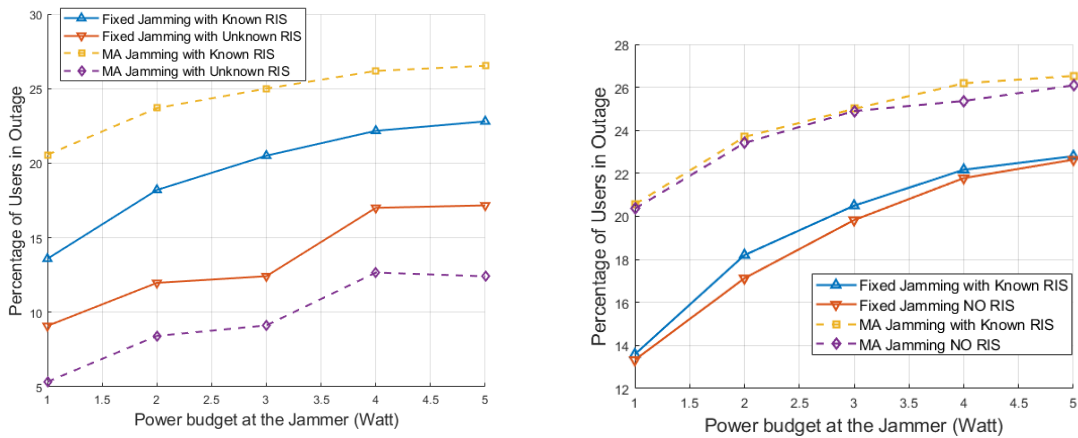


Figure 4.10: Variation in the percentage of users in outage according to the available power at the jammer for all configurations, $R_{th} = 1(bps/Hz)$



(a) Blind jamming vs Full-knowledge jamming

(b) Full-knowledge jamming vs Jamming against a system without RIS

Figure 4.11: Comparison of variation in the percentage of users in outage between MA and FPA based jamming as a function of jammer power, $R_{th} = 1(bps/Hz)$

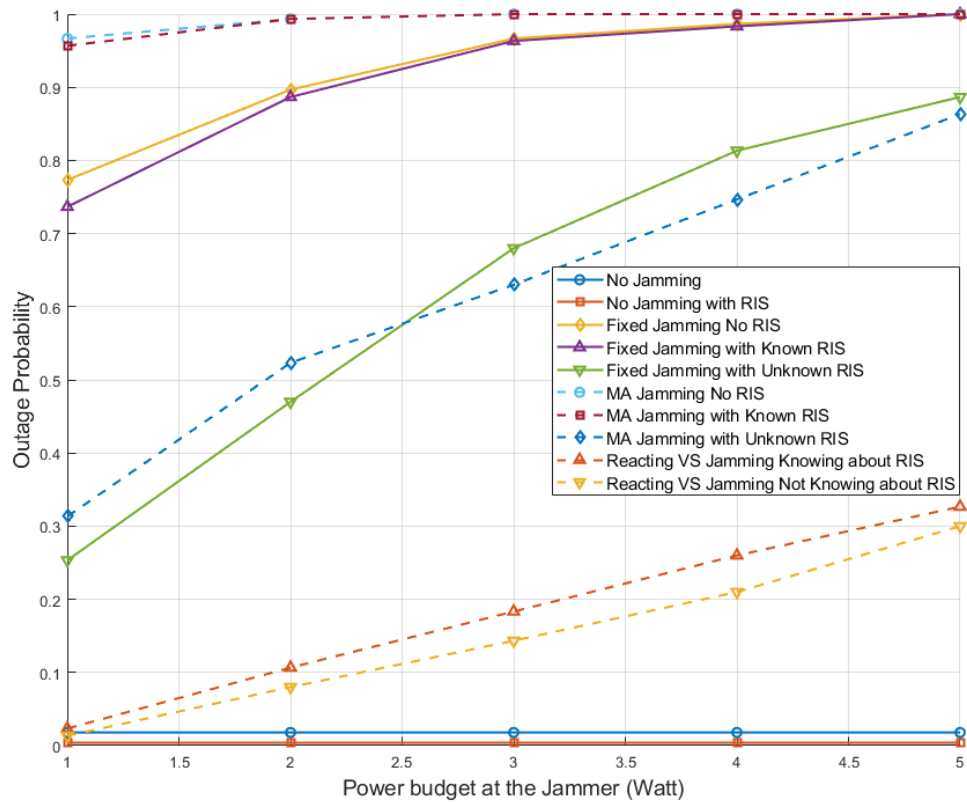
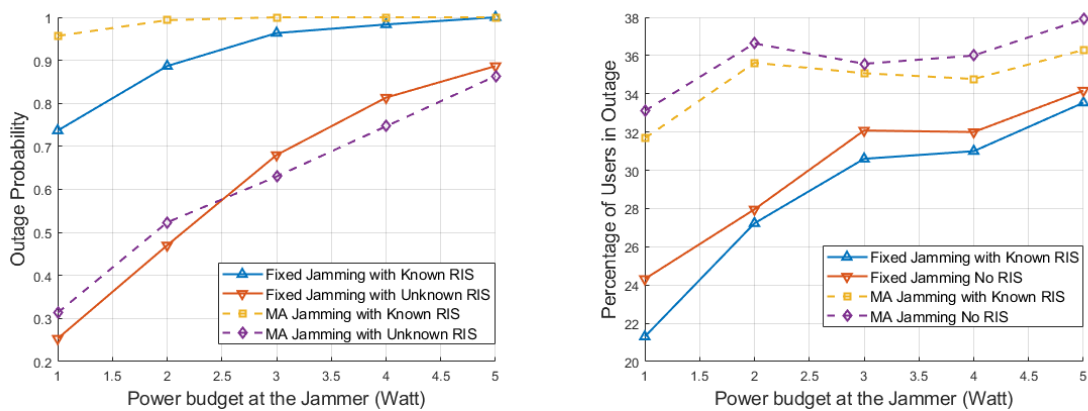


Figure 4.12: System outage probability variation according to the available power at the jammer for all configurations, $R_{th} = 1.5(bps/Hz)$



(a) Blind jamming vs Full-knowledge jamming

(b) Full-knowledge jamming vs Jamming against a system without RIS

Figure 4.13: Comparison of system outage probability variation between MA and FPA based jamming as a function of jammer power, $R_{th} = 1.5(bps/Hz)$

4.6 Summary and Conclusions

In this chapter, we have explored a primitive study on the potential misuse of MA technology in wireless communication, highlighting its associated risks. Our investigation into an MA-enhanced jamming system revealed significant vulnerabilities that arise when such advanced technologies are exploited for malicious purposes. The results demonstrate that jamming using MAs is substantially more effective than FPAs, achieving, on average, a 30% greater impact on system sum rate performance. Our analysis further illustrated that the jammer's location plays a crucial role in jamming efficacy, with proximity to users significantly enhancing the disruption potential. Moreover, jamming with MAs significantly increases system outage probability compared to fixed antennas, with approximately 0.2 higher outage probability across a jammer power range of 1 to 5 W, making MAs about 25% more effective at disrupting communication. Additionally, MAs lead to a greater proportion of users experiencing outages, affecting up to 20% more users at higher power levels. These findings underscore the necessity of developing advanced security protocols that can adapt to the evolving landscape of wireless technology and counteract the threats posed by the unauthorized use of MAs in communication networks.

In light of the growing interest in RIS for next-generation wireless networks, we extended our analysis to evaluate their potential in mitigating MA-based jamming attacks. Our comprehensive assessment—spanning various performance metrics and jamming configurations—reveals several key insights. Notably, when the jammer has full access to RIS-related CSI, the presence of RIS offers no tangible benefit; indeed, the jamming impact remains virtually identical to the scenario without RIS, effectively rendering it a liability rather than an asset. Conversely, when the RIS is properly optimized and its configuration is secured from full CSI exposure, it can substantially alleviate the adverse effects of jamming. Under these conditions, particularly with lower QoS requirements (e.g., $R_{th} = 1 \text{ bps/Hz}$), the optimized RIS reduces both outage probability and sum rate degradation by up to 70%. However, as user QoS demands increase (as observed in the comparison between $R_{th} = 1 \text{ bps/Hz}$ and $R_{th} = 1.5 \text{ bps/Hz}$), the beneficial impact of RIS diminishes rapidly. These results suggest that, by itself, RIS is not a standalone solution for mitigating MA-based jamming attacks. Consequently, exploring advanced RIS architectures, such as active STAR-RIS, emerges as

a promising avenue for future research to further enhance network resilience against sophisticated jamming strategies.

Overall, while MA technology offers promising advancements in connectivity and performance, it is imperative that researchers and practitioners remain vigilant to the security challenges it introduces. Future work should focus on establishing comprehensive frameworks for protecting against the malicious exploitation of MAs, ensuring that the benefits of this technology can be harnessed without compromising the security and reliability of wireless communication systems.

Chapter 5

Conclusion and Future Directions

5.1 Conclusion

This thesis set out to explore the transformative potential of RIS in next-generation wireless networks, addressing both the need for enhanced performance and the imperative for robust security. By combining theoretical analysis, advanced optimization techniques, and deep reinforcement learning, the research provided a comprehensive framework for tackling the inherent challenges of modern wireless communication systems. The following summary highlights the key contributions and findings of this work:

1. **Enhanced Communication Performance:**

The integration of an active STAR-RIS into a C-RSMA downlink system demonstrated a remarkable improvement in spectral efficiency and sum rate performance. By carefully optimizing key system parameters, the proposed scheme consistently outperformed baseline alternatives across diverse scenarios. Moreover, the adoption of a DRL framework—specifically using an actor-critic model—showed promise in reducing computational complexity, thereby paving the way for real-time applications. While the DRL approach exhibits some limitations under strict power constraints, its synergy with traditional convex optimization methods indicates a fruitful avenue for future hybrid techniques.

2. Security and Vulnerability Insights:

On the security front, the investigation into MA-enhanced jamming systems uncovered critical vulnerabilities. The analysis revealed that jamming with MAs significantly degrades system performance—demonstrating a notable increase in outage probability and a more pronounced impact on sum rate compared to fixed antennas. This work not only quantifies the threat posed by MA-based jamming but also highlights the conditional benefits of employing RIS for jamming mitigation. When RIS configurations are properly optimized and shielded from full CSI exposure, they can substantially reduce the detrimental effects of jamming—though this benefit diminishes under higher quality-of-service demands.

3. Interplay Between RIS Optimization and Security:

The dual exploration of RIS for enhancing both communication performance and network security underscores the technology’s transformative potential. While RIS can be leveraged to optimize signal propagation and enhance network reliability, its effective application in countering sophisticated jamming attacks requires further refinement. The findings suggest that RIS should be part of a broader, multi-layered security framework rather than a standalone solution, especially in environments with elevated QoS requirements.

5.2 Future Directions

In summary, this thesis provides a comprehensive analysis of several RIS applications in modern wireless systems, addressing both network performance enhancement and security vulnerability mitigation. The insights lay a robust foundation for future research, which may focus on:

- Localize the error source more precisely and fine-tune the DRL model to achieve better results while exploring other training strategies.
- Evaluate and optimize alternative DRL architectures while exploring hybrid strategies that integrate classical optimization methods with machine learning.
- Investigate cutting-edge RIS configurations, such as active STAR-RIS, to further enhance network resilience against sophisticated jamming attacks.

- Examine the broader implications of MA-based threats, including eavesdropping and coordinated attacker strategies.
- Investigate cooperative RIS deployment and analyze the best placement strategies for RIS in wireless networks.
- Develop robust, adaptive security frameworks to protect next-generation wireless networks from the emerging risks associated with advanced antenna technologies.

Bibliography

- [1] Youssef Maghrebi et al. “Cooperative Rate Splitting Multiple Access for Active STAR-RIS Assisted Downlink Communications”. In: *IEEE Wireless Communications Letters* 13.10 (2024), pp. 2827–2831. DOI: [10.1109/LWC.2024.3448409](https://doi.org/10.1109/LWC.2024.3448409).
- [2] Youssef Maghrebi et al. “A Deep Reinforcement Learning-Driven Optimization for STAR-RIS-empowered Cooperative RSMA”. In: *2024 IEEE Middle East Conference on Communications and Networking (MECOM)*. 2024, pp. 416–421. DOI: [10.1109/MECOM61498.2024.10881479](https://doi.org/10.1109/MECOM61498.2024.10881479).
- [3] Youssef Maghrebi et al. *Movable Antennas in Wireless Systems: A Tool for Connectivity or a New Security Threat?* 2024. arXiv: [2411.06028](https://arxiv.org/abs/2411.06028) [math.OC]. URL: <https://arxiv.org/abs/2411.06028>.
- [4] Yuanwei Liu et al. “Evolution of NOMA Toward Next Generation Multiple Access (NGMA) for 6G”. In: *IEEE Journal on Selected Areas in Communications* 40.4 (2022), pp. 1037–1071. DOI: [10.1109/JSAC.2022.3145234](https://doi.org/10.1109/JSAC.2022.3145234).
- [5] Olaonipekun Oluwafemi Erunkulu et al. “5G Mobile Communication Applications: A Survey and Comparison of Use Cases”. In: *IEEE Access* 9 (2021), pp. 97251–97295. DOI: [10.1109/ACCESS.2021.3093213](https://doi.org/10.1109/ACCESS.2021.3093213).
- [6] Yan Chen et al. “Toward the Standardization of Non-Orthogonal Multiple Access for Next Generation Wireless Networks”. In: *IEEE Communications Magazine* 56.3 (2018), pp. 19–27. DOI: [10.1109/MCOM.2018.1700845](https://doi.org/10.1109/MCOM.2018.1700845).

- [7] Behrooz Makki et al. “A Survey of NOMA: Current Status and Open Research Challenges”. In: *IEEE Open Journal of the Communications Society* 1 (2020), pp. 179–189. DOI: [10.1109/OJCOMS.2020.2969899](https://doi.org/10.1109/OJCOMS.2020.2969899).
- [8] Bruno Clerckx et al. “Is NOMA Efficient in Multi-Antenna Networks? A Critical Look at Next Generation Multiple Access Techniques”. In: *IEEE Open Journal of the Communications Society* 2 (2021), pp. 1310–1343. DOI: [10.1109/OJCOMS.2021.3084799](https://doi.org/10.1109/OJCOMS.2021.3084799).
- [9] Anup Mishra et al. “Rate-Splitting Multiple Access for 6G—Part I: Principles, Applications and Future Works”. In: *IEEE Communications Letters* 26.10 (2022), pp. 2232–2236. DOI: [10.1109/LCOMM.2022.3192012](https://doi.org/10.1109/LCOMM.2022.3192012).
- [10] Yijie Mao et al. “Rate-Splitting Multiple Access: Fundamentals, Survey, and Future Research Trends”. In: *IEEE Communications Surveys & Tutorials* 24.4 (2022), pp. 2073–2126. DOI: [10.1109/COMST.2022.3191937](https://doi.org/10.1109/COMST.2022.3191937).
- [11] Tiantian Li et al. “Full-Duplex Cooperative Rate-Splitting for Multigroup Multicast With SWIPT”. In: *IEEE Transactions on Wireless Communications* 21.6 (2022), pp. 4379–4393. DOI: [10.1109/TWC.2021.3129881](https://doi.org/10.1109/TWC.2021.3129881).
- [12] Phuc Dinh et al. “A Low-Complexity Framework for Joint User Pairing and Power Control for Cooperative NOMA in 5G and Beyond Cellular Networks”. In: *IEEE Transactions on Communications* 68.11 (2020), pp. 6737–6749. DOI: [10.1109/TCOMM.2020.3009262](https://doi.org/10.1109/TCOMM.2020.3009262).
- [13] Intel Corporation. *A holistic study of power consumption and energy savings strategies for Open vRAN systems*. <https://builders.intel.com/docs/networkbuilders/a-holistic-study-of-power-consumption-and-energy-savings-strategies-for-open-vran-systems-1676628842.pdf>. Accessed: February 7th, 2025.
- [14] Paweł Kryszkiewicz et al. “Stochastic power consumption model of wireless transceivers”. In: *Sensors* 20.17 (2020), p. 4704.
- [15] Qin Wang, Mark Hempstead, and Woodward Yang. “A Realistic Power Consumption Model for Wireless Sensor Network Devices”. In: *2006 3rd Annual IEEE Communications Society*

- on Sensor and Ad Hoc Communications and Networks*. Vol. 1. 2006, pp. 286–295. DOI: [10.1109/SAHCN.2006.288433](https://doi.org/10.1109/SAHCN.2006.288433).
- [16] Emil Björnson, Özgecan Özdoğan, and Erik G. Larsson. “Reconfigurable Intelligent Surfaces: Three Myths and Two Critical Questions”. In: *IEEE Communications Magazine* 58.12 (2020), pp. 90–96. DOI: [10.1109/MCOM.001.2000407](https://doi.org/10.1109/MCOM.001.2000407).
- [17] Yijun Feng et al. “Reconfigurable Intelligent Surfaces: Design, Implementation, and Practical Demonstration”. In: *Electromagnetic Science* 1.2 (2023), pp. 1–21. DOI: [10.23919/emsci.2022.0011](https://doi.org/10.23919/emsci.2022.0011).
- [18] Zhengyi Zhou et al. “Joint Transmit Precoding and Reconfigurable Intelligent Surface Phase Adjustment: A Decomposition-Aided Channel Estimation Approach”. In: *IEEE Transactions on Communications* 69.2 (2021), pp. 1228–1243. DOI: [10.1109/TCOMM.2020.3034259](https://doi.org/10.1109/TCOMM.2020.3034259).
- [19] Zhaorui Wang, Liang Liu, and Shuguang Cui. “Channel Estimation for Intelligent Reflecting Surface Assisted Multiuser Communications: Framework, Algorithms, and Analysis”. In: *IEEE Transactions on Wireless Communications* 19.10 (2020), pp. 6607–6620. DOI: [10.1109/TWC.2020.3004330](https://doi.org/10.1109/TWC.2020.3004330).
- [20] Zijian Zhang et al. “Active RIS vs. Passive RIS: Which Will Prevail in 6G?” In: *IEEE Transactions on Communications* 71.3 (2023), pp. 1707–1725. DOI: [10.1109/TCOMM.2022.3231893](https://doi.org/10.1109/TCOMM.2022.3231893).
- [21] Kangchun Zhao, Yijie Mao, and Yuanming Shi. “STAR-RIS Empowered Full Duplex Cooperative Rate Splitting”. In: *2023 IEEE 98th Vehicular Technology Conference (VTC2023-Fall)*. 2023, pp. 1–5. DOI: [10.1109/VTC2023-Fall60731.2023.10333710](https://doi.org/10.1109/VTC2023-Fall60731.2023.10333710).
- [22] Shuang Zhang et al. “Joint Beamforming Optimization for Active STAR-RIS-Assisted ISAC Systems”. In: *IEEE Transactions on Wireless Communications* 23.11 (2024), pp. 15888–15902. DOI: [10.1109/TWC.2024.3434963](https://doi.org/10.1109/TWC.2024.3434963).

- [23] Boyu Ning et al. *Movable Antenna-Enhanced Wireless Communications: General Architectures and Implementation Methods*. 2024. arXiv: [2407.15448](https://arxiv.org/abs/2407.15448) [eess.SP]. URL: <https://arxiv.org/abs/2407.15448>.
- [24] Lipeng Zhu, Wenyan Ma, and Rui Zhang. “Movable Antennas for Wireless Communication: Opportunities and Challenges”. In: *IEEE Communications Magazine* 62.6 (2024), pp. 114–120. DOI: [10.1109/MCOM.001.2300212](https://doi.org/10.1109/MCOM.001.2300212).
- [25] Lipeng Zhu et al. “Movable-Antenna Enhanced Multiuser Communication via Antenna Position Optimization”. In: *IEEE Transactions on Wireless Communications* 23.7 (2024), pp. 7214–7229. DOI: [10.1109/TWC.2023.3338626](https://doi.org/10.1109/TWC.2023.3338626).
- [26] Lipeng Zhu, Wenyan Ma, and Rui Zhang. “Modeling and Performance Analysis for Movable Antenna Enabled Wireless Communications”. In: *IEEE Transactions on Wireless Communications* 23.6 (2024), pp. 6234–6250. DOI: [10.1109/TWC.2023.3330887](https://doi.org/10.1109/TWC.2023.3330887).
- [27] Zhaohui Yang et al. “Downlink Sum-Rate Maximization for Rate Splitting Multiple Access (RSMA)”. In: *ICC 2020 - 2020 IEEE International Conference on Communications (ICC)*. 2020, pp. 1–6. DOI: [10.1109/ICC40277.2020.9149417](https://doi.org/10.1109/ICC40277.2020.9149417).
- [28] Yijie Mao, Bruno Clerckx, and Victor O.K. Li. “Energy Efficiency of Rate-Splitting Multiple Access, and Performance Benefits over SDMA and NOMA”. In: *2018 15th International Symposium on Wireless Communication Systems (ISWCS)*. 2018, pp. 1–5. DOI: [10.1109/ISWCS.2018.8491100](https://doi.org/10.1109/ISWCS.2018.8491100).
- [29] Yijie Mao et al. “Max-Min Fairness of K-User Cooperative Rate-Splitting in MISO Broadcast Channel With User Relaying”. In: *IEEE Transactions on Wireless Communications* 19.10 (2020), pp. 6362–6376. DOI: [10.1109/TWC.2020.3002891](https://doi.org/10.1109/TWC.2020.3002891).
- [30] Shreya Khisa et al. “Energy Consumption Optimization in RIS-Assisted Cooperative RSMA Cellular Networks”. In: *IEEE Transactions on Communications* 71.7 (2023), pp. 4300–4312. DOI: [10.1109/TCOMM.2023.3270907](https://doi.org/10.1109/TCOMM.2023.3270907).

- [31] Shreya Khisa et al. “Full Duplex Cooperative Rate Splitting Multiple Access for a MISO Broadcast Channel With Two Users”. In: *IEEE Communications Letters* 26.8 (2022), pp. 1913–1917. DOI: [10.1109/LCOMM.2022.3173894](https://doi.org/10.1109/LCOMM.2022.3173894).
- [32] Yuanbin Chen et al. “Robust Beamforming for Active Reconfigurable Intelligent Omni-Surface in Vehicular Communications”. In: *IEEE Journal on Selected Areas in Communications* 40.10 (2022), pp. 3086–3103. DOI: [10.1109/JSAC.2022.3196095](https://doi.org/10.1109/JSAC.2022.3196095).
- [33] Zheng Zhang et al. “Security Enhancement for Coupled Phase-Shift STAR-RIS Networks”. In: *IEEE Transactions on Vehicular Technology* 72.6 (2023), pp. 8210–8215. DOI: [10.1109/TVT.2023.3243545](https://doi.org/10.1109/TVT.2023.3243545).
- [34] Michael Grant and Stephen Boyd. *CVX: Matlab Software for Disciplined Convex Programming, version 2.1*. <https://cvxr.com/cvx>. Mar. 2014.
- [35] Vijay Konda and John Tsitsiklis. “Actor-Critic Algorithms”. In: *Advances in Neural Information Processing Systems*. Ed. by S. Solla, T. Leen, and K. Müller. Vol. 12. MIT Press, 1999.
- [36] Yi Zhang and Jeff Schneider. “Learning Multiple Tasks with a Sparse Matrix-Normal Penalty”. In: *Advances in Neural Information Processing Systems*. Ed. by J. Lafferty et al. Vol. 23. Curran Associates, Inc., 2010.
- [37] Tom Schaul et al. *Prioritized Experience Replay*. 2016. arXiv: [1511.05952 \[cs.LG\]](https://arxiv.org/abs/1511.05952). URL: <https://arxiv.org/abs/1511.05952>.
- [38] Suad Basbug. “Design and Synthesis of Antenna Array With Movable Elements Along Semi-circular Paths”. In: *IEEE Antennas and Wireless Propagation Letters* 16 (2017), pp. 3059–3062. DOI: [10.1109/LAWP.2017.2760348](https://doi.org/10.1109/LAWP.2017.2760348).
- [39] Heedong Do, Namyoon Lee, and Angel Lozano. “Reconfigurable ULAs for Line-of-Sight MIMO Transmission”. In: *IEEE Transactions on Wireless Communications* 20.5 (2021), pp. 2933–2947. DOI: [10.1109/TWC.2020.3045588](https://doi.org/10.1109/TWC.2020.3045588).
- [40] Kai-Kit Wong et al. “Fluid Antenna Systems”. In: *IEEE Transactions on Wireless Communications* 20.3 (2021), pp. 1950–1962. DOI: [10.1109/TWC.2020.3037595](https://doi.org/10.1109/TWC.2020.3037595).

- [41] Guojie Hu et al. “Secure Wireless Communication via Movable-Antenna Array”. In: *IEEE Signal Processing Letters* 31 (2024), pp. 516–520. DOI: [10.1109/LSP.2024.3359894](https://doi.org/10.1109/LSP.2024.3359894).
- [42] Zhiyong Feng et al. *Movable Antenna Empowered Physical Layer Security Without Eve’s CSI: Joint Optimization of Beamforming and Antenna Positions*. 2024. arXiv: [2405.16062](https://arxiv.org/abs/2405.16062) [cs.IT]. URL: <https://arxiv.org/abs/2405.16062>.
- [43] Zhemin Xu, Sana Sfar, and Rick S. Blum. “On the Importance of Modeling the Mutual Coupling for Antenna Selection for Closely-Spaced Arrays”. In: *2006 40th Annual Conference on Information Sciences and Systems*. 2006, pp. 1351–1355. DOI: [10.1109/CISS.2006.286674](https://doi.org/10.1109/CISS.2006.286674).